กระบวนการเตรียม และสมบัติเชิงกลของโครงสร้างสองชั้นไฮดรอกซีอะพาไทต์/เตตระโกนอลเซอร์โคเนีย

นางสาวลักษณี ภิญโญ

วิทยานิพนธ์นี้เป็นส่วนหนึ่งของการศึกษาตามหลักสูตรปริญญาวิทยาศาสตรมหาบัณฑิต
สาขาวิชาฟิสิกส์ ภาควิชาฟิสิกส์
คณะวิทยาศาสตร์ จุฬาลงกรณ์มหาวิทยาลัย
ปีการศึกษา 2545
ISBN 974-17-1406-8

PROCESSING AND MECHANICAL PROPERTIES OF HYDROXYAPATITE/TETRAGONAL ZIRCONIA BILAYER STRUCTURE

Miss Lugsanee Pinyo

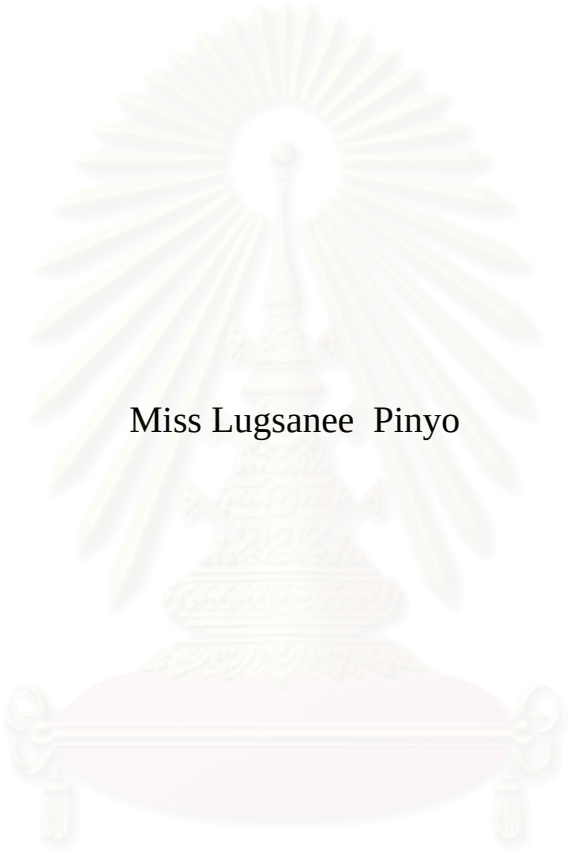

A Thesis Submitted in Partial Fulfillment of the Requirements
for the Degree of Master of Science in Physics
Department of Physics
Faculty of Science
Chulalongkorn University
Academic Year 2002

ISBN 974-17-1406-8

Thesis Title	Processing and Mechanical Properties of Hydroxyapatite/Tetragonal Zirconia Bilayer Structure
By	Miss Lugsanee Pinyo
Field of Study	Physics
Thesis Advisor	Associate Professor Prapaipan Chantikul, Ph.D.
Thesis Co-advisor	Sataporn Wuttiphan, Ph.D.

Accepted by the Faculty of Science, Chulalongkorn University in Partial Fulfillment of the Requirements for the Master's Degree

…… Dean of Faculty of Science
(Associate Professor Wanchai Phothiphichitr, Ph.D.)

THESIS COMMITTEE

…… Chairman
(Assistant Professor Pisistha Ratanavararak, Ph.D.)

…… Thesis Advisor
(Associate Professor Prapaipan Chantikul, Ph.D.)

…… Thesis Co-advisor
(Sataporn Wuttiphan, Ph.D.)

…… Member
(Assistant Professor Kajornyod Yoodee, Ph.D.)

…… Member
(Rattachat Mongkolnavin, Ph.D.)

ลักษณี ภิญโญ : กระบวนการเตรียมและสมบัติเชิงกลของโครงสร้างสองชั้นไฮดรอกซีอะพาไทต์/เตตระโกนอลเซอร์โคเนีย. (PROCESSING AND MECHANICAL PROPERTIES OF HYDROXYAPATITE/TETRAGONAL ZIRCONIA BILAYER STRUCTURE)
อ. ที่ปรึกษา : รศ. ดร. ประไพพรรณ ฉันธิกุล, อ.ที่ปรึกษาร่วม : ดร. สถาพร วุฒิพันธุ์
105 หน้า. ISBN 974-17-1406-8.

งานวิจัยนี้ได้ทำการศึกษากระบวนการเตรียมและสมบัติเชิงกลของโครงสร้างสองชั้นไฮดรอกซีอะพาไทต์/เตตระโกนอลเซอร์โคเนีย การศึกษาแบ่งออกเป็นสองส่วน ในส่วนแรกเราเตรียมชิ้นงานโครงสร้างสองชั้นไฮดรอกซีอะพาไทต์/เตตระโกนอลเซอร์โคเนียโดยกระบวนการขึ้นรูปชิ้นงานด้วยการอัดแบบแกนเดี่ยวแล้วซินเทอริงชิ้นงาน ณ อุณหภูมิที่เหมาะสม ชิ้นงานที่เตรียมได้มีพันธะระหว่างอะตอมตรงรอยต่อระหว่างชั้นได้แข็งแรง อย่างไรก็ตามเราพบว่ามีรอยร้าวอยู่เป็นจำนวนมากในชั้นไฮดรอกซีอะพาไทต์อันมีผลทำให้ชิ้นงานที่เตรียมได้โดยกระบวนการดังกล่าวอยู่ในสภาพที่ไม่เหมาะสมต่อการตรวจสอบกลไกการตอบสนองเชิงกลของชิ้นงาน

ในส่วนที่สองเราดัดแปลงกระบวนการเตรียมโครงสร้างสองชั้นไฮดรอกซีอะพาไทต์/เตตระโกนอลเซอร์โคเนีย โดยเตรียมชิ้นงาน ไฮดรอกซีอะพาไทต์เดี่ยวและชิ้นงานเตตระโกนอลเซอร์โคเนียเดี่ยวแยกกัน จากนั้นนำชิ้นงานทั้งสองติดเข้าด้วยกันโดยชั้นบาง ๆ ของสารยึดติดโพลิเมอร์ ในการใช้เทคนิคอินเดนเทชันร่วมกับเทคนิคบอนด์อินเทอร์เฟสตรวจสอบกลไกการตอบสนองเชิงกล เราพบว่าสมบัติเชิงกลของชั้นไฮดรอกซีอะพาไทต์ของโครงสร้างสองชั้นที่มีชั้นไฮดรอกซีอะพาไทต์บางได้รับอิทธิพลจากชั้นสารยึดติดโพลิเมอร์หรือชั้นวัสดุฐานรองรับเตตระโกนอลเซอร์โคเนีย โดยที่ความต้านทานการยืดยาวออกของรอยร้าวของชั้นไฮดรอกซีอะพาไทต์ของโครงสร้างสองชั้นมีค่าสูงกว่าไฮดรอกซีอะพาไทต์เดี่ยว แต่ความแข็งมีค่าต่ำกว่า อย่างไรก็ตามสมบัติเชิงกลของชั้นไฮดรอกซีอะพาไทต์ของโครงสร้างสองชั้นที่มีชั้นไฮดรอกซีอะพาไทต์หนาไม่แตกต่างจากสมบัติเชิงกลของไฮดรอกซีอะพาไทต์เดี่ยว

ภาควิชา ฟิสิกส์	ลายมือชื่อนิสิต……..
สาขา ฟิสิกส์	ลายมือชื่ออาจารย์ที่ปรึกษา……..
ปีการศึกษา 2545	ลายมือชื่ออาจารย์ที่ปรึกษาร่วม……..

4272380623 : MAJOR PHYSICS
KEY WORD: HYDROXYAPATITE / BILAYER STRUCTURE
LUGSANEE PINYO : PROCESSING AND MECHANICAL PROPERTIES OF HYDROXYAPATITE/TETRAGONAL ZIRCONIA BILAYER STRUCTURE.
THESIS ADVISOR : ASSOC.PROF. PRAPAIPAN CHANTIKUL, Ph.D.,
THESIS CO-ADVISOR : SATAPORN WUTTIPHAN, Ph.D.,
105 pp. ISBN 974-17-1406-8.

An investigation into the processing procedure and mechanical properties of hydroxyapatite/tetragonal zirconia bilayer structure has been carried out. The investigation consists of two parts. In the first part, the green compacts of hydroxyapatite/tetragonal zirconia bilayer structure have been formed by using sigle-end die press. Then they are sintered at a suitable temperature. To form a strong interface between the top and the bottom layer of the obtained bilayer specimens. However, numerous flaws are found in the hydroxyapatite layer. Accordingly, the obtained bilayer structure specimens are not appropriate to be used for an investigation of their mechanical response.

In the second part, an alternative processing procedure is employed. Monolithic hydroxyapatite and tetragonal zirconia specimens are separately prepared and their surfaces are bonded together by a thin adhesive polymer interlayer. By using the indentation technique together with the bonded-interface technique in investigating their mechanical response, it is found that the mechanical properties of the hydroxyapatite layer of the bilayer with thin hydroxyapatite layer are influenced by the presence of the adhesive polymer interlayer or the tetragonal zirconia substrate. Its fracture toughness is higher than that of the monolithic hydroxyapatite whereas its hardness is lower. However, the mechanical properties of the hydroxyapatite layer of the bilayer with thick hydroxyapatite layer are not different from those of the monolithic hydroxyapatite.

Department of Physics
Field of study: Physics
Academic year 2002

Student's signature…….
Advisor's signature…….
Co-advisor's signature.……

ACKNOWLEDGEMENTS

I would like to express my sincere gratitude and deep appreciation to my advisor Assoc. Prof. Prapaipan Chantikul and Dr. Sataporn Wittipan (co-advisor) for valuable guidance and encouragement throughout this thesis. My appreciation goes to Professor Brian R. Lawn, Dr. Supannee Pathumaruk, Dr. Paisan Satsuwan, Assist. Dr. Pisistha Ratanavararak, Assist. Prof. Kajornyod Yoodee and Dr. Rattachat Mongkolnavin, for their valuable suggestions and comment of this thesis.

I would like to acknowledge the Development and Promotion of Science and Technology Talents Project for scholarship. And I also would like to acknowledge the National Metal and Materials Technology Center (MTEC) and Department of Physics, Faculty of Science of Chulalongkorn University for laboratory assistance in this thesis.

Furthermore, I would like to thank the following people: Dr. Panote Thavarungkul for her suggestion; the staffs of workshop of Physics Department for constructing some experimental equipments; my new friends in MTEC for their kindness and help in my experiment; my good friends and others whose names are not mentioned here for their friendship, and help in various ways.

Finally, I would like to express my faithful thanks to my parents and my younger sister for their support, understanding, constant encouragement, without which I would not have completed this thesis.

Contents

Contents(continued)

List of Figures

Page

List of Figures (continued)

Page

List of Figures (continued)

List of Figures (continued)

Page

List of Tables

CHAPTER I

INTRODUCTION

1.1 Biomaterials

There is a necessity for replacing organs which have been lost due to accident or disease. With today medical technology, the lost organs can be replaced by utilizing biomaterials. Biomaterials are defined as any substance, other than a drug, or combination of substances, synthetic or natural in original, which can be used for any period of time, as a whole or as a part of a system which treats, augments, or replaces any tissue, organ or function of the body.

All materials implanted in the body elicit response from living tissue. There are four possible response of living tissue to implants [1]: (1) The surrounding tissue dies when the material is implanted. These toxic materials should not be used as biomaterials. (2) The living tissue is compatible with the implanted material. However, such implanted material is encapsulated by dense fibrous tissue, which prevents distribution of stresses and may cause loosening of the implant. Such material is referred to as nontoxic and biological inactive biomaterials. (3) The living tissue is not only compatible with the implanted material, but it also grows into the implant, thus forming tight natural bonding between the implant and the surrounding tissue. Such materials would be referred to as biocompatible and Surface-Active

Biomaterials. (4) The material, is nontoxic and dissolves with the surrounding tissue. Such materials would be classified as Resorbable Biomaterials.

Varieties of materials have been used as implants. Due to their ability to sustain high stresses, metals are used for heavy load-bearing orthopedic implantation [2]. However, many problems have been encountered when metallic materials are used as implantations, such as wear, corrosion and/or negative tissue reactions [3]. In addition, most of metallic implants are encapsulated by dense fibrous tissue that prevents distribution of stresses and may cause loosening of the implantation [3].

Since bioceramics are compatible with physiological environments [1,2], various ceramics have been medically used for implantations. The compatibility of bioceramics is the result of the fact that they compose of ions usually found in the physiological environment, such as calcium, potassium and sodium or ions showing very limited toxic to body tissue. Thus bioceramics do not cause inflammatory or rejection response by the body. Among them, partially stabilized zirconia and alumina demonstrate high mechanical strength and good biocompatibility. They are widely applied to hip and knee replacements. However, implants made of high strength ceramics, such as zirconia and alumina, are surrounded by a thin fibrous membrane and would cause loosening of the implantation [3].

1.2 Hydroxyapatite as Bioactive Material

In 1971, hydroxyapatite was proposed by Monroe *et al.* for using as hard tissue replacements [4,5]. The major interest of hydroxyapatite [HAp; chemical formula $Ca_{10}(PO_4)_6(OH)_2$], arises from the fact that HAp crystals are the main mineral constituent of vertebrate skeletal systems, comprising 60 to 70 percent of bone and 98

percent of dental enamel. HAp has now been proven to be the most biocompatible, nonbioresorbable and surface active implants [6]. Bone and dental implants made of HAp are naturally bonded tightly to bone or teeth without having to use mechanical interlocking or biological cements. This is because hard tissue formations are observed to occur around HAp implant edges and bridge over the implants, giving an excellent fixation. Due to these advantages of HAp over other biomaterails, it is a challengeable material to be developed for using in orthopedic and dental surgeries, such as hip joints, middle ear reconstruction, jaw augmentation and tooth root replacement.

Unfortunately, brittleness is an overriding factor which limits the ultimate usefulness of HAp. The fracture toughness* (K_c) of HAp does not exceed the value of about 1.0 MPa $m^{1/2}$ [7,8] whereas K_c of human bone have the value of 2-12 MPa $m^{1/2}$. Due to its low fracture toughness, HAp ceramics cannot be used as heavy-loaded implants, such as artificial bones or teeth. Their medical applications at present are limited to non-stressed region of skeleton or to the region where compression is the main mechanical load [1].

Various attempts have been made to improve the fracture toughness of HAp. Among them, the HAp-based ceramic composites are attractive. Various reinforcements, including whiskers [9,10], fibers [11], particles, [12,13] have been dispersed into the HAp matrix. The fracture toughness K_c of HAp-based composites is in the range of 1.4-3.9 MPa $m^{1/2}$, depending upon the used reinforcements [6]. However, the addition of foreign materials into the HAp matrix may lead to the decrease of its biocompatibility and may promote decomposition of HAp into

* Fracture toughness, K_c, is a mechanical parameter, which indicates the resistance of material to crack initiation and propagation under tensile stresses.

tricalcium phosphate (TCP)[11,12]. The presence of TCP in HAp material increases its biodegradability and slow crack growth susceptibility.

Layered structures, in which layers of different composition and/or microstructure are combined to meet specific requirements, are another means to provide a new dimension for material developments. Many ceramic layered composites with alternating microstructures are developed to be used for many structural and biomedical applications [14,15]. Such ceramic layered composites enhance mechanical properties such as strength, toughness, contact damage, machinability, and resistance of wear/erosion. For example, a hard coating can protect a softer and tougher substrate from wear while the substrate provides fracture resistance. Thus ceramic layered composites are another possible and intriguing dimension for achieving the required toughness and strength improvement of hydroxyapatite. The development of a bilayer structure, which consists of HAp as top layer and tough bioceramics as substrate can be envisaged as an attractive means to provide an artificial substitution for an implant to be used in orthopedic and dental surgeries. The hydroxyapatite top layer can stimulate hard tissue growth which bridge the bilayer implant to bone while the tougher substrate provides fracture resistance. Plasma spraying technique has been used to prepare HAp layer on titanium substrate [15,16]. However, HAp powders need to be heated up to high temperatures (>> 1200^{O}C). Therefore the control of the composition and structure of the HAp layer is not easy. Moreover, its adhesion to the substrate is not strong and stable for a long period. Many other methods such as sol-gel [17,18] and hydrothermal method [19] are also employed to fabricate HAp on tough substrate. However, the obtained HAp layer is normally of the order of a few microns. Therefore it is not thickness enough to resist resorbability of HAp which can be as much as 15-30 μm per year [20].

1.3 Objectives and Scope of This Work

In this work, we aim to fabricate a bilayer consisting of hydroxyapatite as the top layer and high fracture toughness ceramics, such as alumina or partially stabilized zirconia, as the substrate. The mechanical response together with mechanical characteristics of the obtained bilayer specimens will be examined. The motivation comes from the need to develop an effective fabrication means to improve the poor behavior of the hydroxyapatite monolith under tensile stresses. Such a bilayer will combine the excellent bioactivity of hydroxyapatite to the high fracture toughness of the substrate. We will fabricate bilayer specimens so that the thickness of the substrate is fixed whereas the thicknesses of the hydroxyapatite top layer are varied. The obtained mechanical behavior data of such specimens will give an indication of the optimum thickness of the hydroxyapatite top layer of the bilayer.

A cosintering procedure of the top layer and the substrate will be employed to prepare bilayer specimens. Such processing procedure is simple and allows for a wide range of top layer thickness adjustment. The green compact of the bilayer is first formed by single-end die pressed and followed by normal sintering. Spherical indentation technique together with bonded-interface technique will be used as a means to investigate the mechanical response of the bilayer specimens to stresses. The mechanical characteristics of the bilayer specimens will be evaluated from the indentation damage patterns generated by Vickers indentation. In addition the mechanical response and characteristics of the hydroxyapatite monolith will be examined and be used as control.

CHAPTER II

BACKGROUND

2.1 Review of Laminate Research

In the past decade, various laminated ceramic composites have been developed and studied [21,22,23,24,25]. The specific application for the composite will determine the optimum composition, microstructure and layer geometry. They are particularly attractive and have provided a new and intriguing dimension to the area of structural ceramics. Their properties, such as strength, toughness and hardness, can be tailored to meet specific requirements that the constituent layer materials cannot. There are different philosophies for achieving the required property improvements. One of the methods is the development of surface compressive residual stress in outer layers. This approach results in an increase in the strength and the "apparent" fracture toughness [26,27]. Wang and Hu [28] observed that the Hertzian contact fatigue damage resistance was markedly improved relative to monolithic ceramics when they generated residual stress in the outer layer. The other approach is to deliberately introduce weak interfaces in order to promote crack deflection for toughening. Clegg *et al.* [29] employs this approach in the laminated composites of silicon carbide and graphite, in which silicon carbide sheets are separated by thin layers of graphite. The observation that cracks in the lower SiC layers initiate at points well away from the tip of the original delamination crack led Clegg and Seddon to suggest that the second crack grows from an existing defect within the SiC lamina [30]. This implies that the

strength of the laminate is determined by the strength of the individual SiC layers and that a potential strategy for improving the mechanical behavior could be to increase the strength of the layers. This idea was subsequently confirmed by Clegg [31]. By the introduction of artificial flaws of different size into the SiC layers, it was found that the apparent fracture toughness varied linearly with the strength of the unnotched bar. Recently, Mawdsley *et al.* [32] propose the multilayer laminates consisting of monazite as the interphase to promote debounding between the reinforcement and the matrix during the fracture of oxide-based composites. The study of fracture behavior and micromechanical properties of alumina/monazite depicts that the achievement of crack deflection may be possible using monazite as interphase in oxide composites.

The more recent method is the development of a composite with strong interfaces in order to avoid crack deflection along the interface. Russo *et al.* [33,34] propose a tri-layer composite design in which the inner layer consists of a material with a strong R-curve (a material which fracture toughness increases as a function of crack length), sandwiched by the outer layers of a high strength, non R-curve material. These systems exhibit high strengths over a wide range of starting flaw sizes. The mechanical properties of laminates are widely analyzed, including the use of Hertzian indentation technique via the bonded-interface technique to determine damage patterns by Lawn and co-workers [35,36,37]. For example, An *et al.* [38] evaluated the Hertzian indentation of tri-layers of fine-grained (d ~ 2.5μm) alumina (A) and a mixture of alumina and 30 vol% calcium hexaluminate ($CaAl_{12}O_{19}$) (C) with either alumina as the outer surface layer (ACA composite), or the calcium hexaluminate as outer layers (CAC composite). They found that the depth of cone cracks in an outer A layer or diffuse microcracked zones in an outer C layer was

restricted to the thickness of the outer layer. This constraint enhanced the contact damage resistance of tri-layer material.

2.2 Contact Damage in Monolithic Solids

A strength theory in terms of formal indentation mechanics was first proposed by Evans [39], at a time when empirical evidence for the highly deleterious effect of localized contact on specimen integrity was beginning to mount [40,41]. However, Evans work was concerned with only one specific situation of impact loading, namely with a hard spherical indenter: the role of many indentation variables necessary in characterizing the damage due to real irregular particles was not determined. The variability in indentation geometry gives rise to a wide diversity of fracture patterns. This diversity appears at first sight to cause complexity in the development of a suitable basis for a theory of indentation fracture. Lawn *et al.* [42] pointed out that real contact situations involving irregular particles can be bracketed into two basic indentation configurations, “blunt” or “sharp”: real particles tend to be blunt if well worn, or sharp if freshly crushed. The distinction between “blunt” and “sharp” indenters, which provides a means for classifying and analyzing indentation fracture patterns, overcomes this difficulty. Blunt indenters are characterized by elastic contact whereas sharp indenters are characterized by elastic/plastic contact. The analysis of contact damage in monolithic solids has received the earliest attention and now well understood. Experimentally, spherical indenter is used to simulate contact damage due

to blunt indenter whereas Vickers[†] or Knoop[‡] indenter, used in hardness testing, are used to simulate contact damage due to sharp indenter.

2.2.1 Contact Damage due to Vickers Indentation

In brittle solids, Vickers indentation produces two basic types of crack patterns: median/radial cracks [43,44] and lateral cracks [45]. A schematic of the geometrical parameters of radial system is illustrated in Fig. 2.1. In the fracture mechanics, these cracks occur when the stress-intensity factor exceeds the intrinsic fracture toughness of the material [46]. Fig 2.2 depicts the basic sequence of crack propagation events [46]: (i) the sharp point induces inelastic, irreversible deformation; (ii) at a critical load one or more nascent flaws within the deformation zone become unstable, and pop-in to form subsurface radial cracks on tensile median planes; (iii) on increased loading, the crack propagates incrementally downward; (iv) on unloading, the median cracks close up below the surface but simultaneously open up in the residual tensile field at the surface as the contact recovers its elastic component; (v) just prior to removal of the indenter the residual field becomes dominant, further expanding the surface radials and initiating a second system of sideways spreading, saucer-like lateral cracks near the base of the deformation zone; (vi) the expansion continues until the indenter removal is complete, both crack systems ultimately tending to half-pennies centered about the load point. The lateral crack system forms a saucer-like fracture approximately parallel to the surface. The median crack grows straight down

---

[†] A Vickers indenter is a squred-base diamaond pyramid with an angle of 130^{O} between opposite faces of the pyramid and 148^{O} between the pyramid edges.

[‡] A Knoop indenter is a rhombic-base diamond pyramid with a ratio between long and short diagonal of about 7 to 1. The pyramid shape used has an included logitudinal angle of $172^{O}30'$ and included transverse angle of $130^{O}0'$.

along the axial σ_3 stress trajectory (Fig. 2.3), orthogonally to the tensile stress $\sigma_1 = \sigma_2 = \sigma_\theta$ at $\phi = 0$ (Fig. 2.4); at the same time, the crack also grows sideways in a plane $\theta =$ const. Along the σ_1 trajectories, orthogonally everywhere to the hoop stress σ_2 (Fig. 2.5), but is restricted in the sideways expansion by the compressive lobes in the σ_2 field close to the surface [43].

In this case, the hardness, *H,* can be evaluated by the mean contact pressure, between the indentation and surface specimen [46]:

$$p_o = P/\alpha_o a^2 = H \qquad (2.1)$$

where P is the indentation load and α_o is to be regarded as numerical constants: for Vickers indenters $\alpha_o = 2$ if a is taken as the impression half diagonal and if H is identified with the mean contact (invariant) pressure.

In addition, toughness K_c can be evaluated from indentation load and dimension of penny-like radial/median crack [47]:

$$K_c = \xi_V^R (E/H)^{1/2}(P/c^{3/2}) \qquad (2.2)$$

where P is the indentation load, c is characteristic dimension of the radial/median crack and ξ_V^R is a material-independent constant for Vickers-induced radial cracks. E and H are the Young's modulus and hardness of specimen, respectively.

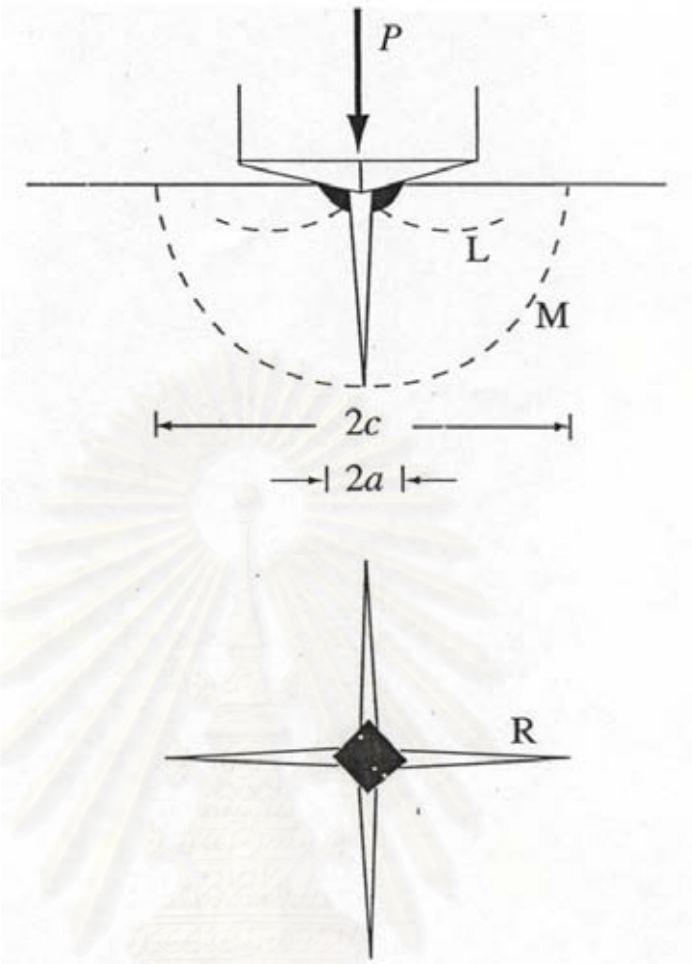

Fig. 2.1 Schematic of radial(R)-median(M) and lateral(L) crack systems including geometrical parameters of radial system. Dark region denoted irreversible deformation zone. Courtesy of Lawn *et al.* [46].

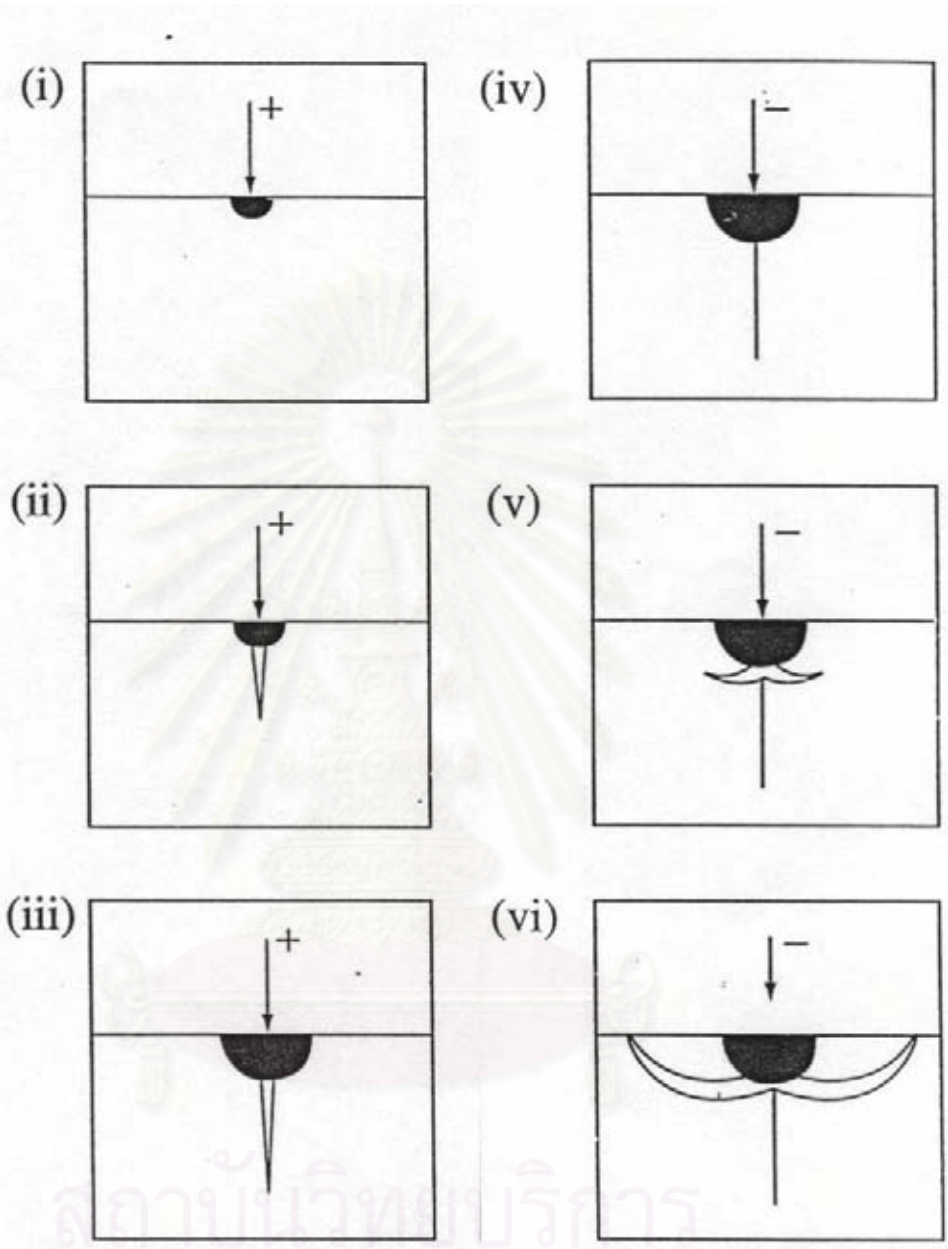

Fig. 2.2 Schematic of vent crack formation under point indentation. Median vent forms during loading (+) half-cycle, lateral vents during unloading (-) half cycle. Fracture initiates from inelastic deformation zone (dark region). Courtesy of Lawn *et al.* [43].

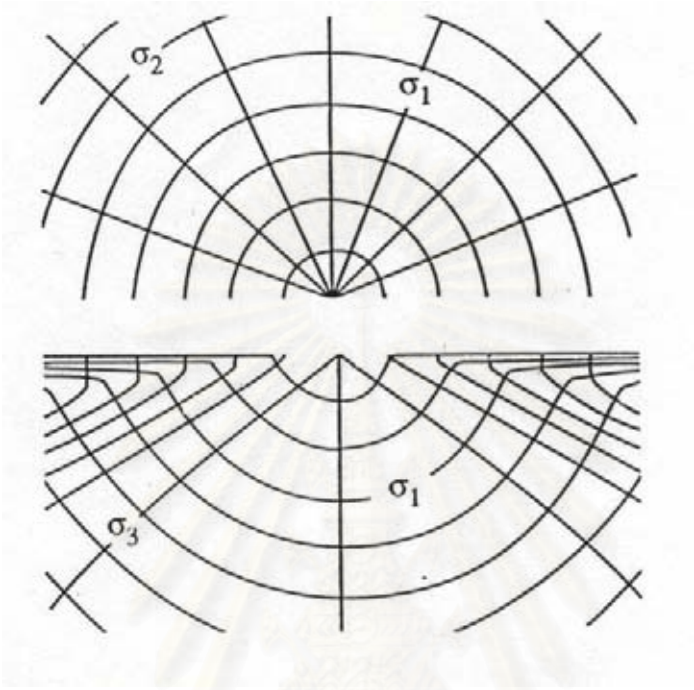

Fig. 2.3 Boussinesq field, for principal normal stress σ_1, σ_2, and σ_3. Stress trajectories, half-surface view (top) and side view (bottom). Courtesy of Lawn *et al.*[43].

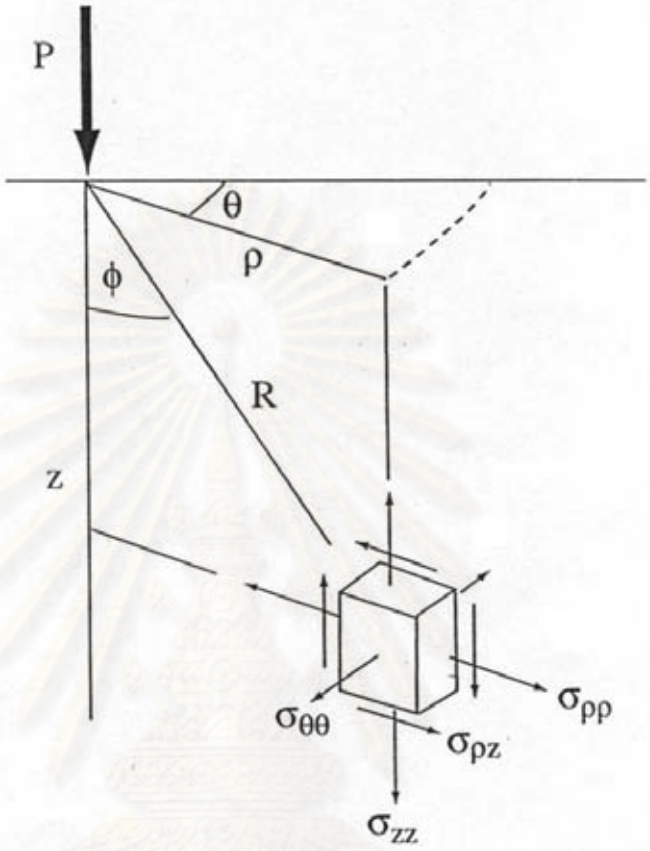

Fig. 2.4 Co-ordinate system for indention stress field. Courtesy of Lawn *et al.* [43]

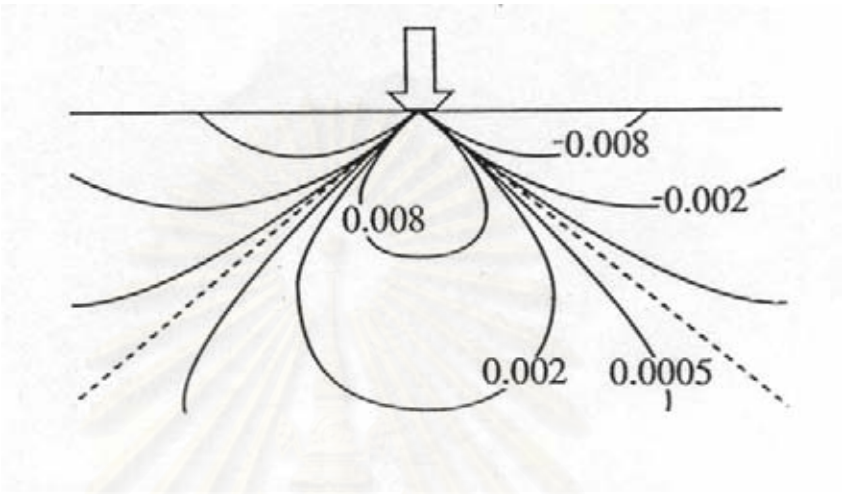

Fig. 2.5 Contour of principal normal stress, σ_2 in Boussinesq field, shown in plane containing contact axis. Plotted of $\nu = 0.25$. Unit of stress is p_0, contact "diameter" (arrowed) is 2a. Courtesy of Lawn *et al.* [43].

2.2.2 Contact Damage due to Hertzian Indentation

Before mentioning in the spherical indentation fracture for layered structure, we will focus our attention briefly on the cone crack fracture produced by Hertzian indenter on the brittle ceramics. Therefore it is a fundamental knowledge.

Consider the frictionless contact of a sphere on a flat surface. The contact pressure increases monotonically with load form zero at first contact. As the load increases, the contact point expands into cycle. The stress field is initially elastic, as the classical Hertzian stress field [48,49]. Beyond a critical load the material undergoes irreversible deformation and/or fracture (Fig 2.6). In brittle ceramics, the sequence of events for one complete indentation is depicted in Fig 2.7[46] : (i) pre-present surface flaws are subjected to tensile stresses outside the contact zone; (ii) at some point in the loading a favorably located flaw runs around the contact circle to form a surface “ring” crack; (iii) on further loading the embryonic ring crack grows incrementally downward in the rapidly weakening tensile field; (iv) at critical load the ring becomes unstable and propagates downward into the full frustum of the Hertzian cone (pop-in); (v) at still further loading the cone continues in stable growth (unless the contact circle expands beyond the ring crack, in which case the cone is engulfed in the compressive contact zone); (vi) on loading, the cone crack closes. An example of Hertzian cone fracture is shown in Fig 2.8.

For the elastic field, Hertz was the first to investigate the contact problem of frictionless elastic bodies under normal sliding [50]. The configuration of the Hertzian test is a linear elastic half-space (specimen) subjected to normal loading by a hard spherical indenter of radius r, as shown in Fig 2.9. Hertz [50] calculated the radius, a, the circular elastic contact as the function of the applied force, P by

$$a^3 = (4/3)\,(kPr/E)$$

where E and E' is the Young's modulus of specimen and indenter respectively, and likewise ν and ν' the Poisson's ratio. k is an elastic mismatch factor,

$$k = (9/16)\,[(1-\nu^2)+ (1-\nu'^2)\,(E/E')] \qquad (2.4)$$

The distance of mutual approach of the contacting bodies is given by

$$Z = (4k/3E)^{2/3}(P^2/r)^{1/3} \qquad (2.5)$$

These three equations are sufficient to specify the loading characteristics for any commonly used spherical indenter loading mode [51].

The stress-strain response at low stresses according to the classical linear Hertzian relation [50] is:

$$p_0 = (3E/4\pi k)\,a/r \qquad (2.6)$$

where we define p_0 is the "indentation stress", and a/r is "the indentation strain". Because the elastic constants are specifiable a priori a given indenter/specimen material system, the uniaxial stress-strain relation is predetermined. The value of k is dependent on the indenter material.

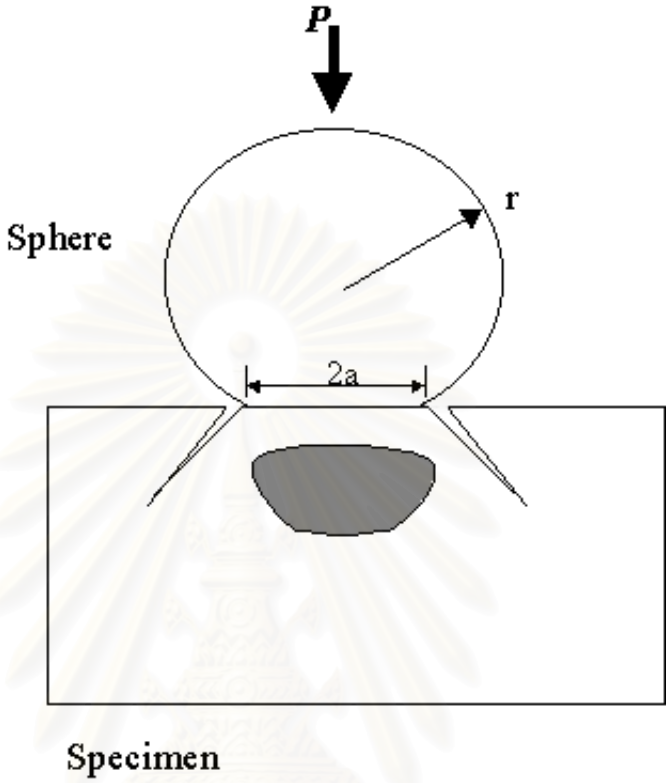

Fig. 2.6 Hertzian contact of sphere on flat ceramic specimen. Beyond elastic limit, contact initiates cone crack fracture ("brittle mode"). Or subsurface deformation zone ("quasi-plastic mode"). Courtesy of Lawn [49].

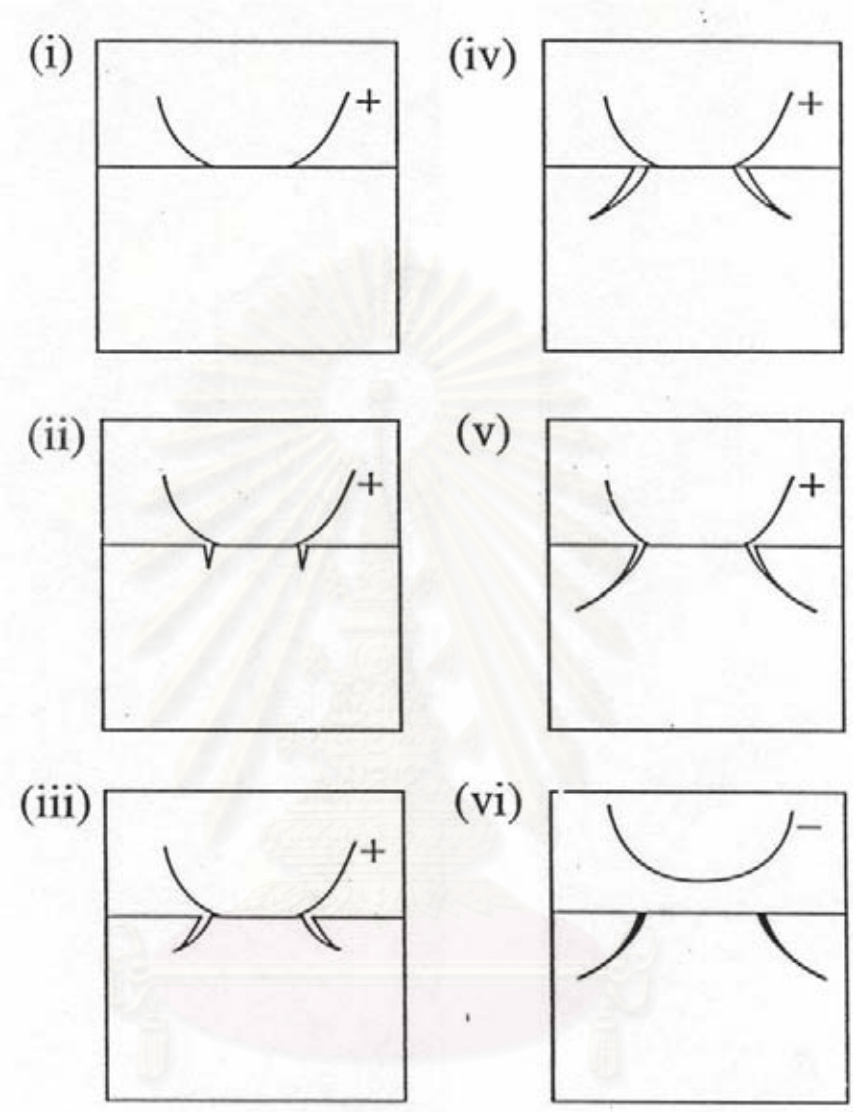

Fig. 2.7 Hertzian cone crack system. Evolution of cone during complete loading(+) and unloading(-) cycle. Courtesy of Lawn [46].

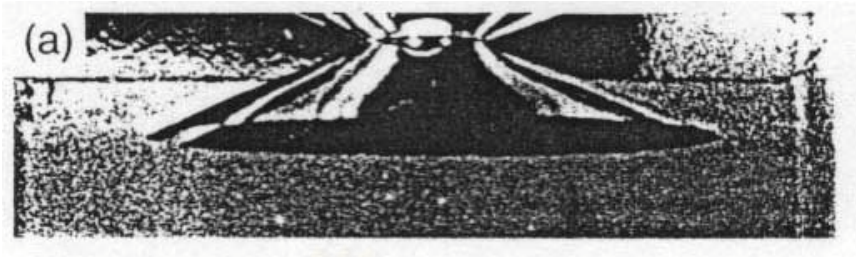

Fig. 2.8 Photograph of crack in soda-lime glass, produced by indentation with cylindrical punch at P = 40 kN (block edge 50 mm) Courtesy of Roesler [52].

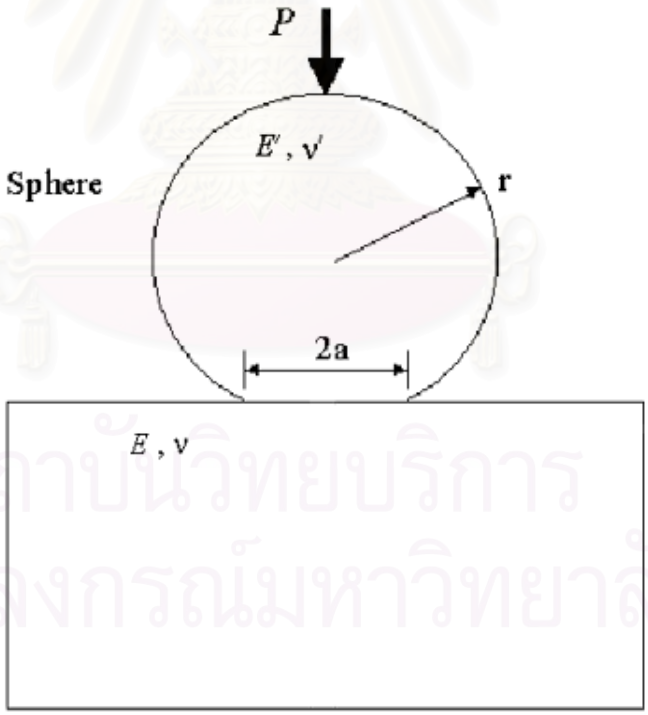

Fig. 2.9 Parameters of Hertzian cone crack configuration.

2.3 Contact Damage in Layered Structure: Hertzian Indentation

In this thesis, Hertzian indentations are applied to initiate the fracture deformation on the surface. The effect of contact on bilayer structure with dependence on thickness of top layer will be observed. In this section we will focus our attention briefly on the contact damage produced by Hertzian indenter on the layered structures.

Recently, the design of ceramic-based layered structures has focused on strong interlayer interfaces. There are several techniques being used to evaluate mechanical properties and contact damage, including indentation techniques. Hertzian indentation is well known technique to be used to introduce contact damage. It gives amount of information on both elastic and plastic responses and the technique is simple. This concept of strongly bonded homogenous/heterogeneous interlayers has been proposed by Wuttiphan *et al*. [36] and Lee *et al.* [53,54]. Those authors used thin brittle coatings on soft substrates, with different elastic-plastic mismatch. They observed transverse cracks that were induced in brittle coatings (on soft substrates) by spherical indenters. The transverse cracks, including some new modes did not observed in monolithic materials. Therefore Lawn and co-workers [55,56,57] are interested to systematically study these cracks. Chai *et al.* investigate the effect of adhesive interlayer in determining the critical condition for fracture in brittle layer structures from Hertzian indentation using a model of transparent trilayer system consisting of the a glass plate coating jointed to a glass plate substrate by epoxy adhesive. They reported that the radial cracks at the glass/ adhesive interface generated most easily in systems with large adhesive thickness (and smaller overlayer thicknesses).

The transverse cracks occur from sphere indenter, of radius r at load P on coating of thickness d (on the layered structure) as shown in Fig.2.10 . The coating is considered to be thin enough that it is flexible under the applied contact. These cracks are separated to two main fracture modes [58]:

Cone cracks: the crack first develops from the top surface outside the contact circle, where the tensile stress is maximum, as a shallow, stable surface ring within a rapidly diminishing subsurface tensile field; it then pops into its ultimate (truncated) cone-like geometry at the critical load.

Inner cracks: this crack is a relatively new fracture mode, unique to layered structures in concentrated loads. The cracks generate at the coating/substrate interface immediately below the contact, and extend radially over large lateral distances as the load is increased beyond the critical load. They remain beneath surface during this lateral extension and so are not easily detected in opaque coatings.

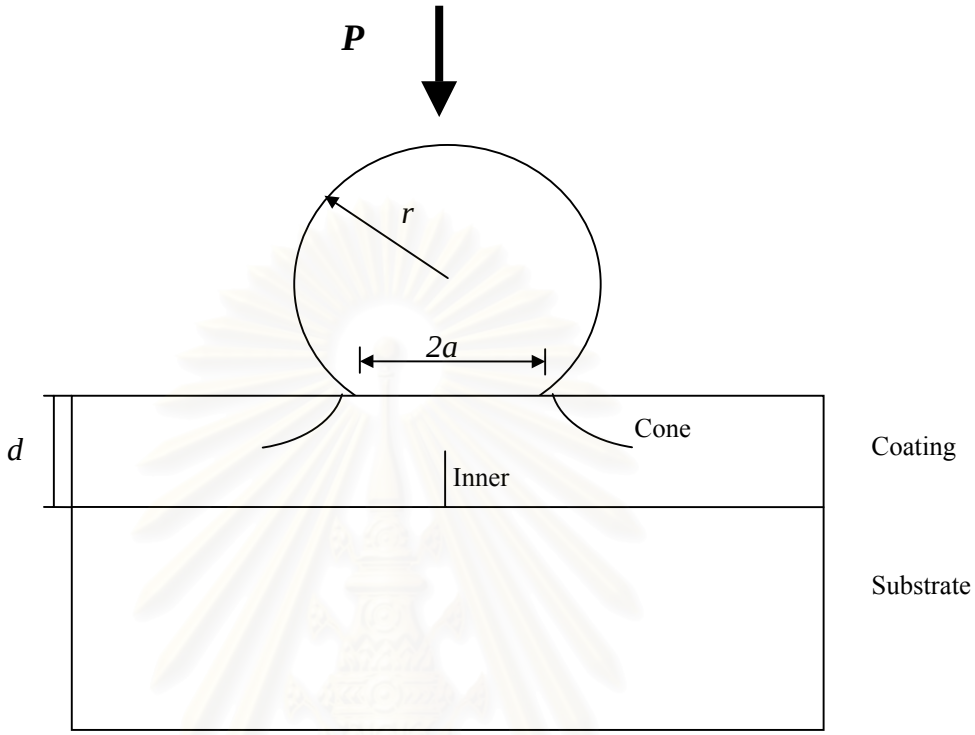

Fig. 2.10 Schematic of transverse cracks in brittle coating on a compliant substrate, showing indenter of radius *r* at load *P* on coating of thickness *d*. Surface circumferential cone crack around contact circle, radius *a*. Subsurface inner crack at coating/substrate interface. Courtesy of Lawn [58].

2.4 Observation of Damage: The Bonded- Interface Technique

In the study of the strength and lifetime properties of the material, the nature of damage deformation that occurs from contact bearing or spurious impacts with foreign bodies is important to determine. In the transparent ceramic, such as glass, all damage deformation can directly be observed. On the contrast, the subsurface contact damage cannot directly be observed in the opaque ceramic. One of the most powerful techniques for revealing such damage is the "bonded-interface" technique. This technique is familiar to researchers that study in either monolith [59,60,61] or laminate structure [62,63]. Other techniques that can be used to investigate subsurface deformation and fracture are thermal wave [64] or cross-section polishing [59], but these techniques either do not reveal the damage so clearly (sectioning), or are labor-intensive (thermal wave). Therefore, we will use the bonded-interface technique in this work.

The bonded interface technique is illustrated in Fig.2.11. Two half-specimens with polished surface are bonded face-to-face under clamping pressure with a thin layer of adhesive. Indentation test surface with grounded and polished is perpendicular to the bonded interface. Indentations are made across the interface trace at the test surface. After indentation, the specimen halves are separated. Then, the reflection optical microscopy using Nomarski interface contrast is used to examine the subsurface deformation and fracture pattern in section view. Careful experimentation has been made to assure that the damage observed is indeed a true representation of the real damage geometry, by comparing bonded-interface observation with dark-field observations in translucent course grain aluminas [59]. It

has also been illustrated that the bonded-interface technique does not qualitatively affect the concentration of damage or the shear stresses at which it occurs [59, 39].

As indicated above, the bonded-interface technique is the most powerful method obtainable to investigate contact damage patterns. The dark-field illumination cannot be revealed the damage pattern beneath surface of opaque, most of ceramics. Thermal wave techniques are revealing, especially when microcracking is present, but are labor- and instrument-intensive. Consequently, the boned-interface is the method to apply in this thesis.

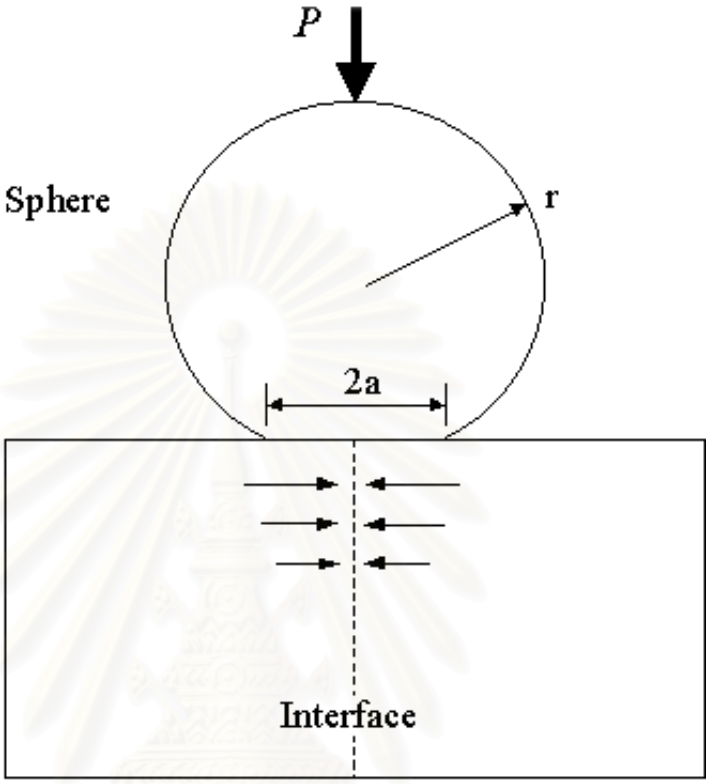

Fig. 2.11 Schematic Hertzian indentation test for bonded interface specimen. Sphere, radius *r*, delivers load *P* over contact radius *a*. Specimen consists of two polished halves bonded across the interface. Compressive stress beneath contact between specimen halves during indentation.

CHAPTER III

EXPERIMENTAL PROCEDURE

3.1 Synthesis of Hydroxyapatite Powder.

In this work, we attempt to synthesize powder to be used as raw material for bilayer structure preparation. These bilayer structures consist of HAp as the top layer and zirconia as the substrate.

3.1.1 Introduction

The HAp powders can be synthesized by means of various techniques, either dry or wet method. The wet chemical syntheses, which utilize either the precipitation from mixed aqueous solution or the hydrolysis of calcium phosphates, prevail in practical use. In the precipitation reaction, solution of $Ca(NO_3).4H_2O$ and $NH_4H_2PO_4$ are brought to pH 11-12 with concentrated NH_4OH. The phosphate solution is dropwise added to the stirred calcium solution [65].

Another method is the addition of H_3PO_4 to $Ca(OH)_2$; the pH changes from 12.4 to 8.7 as the precipitation reaction proceeds [66]. In hydrolysis, $CaHPO_4$ is carried out in a NaOH solution of low concentration for several hours at 25^{o}C to 100^{o}C or for 20 h in boiling distilled water [67]. The followings are important

parameters in the various compositions and structures of HAp obtained from these production ways:

1. The flow rate for the reagents, which controls the crystal size of apatites.
2. The pH value at which the precipitation is carried out.
3. The presence of impurities which can easily be incorporated in the structures.

The solid-state reactions between calcium and phosphorus compounds at high temperature (> 900^{o}C) is one of the methods, which apatites are prepared by the dry chemical method [68].

The crystal structure of HAp was previously reported to belong to the space group $P6_3/m$ in the hexagonal system [69], but is now known that HAp tends to occur in a close-similar pseudohexagonal monoclinic form [70]. At high temperatures, the HAp structure may be modified depending upon its stoichiometry[§], the temperature, the atmosphere, and the synthesis conditions. Most HAp synthesized from the dry-chemically synthesized HAp methods, such as by the solid state reaction, have the advantage of providing stoichiometric HAp powders. On the contrast, most wet-chemically synthesized HAp powders are nonstoichiometric[**] because of the presence of HPO_4 and/or H_2O during the synthesis. The results after the thermal treatment are stoichiometric HAp and tricalcium phosphate (TCP)[71].

At the temperatures higher than 900^{o}C, the HAp can be partially dehydrated, as follows:

$$Ca_{10}(PO_4)_6(OH)_2 \leftrightarrow Ca_{10}(PO_4)_6(OH)_{2-2x}O_x\square_x + xH_2O$$

where $\square$ denotes vacancies at lattice sites of OH.

[§] HAp ($Ca_{10}(PO_4)_6(OH)_2$) is stoichionmetric if the Ca/P molar ratio is accurately 1.67 and H_2O content 1.79wt%[9].
[**] The nonstoichionmetry of HAp is presented by $Ca_{10-x}(HPO_4)_x(PO_4)_{6-x}(OH)_{2-x}nH_2O$; o<x<1, n = 0-2.5

The reaction is an equilibrium reaction and the reaction product may depend on the H_2O vapor pressure. If H_2O is added, the reaction shifts to the left, so stabilizing the HAp. The structure of the HAp is then preserved up to 1100°C. Pyrolysis (decomposition as a result of heat) in vacuum or in water-free gasses shifts the reaction to the right and an oxyhydroxyapatite is formed, $Ca_{10}(PO_4)_6(OH)_{2-2x}O_x\square_{..x}$ [72].

In the limit, when x = 1, oxyapatite, $Ca_{10}(PO_4)_6O$, is formed [70]. The oxyapatite exists only under a secondary vacuum of 10^{-4}-10^{-6} torr in sufficiently water-free atmosphere and stable between 800°C and 1050°C. Beneath 800°C under the same vacuum, it has been shown that the oxyapatite rehydrates to an oxyhydroxyapatite during cooling, depending on the cooling conditions. This is stable in the atmospheric moisture at room temperatures [70].

From 1050°C, the hydroxyapatite may be decomposed, as the follows,

$$Ca_{10}(PO_4)_6(OH)_2 \longrightarrow 2\beta Ca_3(PO_4)_2 + Ca_4P_2O_9 + H_2O;$$

At the temperature higher than 1350°C, $\beta Ca_3(PO_4)_2$ transforms to $\alpha Ca_3(PO_4)_2$ [73]. The α phase, a polymorphic form of β, is the high-temperature phase which is maintained upon cooling.

3.1.2 Synthesizing Procedure of Hydroxyapatite Powder

The precipitation reaction method is used as a means to synthesize HAp powders. Fig. 3.1 is the flow chart summarizing the synthesizing procedure employed in this work.

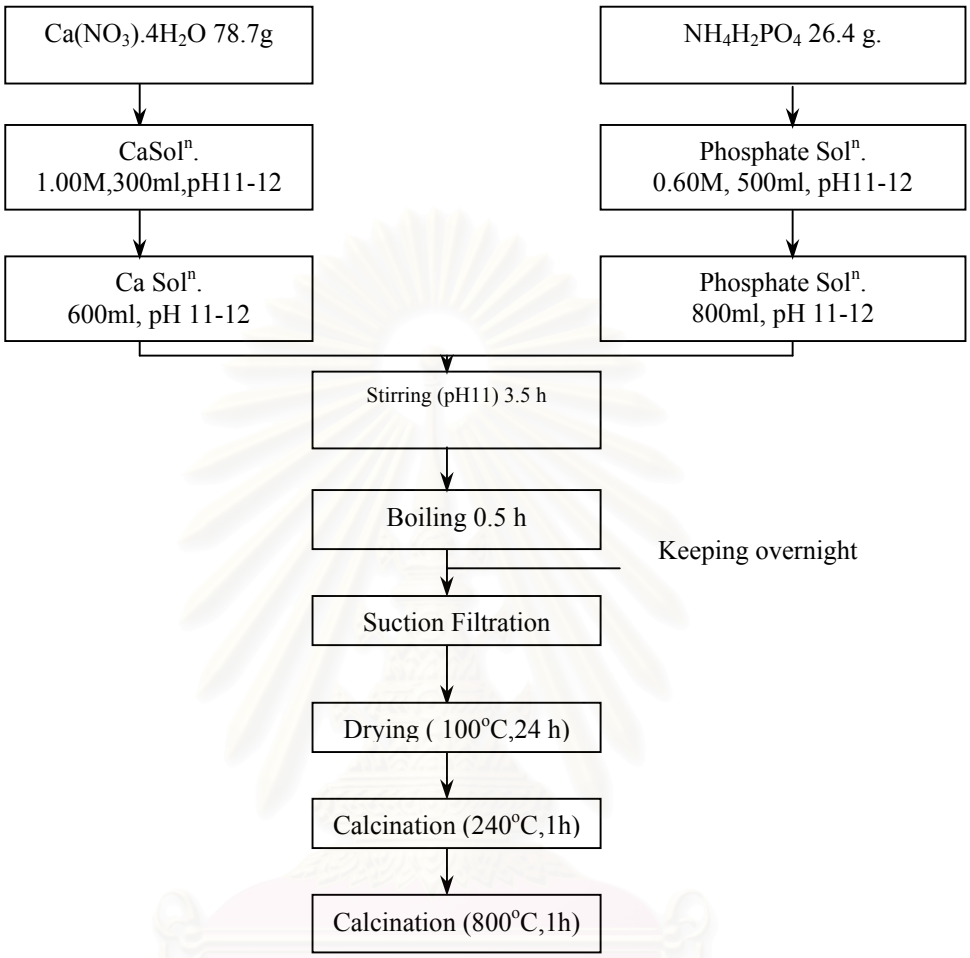

Fig. 3.1 Flow chart for the synthesizing procedure employed in this work.

Seventy-eight and seven-tenth grams (0.33 mol) of $Ca(NO_3)_2.4H_2O$ was dissolved in 300 ml of de-ionized water in 2,000 ml flask. The solution was adjusted to pH 11 to 12 by the addition of amonium hydroxide and then diluted to 600 ml. Calcium solution, vigorously stirred for 3.5 h, was dropped slowly into a solution of 26.4 g (0.2 mol) of diamonium hydrogen phosphate in 500 ml de-ionized water which similarly had been brought to pH 11 to 12 with amonium hydroxide and thereafter diluted to 800 ml. The reaction mixture, which was milky, was under the pH control (pH 11 to 12) and in the room temperature (25^oC) during synthesizing process. The reaction mixture was boiled for half an hour and left overnight at room temperature to allow the precipitate to settle in the supernatant solution. The supernatant solution was separated from the precipitate by pouring and by using the suction filter, with the application of a weak vacuum.

The filtered cake was washed with 100 ml of hot water, dried for 20 h at 100^oC, then broken down by grinding in a mortar. The powder was calcined within an hour at 240^oC to remove the ammoniumnitrate (NH_4OH) and was thereafter heated for 3 h at 800^oC by a rate of 300^oC/h, whereas cooling was performed as the furnace cooled down. The calcination process promoted powder crystallinity. Grinding again broke down the powders if the powder agglomerated.

3.1.3 Characterization

The phase composition of calcined powder was determined by powder X-ray diffractometery (XRD) (model JDX 3530; JEOL, Tokyo, Japan), using $CuK_{\alpha 1,2}$ radiation at 30 mA and 30kV with scanning from $2\theta = 0^o$ to 90^o in step of 0.04^o. Each step counted for 0.05s. The obtained X-ray diffraction pattern (Fig.3.2) illustrated that

the maximum diffraction line was at $2\theta = 31.8^{o}$. Fig. 3.2 showed the comparison of XRD pattern of the obtained powders with the reference HAp. It can be seen that both patterns are closely corelated, thus confirming that the obtained powders are monophase HAp.

3.2 Commercial Partially Stabilized Zirconia Containing 3 mol% Yttria Powders

In this thesis, we attempt to improve the toughness and strength of HAp by laminated composite method. Therefore a suitable choice of the material to be used as the substrate is important to the fabrication of the bilayer structure. The biocompatibility and high fracture toughness are the most important requirements for the candidate substrate. Partially-stabilized zirconia and alumina are well-known as bionert materials having high mechanical toughness. However, the candidate substrate should have the thermal expansion coefficient and sintering temperature closed to HAp for the achievement of the successful fabrication of bilayer. Table 3.1 shows the comparison of the thermal expansion and sintering tempurature of partially-stabilized zirconia, alumina and HAp. It can be seen that these parameters of partially-stabilized zirconia are closer to HAp than those of alumina. Therefore, partially-stabilized zirconia is chosen as the substrate of the bilayer which will be fabricated in this work [74,75,76].

The martensitic transformation of tetragonal to monoclinic phase occuring in zirconia was first reported in a paper entitled " Ceramic steel?" by Garvie *et al.* [77].

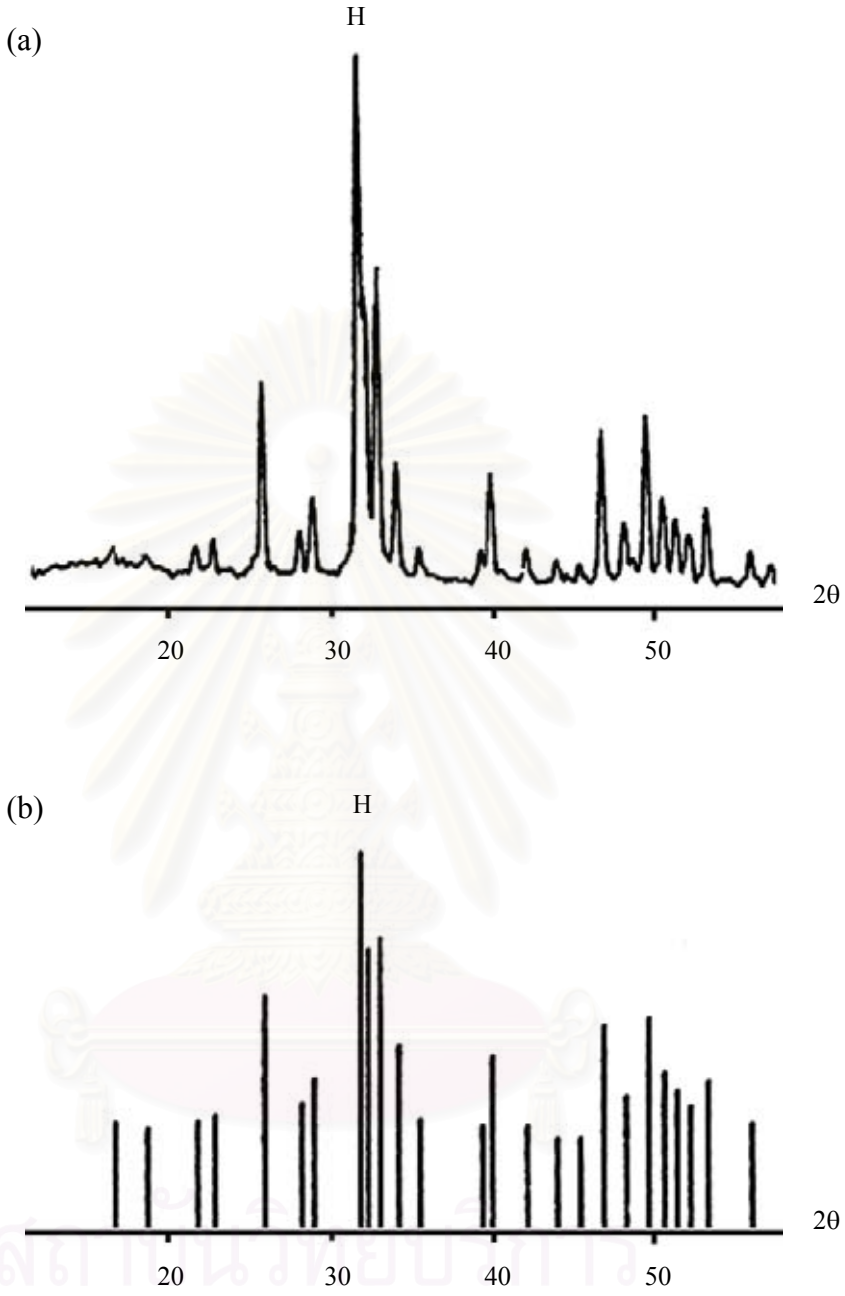

Fig. 3.2 XRD pattern of as-calcined HAp at 800^{O}C showing in comparison with reference HAp: (a) synthesized HAp; (b) reference HAp.

Table 3.1 Physical Properties of HAp, ZrO_2 and Al_2O_3 [74-76].

Property		Hydroxyapatite	Zirconia	Alumina
Density	g/cm^3	3.07	5.5-6.1	3.97
Melting Point	^OC	1650	2700	2051
Sintering Temperature	^OC	1200	1400	1700
Thermal Expansion	K^{-1}	10-13.7 $x10^{-6}$	11 $x10^{-6}$	6-9 $x10^{-6}$
Poisson's ratio		0.26	0.3	0.23
3-PT Bend Strength	MPa	84-113	600-1200	300-600
Hardness	GPa	10-12	12-14	14-20
Young's Modulus	GPa	65-100	210	380
Fracture Toughness	$MPam^{1/2}$	0.6-1.5	10	4-6

This phase transformation can be induced not only under the change of temperatures but also under the influence of any applied stress at/or near room temperature.

The tetragonal to monoclinic phase ($t \rightarrow m$) transformation in pure ZrO_2 was reported to begin at ~950^{O}C and then nearly complete at 750^{O}C on cooling. In contrast, the reversible phase transformation was reported to commence at ~ 1000^{O}C and then nearly complete at 1180^{O}C on heating [78][††]. Therefore pure zirconia, only very small particles can be retained at room temperature in the tetragonal structure. The addition of a stabilizing compound such as magnesia (MgO), calcia (CaO), yttria (Y_2O_3) or ceria (CeO_2) in zirconia, was found to retain the tetragonal phase from spontaneous transformation on cooling. Zirconia-based systems are usually classified in three groups [79]: (1) tetragonal zirconia polycrystals (TZPs) which are nearly single-phase polycrystalline ceramics and are prepared from fine-grained zirconia powders by sintering; (2) Partially stabilized zirconia (PSZ) in which tetragonal-zirconia is precipitate phases in the matrix of cubic zirconia; (3) Zirconia-toughened alumina (ZTA) in which zirconia is a dispersed phase in the alumina matrix. The zirconia attributed this increase in strength to the martensitic transformation occurring during deformation, which was qualitatively explained as follows. This transformation is demonstrated schematically in Fig.3.3. An expanding dilation zone along the front of an initially stationary crack, state a, induces the transformation nearly the frontal crack tip. At a critical zone size the crack commences to propagate, state b. The compressive stress instigates the expansion of transformation area along the crack, so the toughness begins to increase.

[††] Pure zirconia has three allotropic forms: cubic (*c*), tetragonal (*t*) and monoclinic (*m*). At ambient pressure, cubic structure exhibits at high temperatures (> 2370^{O}C), tetragonal structure at intermediate temperatures (1200^{O}-2370^{O}C), and monoclinic at low temperatures (< 950^{O}C)[68].

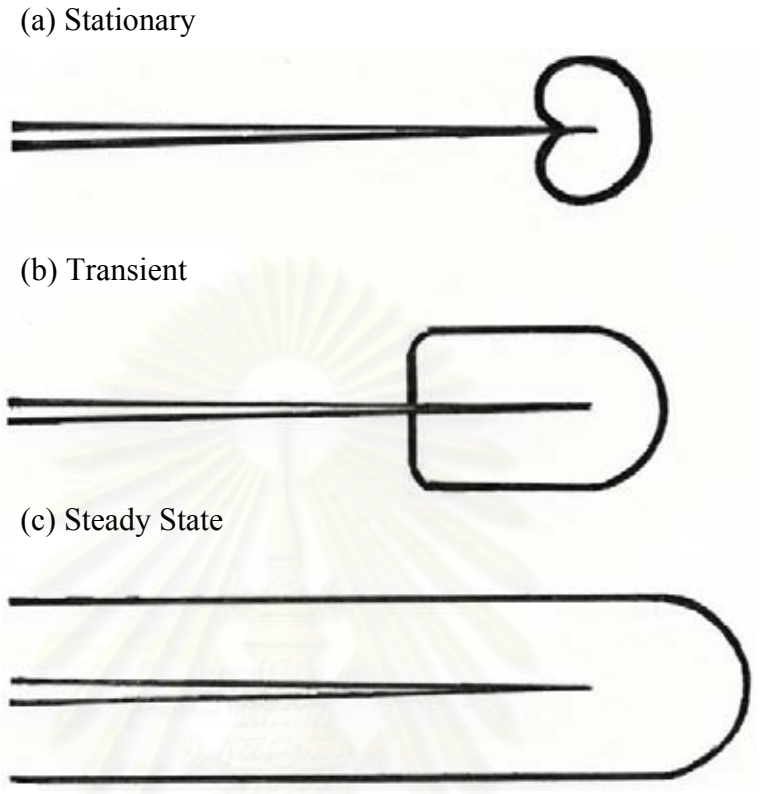

Fig. 3.3 Development of frontal-wake zone with crack extension: (a) zero extension, equilibrium frontal zone; (b) short extension, partial wake; (c) long extension, steady-state wake. Courtesy of Lawn [46].

Finally, after the crack has extended sufficiently that wake is fully developed, state c, due to the compressive stress on the crack saturates, the toughness is constant [46].

Several works demonstrated that the incorporation of yttria in zirconia resulted in a high strength and toughness [80,81]. In addition, Masaki *et al.* proposed that 3 mol % of yttria dispersed in zirconia achieved a good mechanical strength (Fig. 3.4) [82]. Therefore zirconia containing 3 mol % yttria is chosen as the substrate of the bilayer to be fabricated in this work. We use commercial powders from the Tosoh Co. Table 3.2[‡‡] shows the compositions and several mechanical properties of partially stabilized zirconia containing 3 mol % yttria supported by the Tosoh Co.

3.3 Synthesis of Hydroxyapatite with 20 vol % TZ-3Y Powder

HAp powders with uniform dispersion of 20 vol % TZ-3Y powders were synthesized to be used in preparing an intermediate layer between HAp and TZ-3Y layers. Since this layer consists of HAp and TZ-3Y, it is expected that it would improve the adhesion of HAp/TZ-3Y bilayer specimen. We used the coprecipitation method established in Sataporn work (72) in preparing HAp powders with the uniform dispersion of 20 vol % TZ-3Y powders.

[‡‡] The information of TZ-3Y from the catalog of zirconia powders from Tosoh Cooperation, Tokyo, Japan.

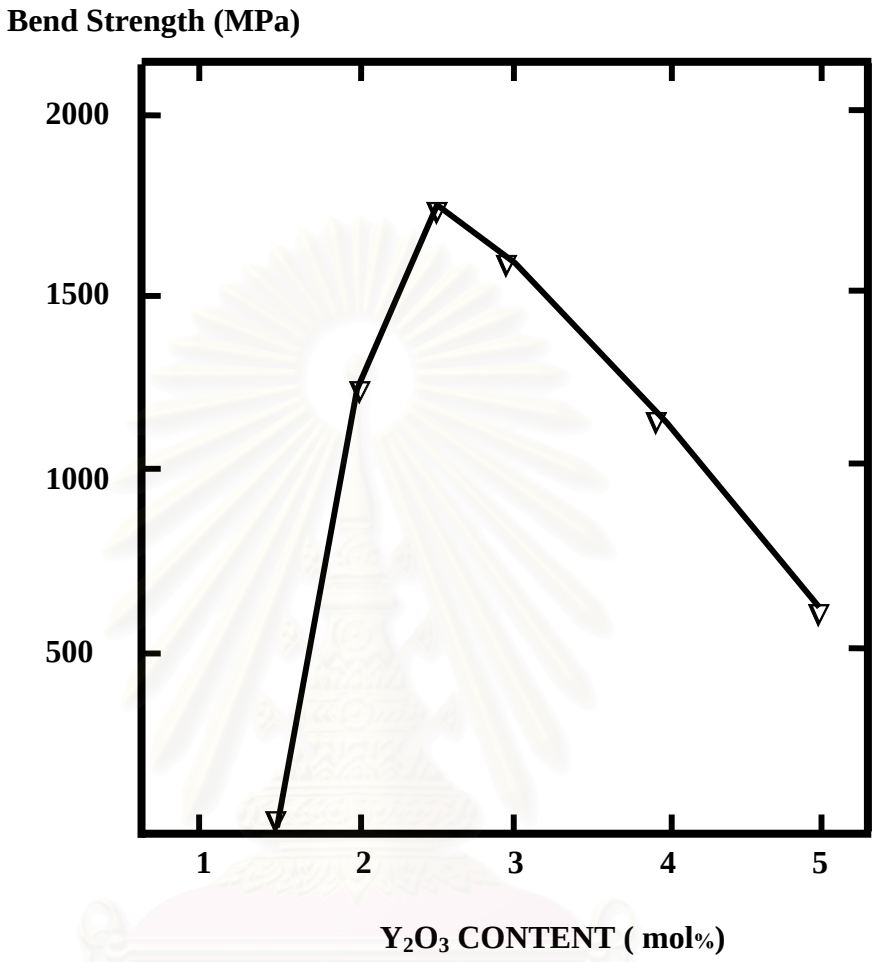

Fig. 3.4 Plot of bending strength as a function of Y_2O_3 content. Courtesy of Masaki [82].

Table 3.2 Compositions and Properties of TZ-3Y.

Composition	Partially Stabilized Zirconia (Y_2O_3)
Y_2O_3 (mol%)	3
Y_2O_3 (wt%)	5.15 ± 0.20
Al_2O_3 (wt%)	≤ 0.1
SiO_2 (wt%)	≤ 0.02
Fe_2O_3 (wt%)	≤ 0.01
Specific Surface Area (m^2/g)	16 ± 3
Density (g/cm^3)	6.05
Bending Strength R.T. (Mpa)	1200
Hardness (HV10)	1250

3.3.1 Synthesizing Procedure of Hydroxyapatite with the Uniform Dispersion of 20 vol% TZ-3Y Powder

The synthesizing procedure of HAp powders with the uniform dispersion of 20 vol % TZ-3Y powders employed in this work is summarized in the flow chart shown in Fig.3.5.

A 78.7 g of $Ca(NO_3)_2.4H_2O$ was dissolved in 300 ml of de-ionized water and brought to pH 11 to 12 with concentrated NH_4OH and finally diluted to 600 ml. A 26.4 g $(NH_4)_2HPO_4$ was dissolved in 500 ml of de-ionized water and brought to pH 11 to 12 with concentrated NH_4OH and thereafter diluted to 800 ml. The pH was checked again and additional concentrated NH_4OH was added if necessary. The pH of the solution was measured using a pH paper. The calcium solution was vigorously stirred at room temperature. Together with the addition of a 14.2 g of TZ-3Ycalcined in air for 1 h at 1200^OC, the prepared $(NH_4)_2HPO_4$ solution was slowly dropwised from a pipet into the vigorously stirred $Ca(NO_3)_2$ solution.

The reaction mixture, which was milky, was continuously stirred at room temperature for 3.5h and then was boiled for 0.5 h and left overnight at room temperature to allow the gelatinous precipitate to settle. The resulting milky solution was suction filtered. The filtered cake was oven dried for 20h at 100^OC , then broken down by crushing in a mortar. The obtained powders were calcined at 240^OC for 1h to eliminate NH_4NO_3 and was heated to 800^OC for 1 h to promote powder crystallinity. Crushing again broke down the agglomerated powders.

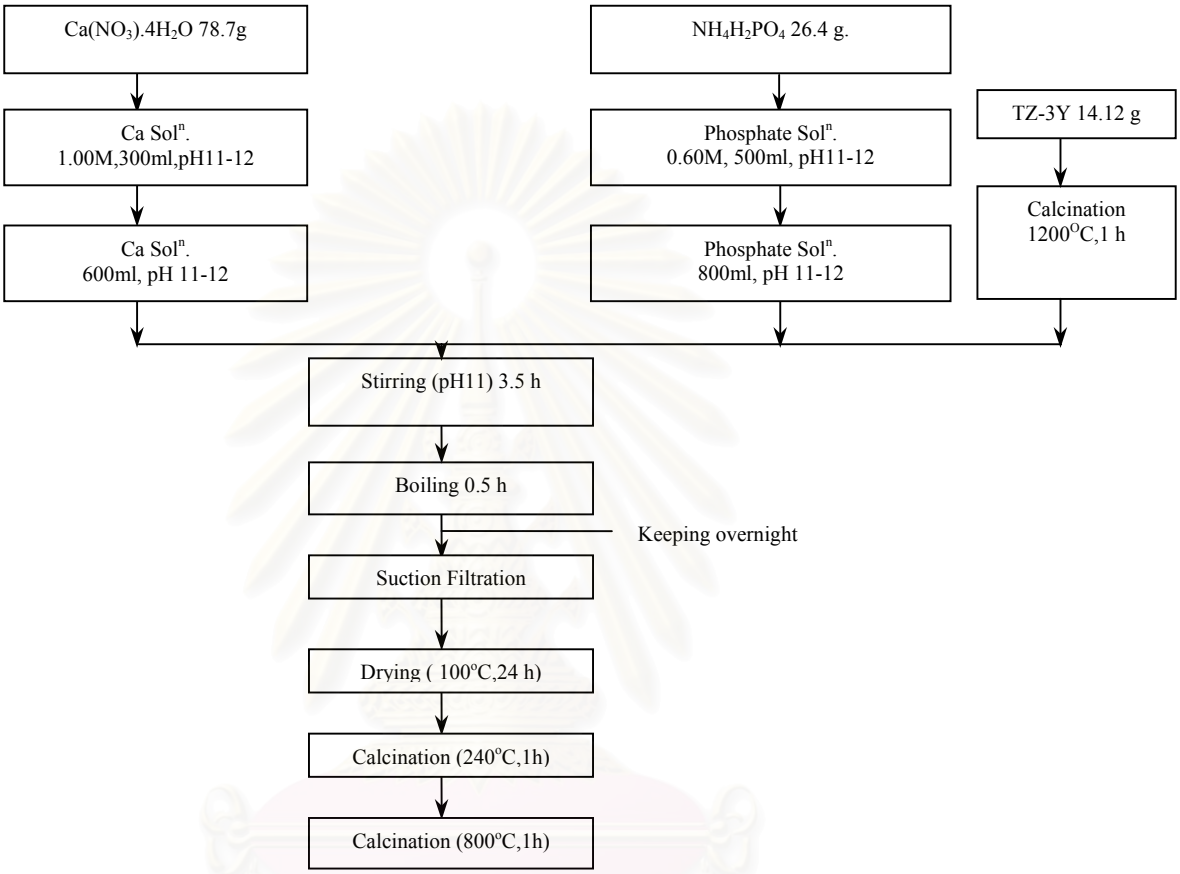

Fig. 3.5 Flow chart for the synthesizing HAp with 20 vol%TZ-3Y procedure employed in this work.

3.3.2 Characterization

The phase composition of the calcined powder was determined by powder X-ray diffractometery (XRD) (model JDX 3530; JEOL, Tokyo, Japan), using $CuK_{\alpha 1,2}$ radiation at 30 mA and 30kV with scanning from $2\theta = 0^{o}$ to 90^{o} in step of 0.04^{o}, each step counted for 0.05s. The XRD pattern (Fig. 3.3.2) of the TZ-3Y-HAp powder is shown along the XRD pattern of HAp and TZ-3Y. Fig. 3.6 showed that XRD pattern of the obtained powders had both HAp and TZ-3Y with tetragonal and monoclinic peaks.

3.4 Fabrication of HAp/ Zirconia Containing 3 mol % Yttria Bilayer Structure

3.4.1 Exploratory Investigation

In the preparation of bilayer structure, there are several factors, need to be considered, such as the appropriate sintering temperature and uniaxial pressure. To enable us to successfully fabricate HAp/ zirconia containing 3 mol % yttria bilayer structure, an exploratory investigation was made to find out the appropriate fabrication procedure to be employed.

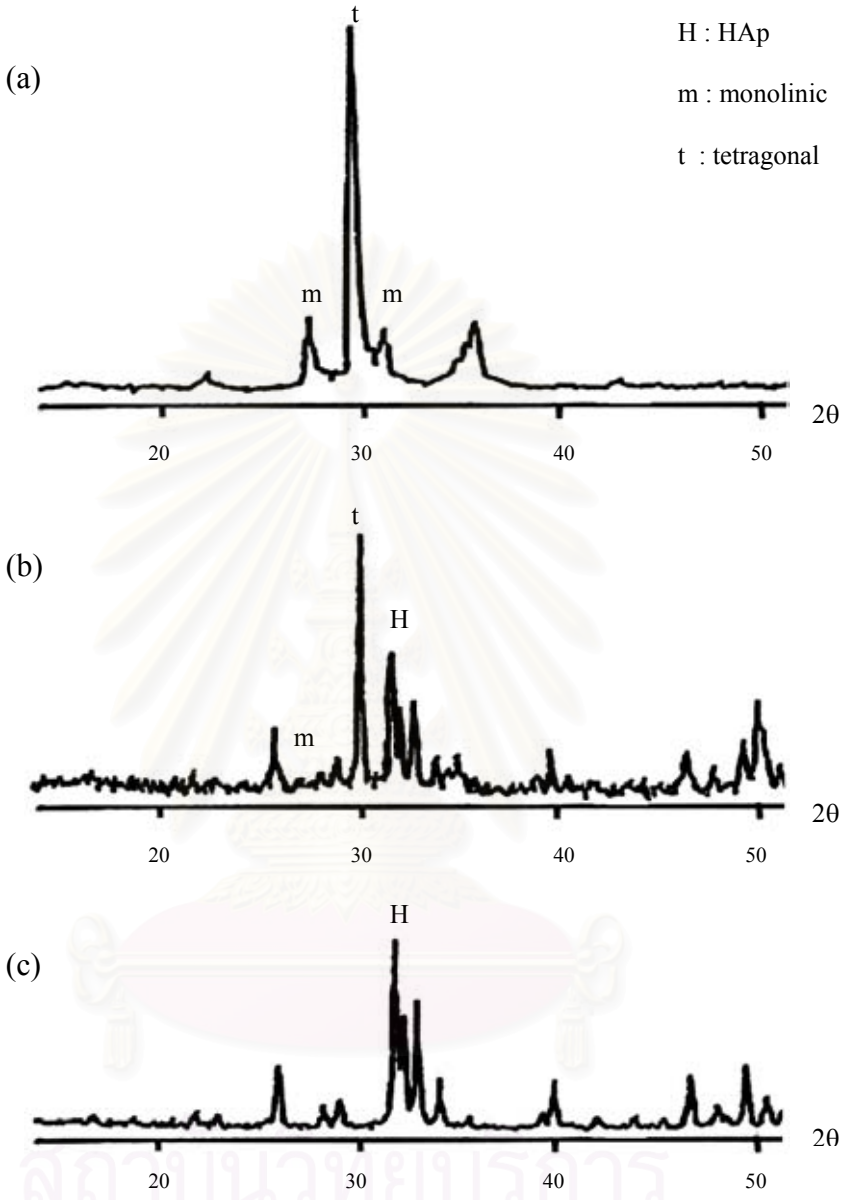

Fig. 3.6 XRD pattern of as-calcined HAp with 20 vol%TZ-3Y showing in comparison with reference datum; (a) reference zirconia; (b) synthesizing HAp with 20 vol% TZ-3Y; (c) reference HAp.

3.4.1.1 Cosintering as a Means to Form HAp/TZ-3Y Bilayer Structure

As an initial attempt, 3 g of HAp powders were single-end die pressed to 30 MPa using a high-purity graphite die, punch and spacer assembly to form a green compact of HAp layer. A green compact of TZ-3Y layer was then form on the top of the HAp layer by adding 5 g of TZ-3Ypowders into the die and applying 60 MPa compressive stress. The obtained green compact of HAp/TZ-3Y bilayer was disc shape of 25.7 mm diameter and 8.2 mm thickness. The green discs were sintered in air with the heating rate of 3 ^{O}C/min from room temperature to a sintering temperature of 1200 ^{O}C (the HAp sintering temperature) for 3 h. The specimens were allowed to cool in the furnace. The heating treatments were carried out in a box furnace (model RHF 17/1CE; Carbolite)

After the heat treatment, the TZ-3Y substrate and the HAp top layer did not bind together. The TZ-3Y layer had larger diameter than the HAp layer. Therefore the difference in the densification of the two layers results in the separation of atoms at the interface of the bilayer. This outcome indicates that it is important to establish data, which would give an indication of the appropriate temperature that should be employed as the cosintering temperature of the HAp/TZ-3Y bilayer.

We then prepared the green compact of each monolith and investigate their diameter variations as a function of sintering temperature. Therefore 3 g of HAp powders were single-end die pressed to 56 MPa using a high-purity graphite die, punch and spacer assembly. The green compact was disc shape of 25.7 mm diameter and 4.1 mm thickness (Fig. 3.7). 5g of TZ-3Y powders were used to prepare the TZ-3Y green compact. The same uniaxial press procedure as that used to prepare HAp green compact was employed in the preparation of the TZ-3Y monolith green compact.

Fig. 3.7 Photograph of the green compact of HAp (25.7 mm diameter and 4.1 mm thickness).

Both HAp and TZ-3Y green compact specimens were sintered in separate batches with the heating rate of 3 ^{O}C/min to the elevated temperatures between 1200^{O}C and 1350^{O}C for1 h. After sintering, the discs were allowed to cool in the furnace. This process was operated in air. Regarding the data of the sintered compacts, the percentage of volume shrinkage and density of each batch were evaluated by using ASTM C 20-80a [83]. The results were summarized in Table 3.3. The obtained data illustrated that the densification of TZ-3Y increases as the sintering temperature increases. The HAp results were summarized in Table 3.4. The results of both TZ-3Y and HAp specimens are resummarized in Fig. 3.8 as a plot of diameter of as-sintered specimen as a function of the sintering temperature in the temperature range of 1200^{O}C to 1350^{O}C. The results indicate that an appropriate cosintering temperature for fabricating the HAp/TZ-3Y bilayer should be 1330^{O}C.

A suitable final uniaxial pressure is another necessary factor needed to be established for this processing. We made an investigation of what would be the appropriate pressure by varying compacting stress between 40 and 60 MPa. The green discs were single-end die pressed to 30 MPa in forming each layer the final uniaxial pressure between 40 to 60 MPa was applied to the bilayer discs. Thereafter the bilayer discs, which were subject to different final pressures, were sintered at the condition as prescribed above. It was observed that all specimens were separated at the interface into two pieces. However the specimens as formed by 60 MPa had a few pieces of HAp on TZ-3Y. From this observation, we therefore used the final uniaxial pressure of 60 MPa

Table 3.3 Densification of monolithic TZ-3Y as a function of sintering temperature between 1200^{O}C and 1350^{O}C.

Temperature(^{O}C)	%Volume shrinkage	Density(g/cm^3)	%theoretical density
1200	16.12	3.54	59.04
1250	38.03	4.14	68.99
1300	43.51	4.99	83.14
1350	51.71	5.59	93.12

Table 3.4 Densification of monolithic HAp as a function of sintering temperature between 1200^{O}C and 1350^{O}C.

Temperature(^{O}C)	%Volume shrinkage	Density (g/cm^3)	%theoretical density
1200	48.59	2.60	82.63
1250	50.77	2.70	85.65
1300	49.69	2.89	91.87
1350	49.25	2.83	89.78

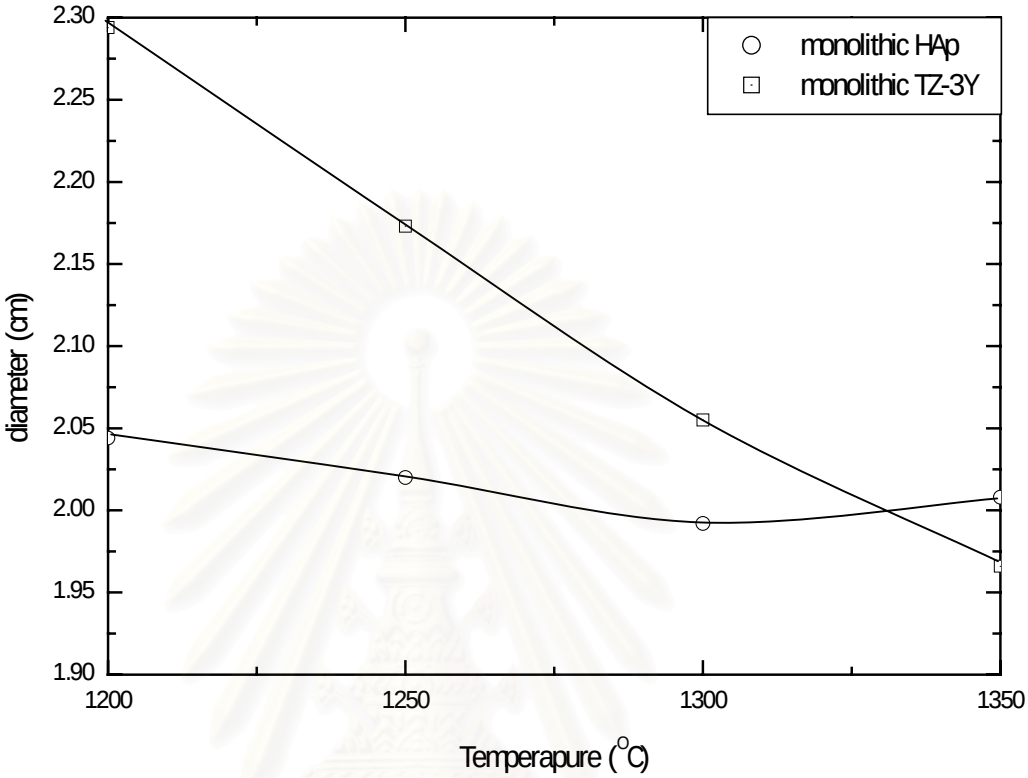

Fig. 3.8 Plot of as-sintered diameter of HAp and TZ-3Y as a function of sintering temperature.

We speculated that it might be an advantage for the adhesion of HAp/TZ-3Y bilayer specimen if an intermediate layer that was a composite of HAp and TZ-3Y was added or another means, if a suitable compressive load was used to form each layer of HAp/TZ-3Y bilayer. Therefore the bilayer structure with an intermediate layer was prepared by adding HAp with 20 vol%TZ-3Y, thin layer, between HAp and TZ-3Y layers. The uniaxial pressure of 60 MPa and the sintering temperature of $1330^{O}C$ were used in preparing these specimens. We found that the intermediate layer had larger diameter than adjacent layers and the samples did not bind together (Fig. 3.9).

Another means, we varied the compressive load that was used to form each layer and found that the suitable compressive load should be about 10 MPa.

Finally in forming the green compact of the bilayer, we fixed the thickness of TZ-3Y substrate by using 5 g of TZ-3Y powder while varing the thickness of HAp layer by using various weights of 2, 3, 4, 5 and 6 g. The as-fired bilayer structures of different HAp top layer thickness are shown in Fig.3.10. The good interface between adjacent layers when HAp weights of 2, 3, and 4 g were used on forming the top HAp layer, was apparent. When the top layer was thick, a part of it peeled of from laminate (as shown in Fig.3.10 (b, and c)). In addition, the crack paralleling to the interface was observed in the top layer of 5 and 6 g of HAp weight. As the result, the HAp layer of moderate thickness (3 and 4 g of HAp powders) was selected for using in this bilayer structure preparation.

Fig. 3.9 Photograph of trilayer laminate consisting of HAp top layer and TZ-3Y substrate with intermediate thin layer of HAp with 20 vol%TZ-3Y.

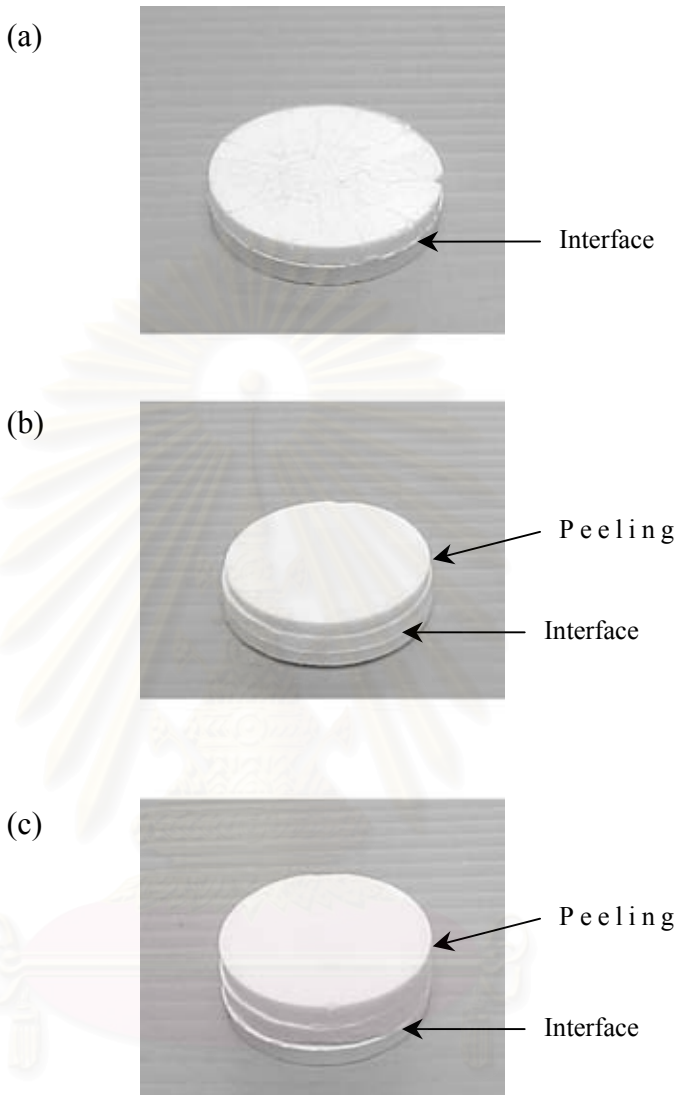

Fig. 3.10 Photographs of as-fired HAp /TZ-3Y structures having various HAp layer thickness : (a) HAp weight = 2 g; (b) HAp weight = 3 g ; (c) HAp weight = 5 g.

3.4.1.2 Cosintering as a Means to Form HAp/TZ-3YE Bilayer Structure

A new improved zirconia containing 3mol% Y_2O_3 powders, TZ-3YE, are developed and supplied by the Tosoh, Co. These new grades of partialy stabilized zirconia powder exhibits lower sintering temperature than TZ-3Y therefore TZ-3YE would seen to match with HAp better than TZ-3Y.

Before fabricating HAp /TZ-3YE bilayer using the same method described in Sect. 3.4.1.1, as a function of sinteringtemperature was explored and summarized in (Table 3.5). The as-fired diameter of TZ-3YE monolith was plotted as a function of the sintering temperature between 1200^{O}C and 1350^{O}C along with the densification data of HAp in Fig.3.11 . It can be seen in Fig. 3.11 that the most suitable cosintering temperature that would be used to fabricate HAp/TZ-3YE is 1250^{o}C. It is closer to the sintering temperature of HAp monolith than the cosintering temperature of HAp /TZ-3Y bilayer. Unfortunately, the obtained HAp/TZ-3YE specimens were similar to HAp/TZ-3Y bilayer specimens.

According to these investigations, we prepared both HAp/TZ-3Y and HAp/TZ-3YE bilayers.

Table 3.5 Densification of monolithic TZ-3YE as a function of sintering temperature between 1200^{O}C and 1350^{O}C.

Temperature(^{O}C)	%Volume shrinkage	Density (g/cm^{3})	%theoretical density
1200	36.03	3.87	64.51
1250	50.59	5.02	83.60
1300	56.67	5.73	95.47
1350	58.55	5.94	99.07

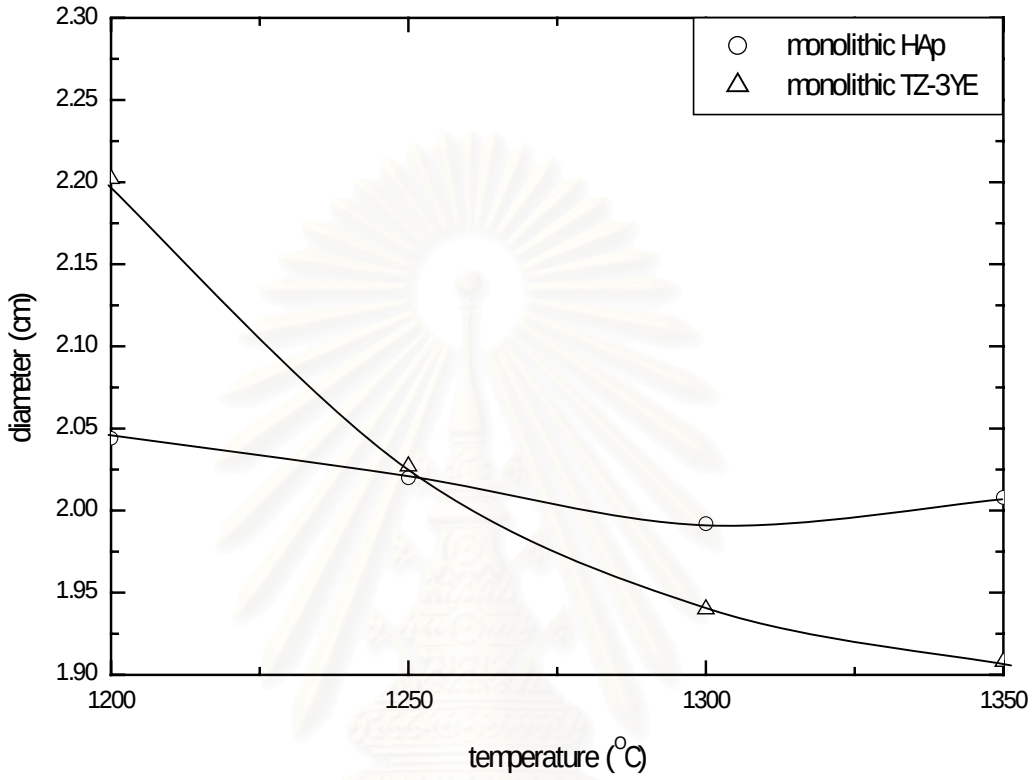

Fig. 3.11 Plot of as-sintered diameter of HAp and TZ-3YE as a function of sintering temperature.

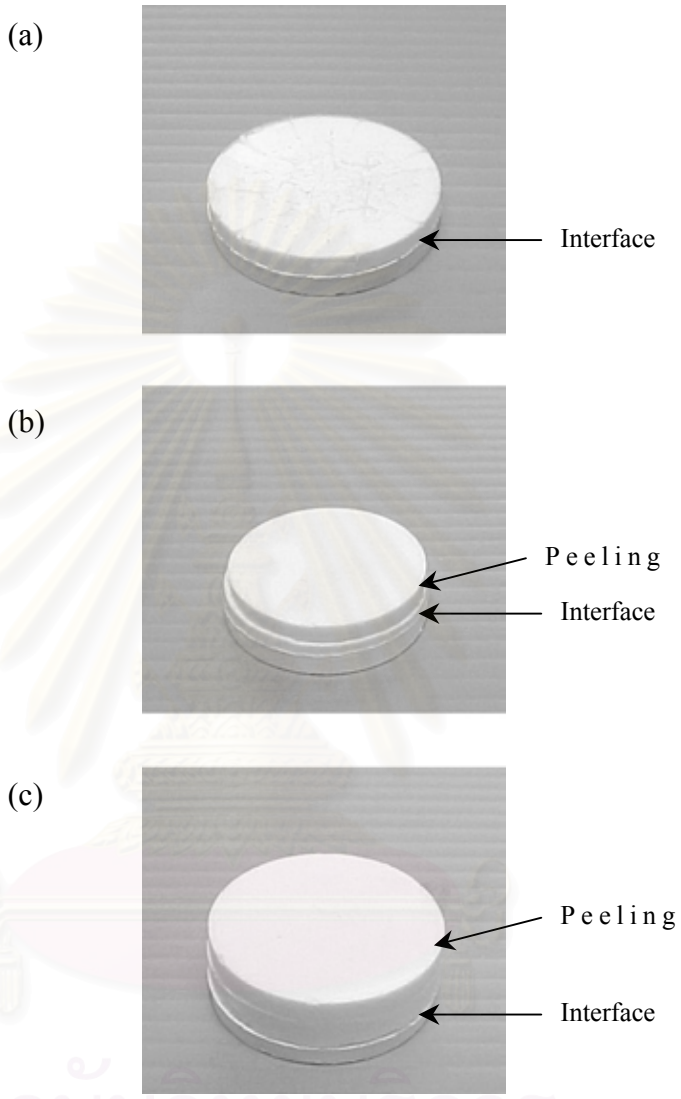

Fig. 3.12 Photographs of as-fired HAp /TZ-3YE structures having various HAp layer thicknesses: (a) HAp weight = 2 g; (b) HAp weight = 3 g; (c) HAp weight = 5 g.

3.4.2 Fabrication Procedure

The fabrication procedure of cosintering bilayers is summarized in a flow chart shown in Fig. 3.13.

To facilitate in bilayer structure, the green forming of bilayers was prepared by die pressing method. The bilayers consisted of HAp as the top layer and TZ-3Y or TZ-3YE as the substrate. The procedure of die pressing started with single-end die pressing four grams of HAp powders under about 10 MPa. Then, five grams of TZ-3Y (or TZ-3YE) was added on top of the finished HAp in die cylindrical tube and was die pressed under 60 MPa. A green compact of HAp/TZ-3Y (or HAp/TZ-3YE) was then obtained. The compact has a disc shape of 25.7 mm in diameter and about 8 mm thick. Thereafter, several green discs prepared by the same method were heated at a rate of 3^{o}C/min until they reached suitable sintered temperatures –1330^{o}C and 1250^{o}C for HAp/TZ-3Y and HAp/TZ3YE, respectively. After sintering, the discs were allowed to cool in a furnace.

Now, we come to the physical properties testing procedure for the discs. The delamination along the interface of the bilayers was first tested by a primitive method – cross-sectional cut. A diamond saw was used to cut through the specimens. The results shown that the bilayer discs, after heated, were not delaminated. So, the interface is sufficiently strong.

The final quality check on the specimens was examining their top surfaces of HAp layer, which were polished with 1 μm diamond suspension finish to 1mm thickness using a microscope. Fig 3.14 shows how the surface looks like when viewed by a microscope. We can see that there are many flaws all over the surfaces. The flaws on the top surface increase as the top layer's thickness decreases.

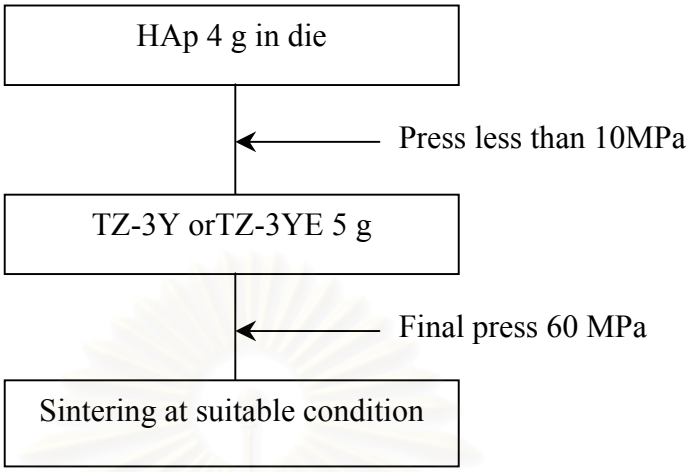

Fig. 3.13 Flow chart for the fabrication procedure employed in this work.

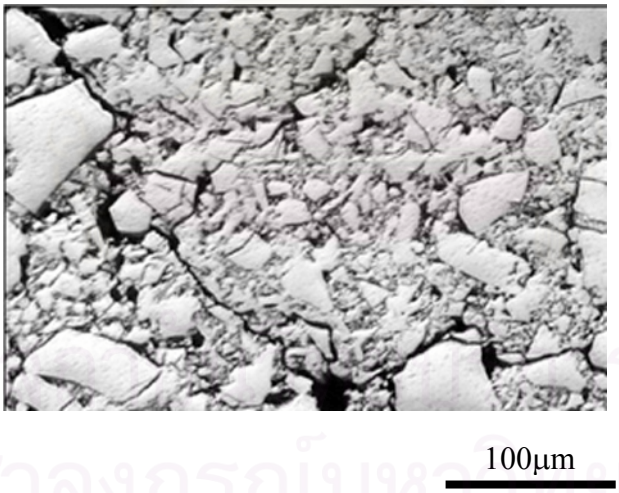

Fig. 3.14 Photograph of HAp surface at 1mm above interface that were polished to 1 μm diamond suspension finish.

Moreover, the patterns of the flaw on the surface of HAp/TZ-3Y bilayers are similar to those found in surfaces of HAp/TZ-3YE bilayers.

The causes of the cracks might come from three different physical properties of the two layers: different sintering shrinkage, varying strength, and thermal expansion coefficients mismatch. I found that the thermal expansion coefficients of HAp and TZ-3Y are $13.9 \times 10^{-6}\ {}^{O}C^{-1}$ and $12.1 \times 10^{-6}\ {}^{O}C^{-1}$, respectively. To analyze the sintering induced cracking is not easy because it depends on relative sintering temperature and the different in shrinking rate between the two layers. Another factor is the changing strengths (or toughnesses) during sintering. The presence of cracking normal to the HAp layer in the case of thin layers might suggest that the HAp begin sintering at lower temperature than the zirconia (TZ-3Y, TZ-3YE), thus generated tensile residual in- pane stresses. For thicker HAp layers the stresses would be lower. The cracking parallel to the interface for the thick HAp layers could be driven by larger shrinkage in either component, depending on relative strengths and stiffness at the time cracking.

We have, then, seen that although the finished specimens prepared by the die pressing and sintering procedure have sufficiently strong interface of the HAp /TZ-3Y (or TZ-3YE) structure, they are not presumably not good enough to be tested by indentation test. The indentation test is a test to evaluate several mechanical properties of the specimens; including cracking propagations, which are measured by indenter. Because the presence of the flaws on the surfaces of the specimens is too many and too large, the indentation test could cause confusion and miscalculation of the specimens' mechanical properties.

3.4.3 Fabricating HAp /TZ-3YE Bilayer via Adhesive Polymer

As the result of previous systems, they are not suitable to indentation testing, which is used to evaluate some mechanical properties. To enable the possibility of an investigation of the mechanical response to stresses of the hydroxyapatite/tetragonal zirconia bilayer structure, an alternative processing procedure is employed.

The bilayer structure consists of HAp coating glued to TZ-3YE substrate by adhesive polymer. HAp and TZ-3YE powders of the weight of 3 g and 5 g, respectively, was single-end die pressed to 56 MPa. The obtained green discs were then subjected to cold isostatic pressing (CIP) at 180 MPa before being sintered in air for 1 h at 1250^{o}C, with the heating a rate of 3^{o}C/min.

To form the bilayer structures, top and bottom surfaces of HAp and TZ-3YE discs were polished to 1 μm diamond suspension finish. Then discs were cleaned with distilled water and dried in hot air. To bond the HAp top layer onto TZ-3YE substrate the following procedure was carried out (Fig3.15): (i) set HAp and TZ-3YE discs on the clamp, placed on the opposite sides; (ii) apply cyanoacrylate adhesive to capillarity between HAp and TZ-3YE discs; (iii) bond these layers together by applying slightly compressive pressure so as to control the interlayer thickness. Then the bilayers were clamped and left for one hour in air. The resultant bilayer contained a bond interlayer of thickness ≈10 μm. Thereafter the bilayer structures were cut into bars 2.5 x 5 x 20 mm as shown in Fig. 3.16.

The indentation testing procedures of these specimens will be given in detail in the next section and the results of indentation testing will be shown in chapter 4.

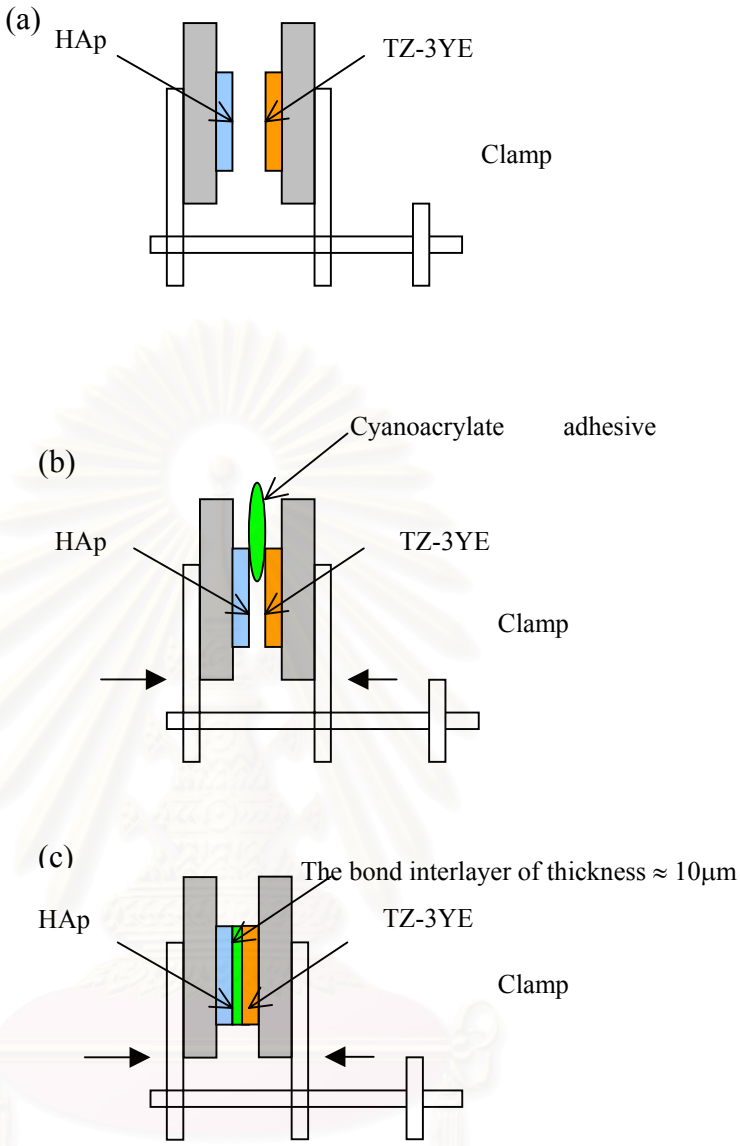

Fig. 3.15 Schematic bonding procedure used to prepare bilayer structure: (a) set the discs on the clamp; (b) apply the cyanoacrylate adhesive to capillarity; (c) bond the discs together.

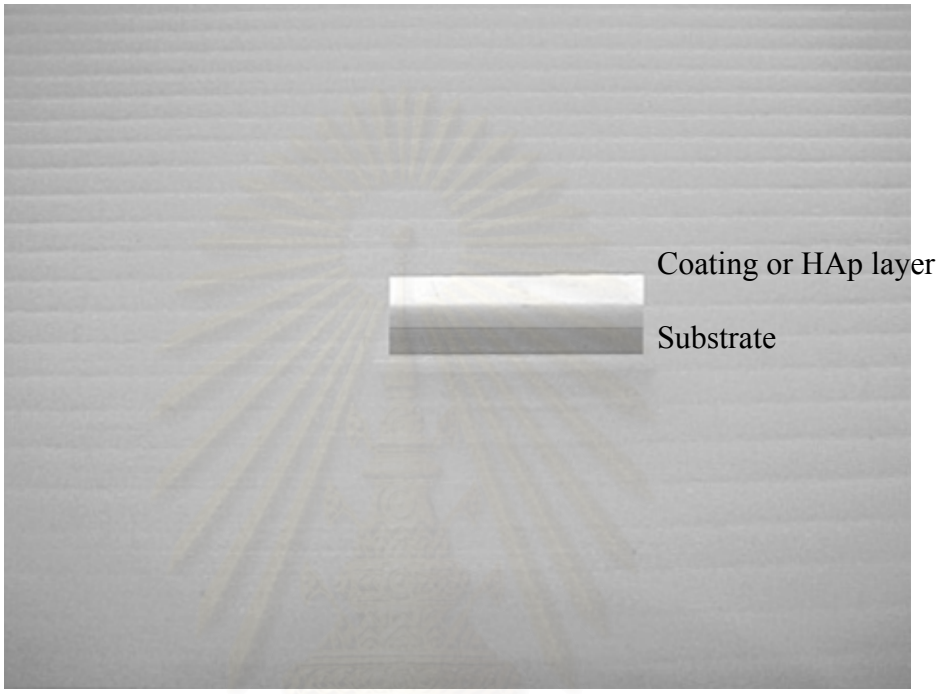

Fig. 3.16 Bilayer structure consisting of HAp layer on TZ-3YE substrate.

3.5 Indentation Tests

In this thesis, indentation techniques are used to evaluate fracture toughness and examine the effect of contact load on both monolithic specimens (HAp and TZ-3YE) and HAp/TZ-3YE bilayer structure, of different thicknesses of the HAp layer.

3.5.1 Vickers Indentation

Vickers indentations were used to evaluate the hardness and the fracture toughness. In order to be able to observe its deformation/fracture patterns produced by Vickers indentation, the preexisting damages on specimen surfaces have to be removed by grinding and polishing with successively finer abrasive powders to obtain an optical finish.

For the monolithic specimens, the optimum surface-removing procedure was achieved by polishing the specimen surface with a series of SiC paper (600, 800, 1200 mesh), and a series of diamond suspension (6, 3, 1 μm). When the polishing process was completed, the monolithic HAp and TZ-3YE were indented by Vickers indentation at load range of 9.8 to 49 N and 9.8 to 98 N[§§], respectively, by using a hardness-testing machine (Zwick). Loading of the indentation was under dead-weight condition with rates controlled an adjustable dashpot (loading velocity 1 mm s^{-1}), unloading was by hand and was somewhat more rapid. The peak contact load was maintained of 10-15 s. During indentation, care was taken to maintain the indentation

[§§] From Vitun work, he reported that Vickers indentation test over load range P = 9.8 – 98 N was suitable to evaluate the hardness and toughness of TZ-3YE.

axis parallel to the surface normal of specimen and indents spaced far enough apart that no measurable crack interactions occurred. Specimen surfaces, the indenters and the indentation stage were well cleaned with solvents prior to indenting. All indentations were made in ambient air. After indentations, the deformation/fracture pattern of the indented specimen was examined by an optical microscope operated in reflected light.

Bilayer specimens were then ground and polished to 1 μm diamond suspension finish, to produce final HAp layer thickness, *d*, about 800, 600 and 400 μ m . The top layer thickness should be accurate, this thickness from one edge to the other could be slightly error (≤ 50 μm). It is not easily to grind them therefore we design the controlling clamp (Fig. 3.17) for using in this process. When the polishing process was completed, the Vickers indentation method using the same method described in monolithic specimens was used to introduce contact damage to the bilayer. The Vickers indentation were performed on the top surface of bilayer specimens over a load range P = 9.8-49 N, in air. Fig.3.18 shows schematic testing configuration for Vickers indentation on the bilayer.

The evaluation of hardness and toughness was analyzed by using Eqs. (2.1) and (2.2), respectively.

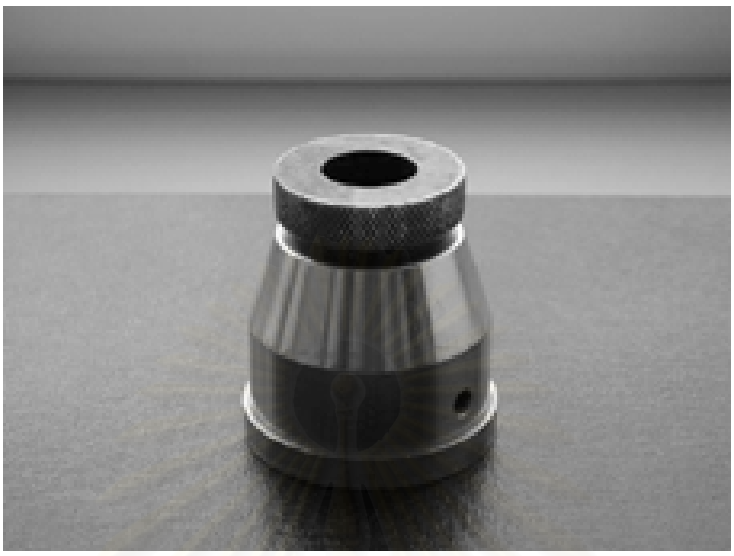

Fig. 3.17 Photograph of the controlling clamp.

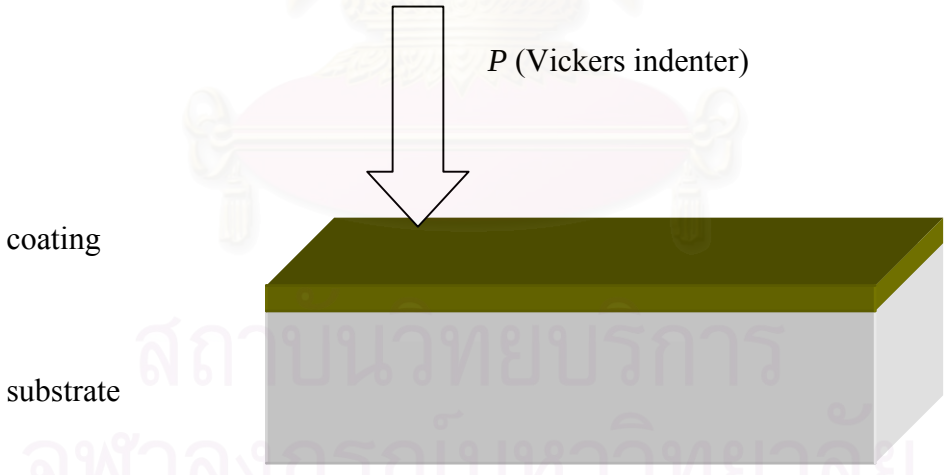

Fig. 3.18 Schematic testing configuration for Vickers indentation.

3.5.2 Hertzian Indentation

Hertzian indentations were introduced on the specimen surface by blunt indenter. The contact damage on bilayer structure specimens, which is various thicknesses of top layer are observed.

Hertzian indentation techniques together with bonded-interface techniques are used to observe the damage pattern of blunt indentation beneath surface. The half-bilayer specimens were ground and polished normal to the layer interface. Two of the polished half specimens were placed on metal plate and joined together by clamp, (Fig.3.19). Then the bonded-interface specimen was polished on the top HAp surfaces to the required thickness, *d.*

A sequence of indentations was subsequently made along the bonded-interface trace on the test surfaces, with WC sphere of radius r = 3.96 mm in a screw-driven testing machine (Instron 4501,Instron Corp, Canton, Ma) in air, taking special care to keep the contacts centered across this trace, and applying a clamping stress normal to the interface to minimize intersurface separation. After indentation, the specimen halves were separated. Then, the reflection optical microscopy using Nomarski interface contrast was used to examine the fracture pattern in section view.

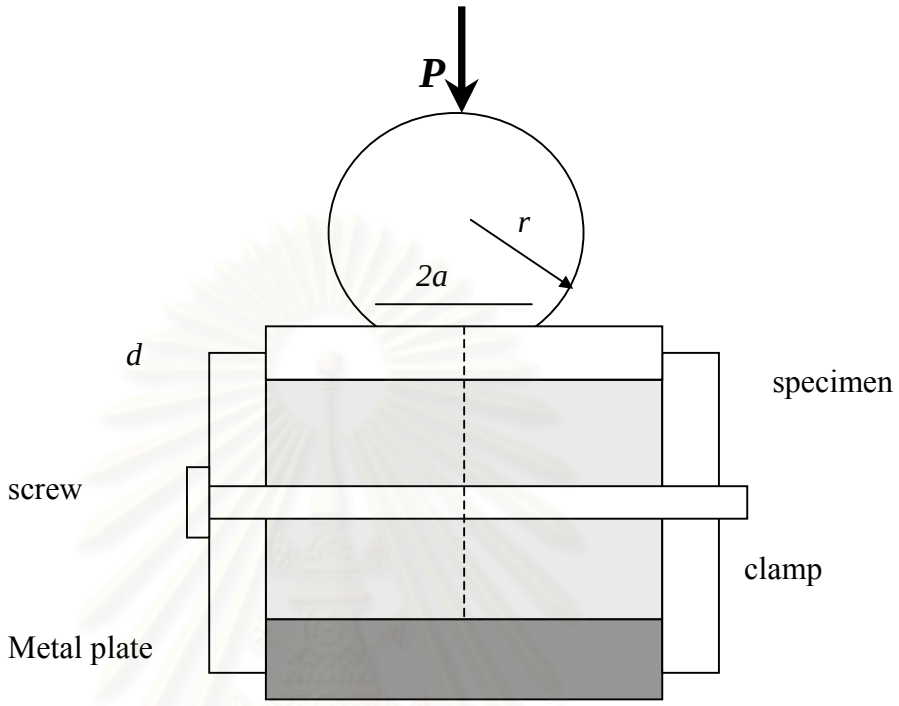

Fig. 3.19 Schematic Hertzian indentation on top coating surface in HAp/TZ-3YE bilayer structure.

CHAPTER IV

RESULTS, DISCUSSION AND CONCLUSION

4.1 Response of Monolithic HAp to Vickers Indentation

The response of monolithic HAp to the Vickers indentation is presented in two parts: the first part is a qualitative description of the deformation and fracture behavior, and its quantitative results is presented in the second part.

Firstly, the main observations of the influence of indentation load on the HAp surface are the followings:

(i) Cracking occurs even for the load as low as 1 N. Fig. 4.1 shows the observed damage pattern due to 9.8 N.

(ii) Cracks are of two types: median/radial and lateral. The median/radial cracks form on the two mutually orthogonal median planes of symmetry defined in each case by the indentation axis and one of impression diagonals. The lateral cracks form nearly parallel to the specimen surface and center beneath the contact zone. The deflection of the lateral crack towords the specimen surface is evident in Fig. 4.2 (a) as surface trace (L) on the top right quarter of the damage pattern.

(iii) The higher the indentation load, the more severe the damage pattern. Fig. 4.2 shows the observed damage pattern due to 29.4 N load in comparison with that due to 49 N load. Apart from the longer radial traces due to the 49 N load, the higher the indentation load, the more lateral cracks intersect the specimen surface as evident in Fig. 4.2 (b). For the indentation load above 49 N, the residual impression corner on

(a)

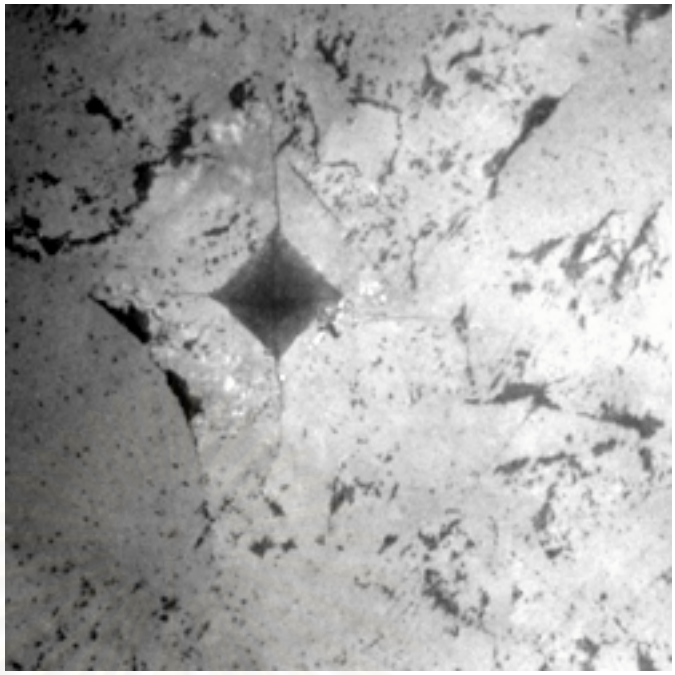

(b)

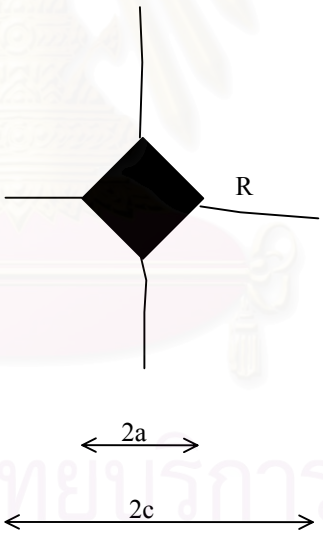

Fig. 4.1 Optical micrograph and schematic of Vickers-produced damage patterns on surface of monolithic HAp indented with 9.8 N; where *a* and *c* are dimension of impression half-diagonal and crack length, respectively.

(a) optical micrograph, (b) schematic diagram. Also label in (b) is radial (R) crack and residual impression (shaded).

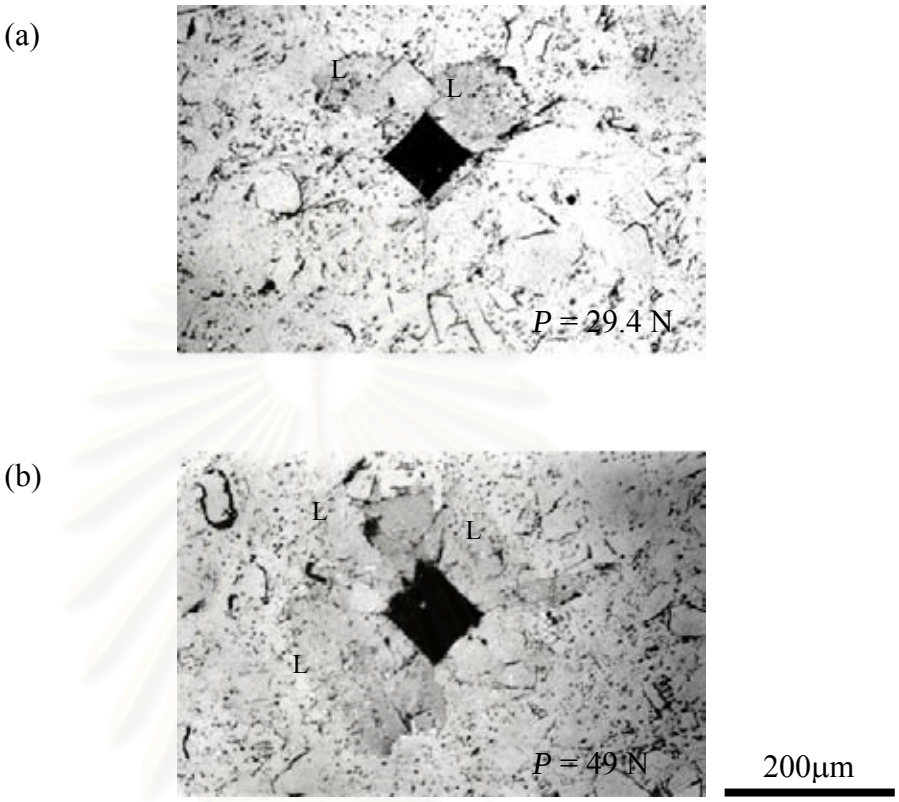

Fig. 4.2 Optical micrographs of Vickers-produced damage patterns on surface of monolithic HAp at two different indentation loads *P*. (a) *P* = 29.4 N; (b) *P* = 49 N.

surface is no longer well defined and the lateral cracks produce so intense surface chipping that the crack pattern are no longer seen.

As the corner of residual impression due to the indentation loads > 49 N are not well-defined, only tests performed in the 9.8 to 49 N load range were retained for hardness measurements. Fig. 4.3 is a plot of the impression half-diagonal, a, as a function of the indentation load, P. The dimension of impression half-diagonal for each indent was measured as average over the two half-diagonals. Each data point in Fig. 4.3 represents the mean and standard deviation of three indentations. The result illustrated in Fig. 4.3 has established that the dimension of impression half-diagonal in HAp follows the 1/2 power dependence of indentation load ($a \alpha P^{1/2}$). Thus the above-obtained dependence of a on P implies that Eq. 2.1 is the equation to be used for evaluating hardness, H, for the monolithic HAp. Fig. 4.4 resummarizes the results of impression half-diagonal measurements as a plot of P/a^2 as a function of indentation load P and the fitted line is the mean over all indentations. It can be seen from such a plot that the mean value of P/a^2 = 8.71 ± 1.26 GPa. From Eq. 2.1 along with the mean value of P/a^2, we obtain the hardness of monolithic HAp to be 4.35 ± 0.63 GPa.

In the same manner as above, the radial crack length was measured as a function of indentation load. Again due to difficulties in accurately measuring radial crack length when P > 49 N, tests performed in the 9.8 to 49 N load range were retained for the radial crack length measurement. The indentation load dependence of the radial crack length, c, is shown in Fig.4.5. Each radial crack length was measured as average over the four radial traces. Each data point in Fig. 4.5 represents the mean and standard deviation of three indentations. The slope of c-P curve in Fig. 4.5 is 2/3.

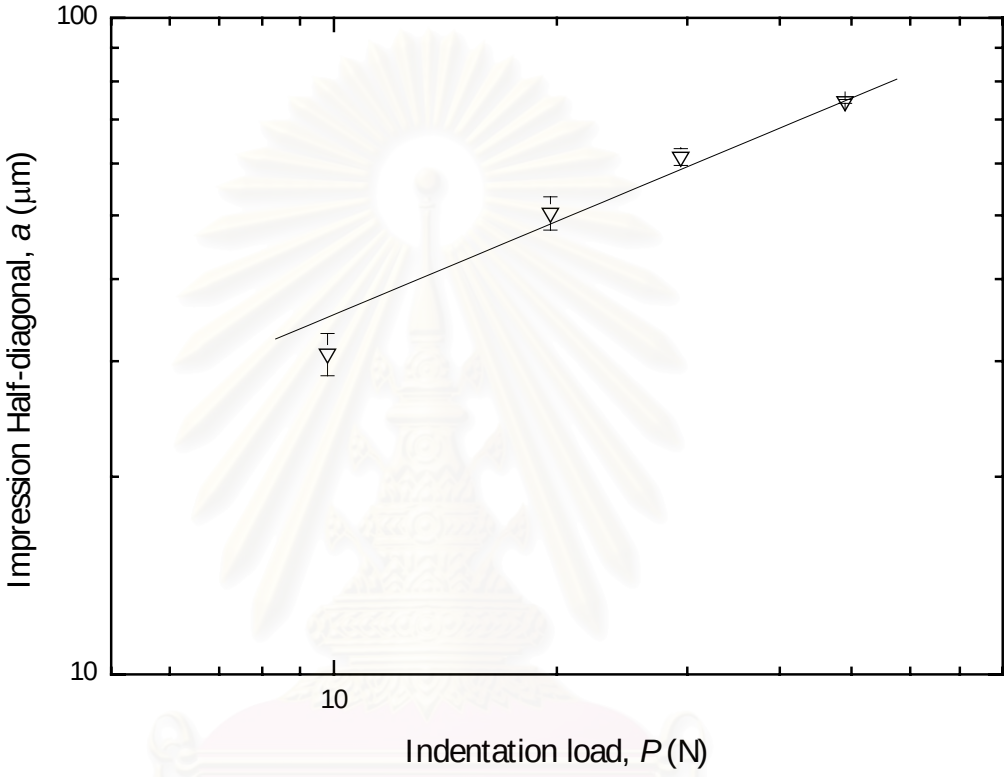

Fig. 4.3 Plot of impression half-diagonal on HAp surface as a function of indentation load.

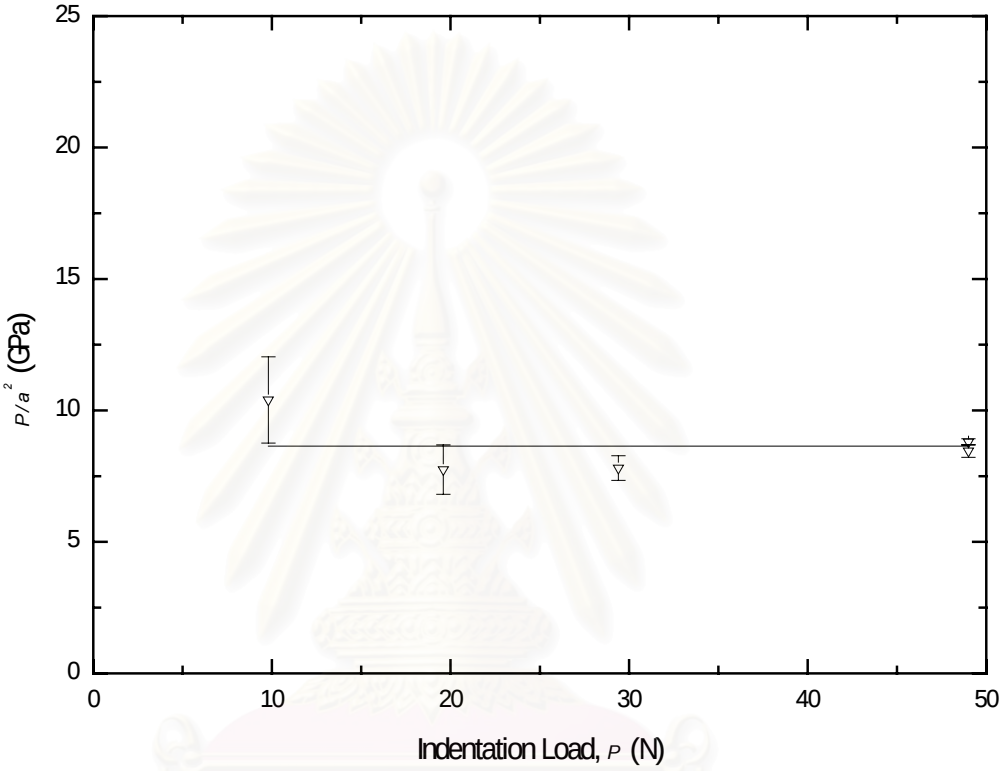

Fig. 4.4 Plot of P/a^2 as a function of indentation load of monolithic HAp.

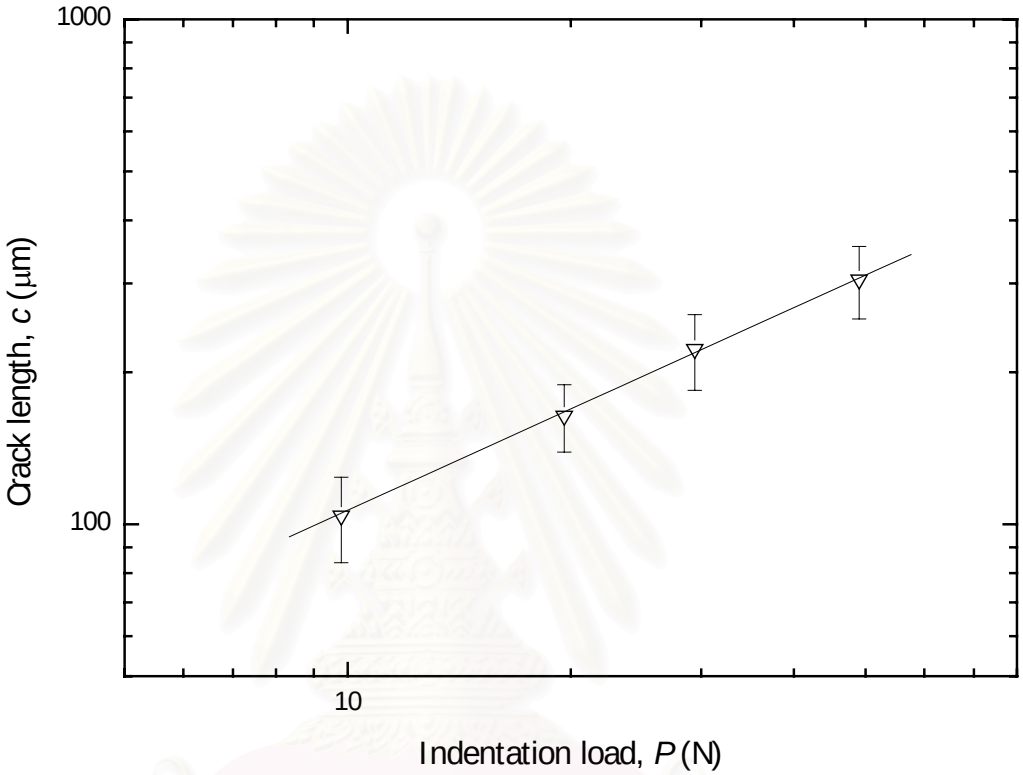

Fig. 4.5 Plot of radial crack length on HAp surface as a function of indentation load.

Thus the result illustrates in Fig. 4.5 has established that the dimension of the radial crack in monolithic HAp follows Eq. 2.2 ($c \alpha P^{2/3}$). Fig 4.6 resummarizes the result of crack measurements as a plot of $P/c^{3/2}$ as a function of indentation load P and the fitted line is the mean over all indentations. The mean value of $P/c^{3/2}$ = 9.17 ± 0.20 $MPam^{1/2}$. By using Eq. 2.2 along with the mean value of $P/c^{3/2}$, we obtain the fracture toughness of monolithic HAp to be 0.58 ± 0.01 $MPam^{1/2}$.

4.2 Response of Monolithic TZ-3YE to Vickers Indentation

In this section, the response of monolithic TZ-3YE to Vickers indentation is presented. Again the response of monolithic TZ-3YE to the Vickers indentation will be presented in two parts: a qualitative description of the deformation and fracture behavior is presented in the first part, and the quantitative results is presented in the second part.

The main observations of the influence of indentation load on the TZ-3YE surface are the followings:

(i) The radial crack traces on the specimen surface is observed when the load ≥ 9.8 N. Fig. 4.7 (a) presents the observed damage pattern due to 9.8 N.

(ii) Over load range P = 9.8 to 98 N, only the radial crack traces emanating from the impression corners are observed. The observed damage patterns due to 29.4 N load in comparison with that due to 49 N load are shown in Fig. 4.7.

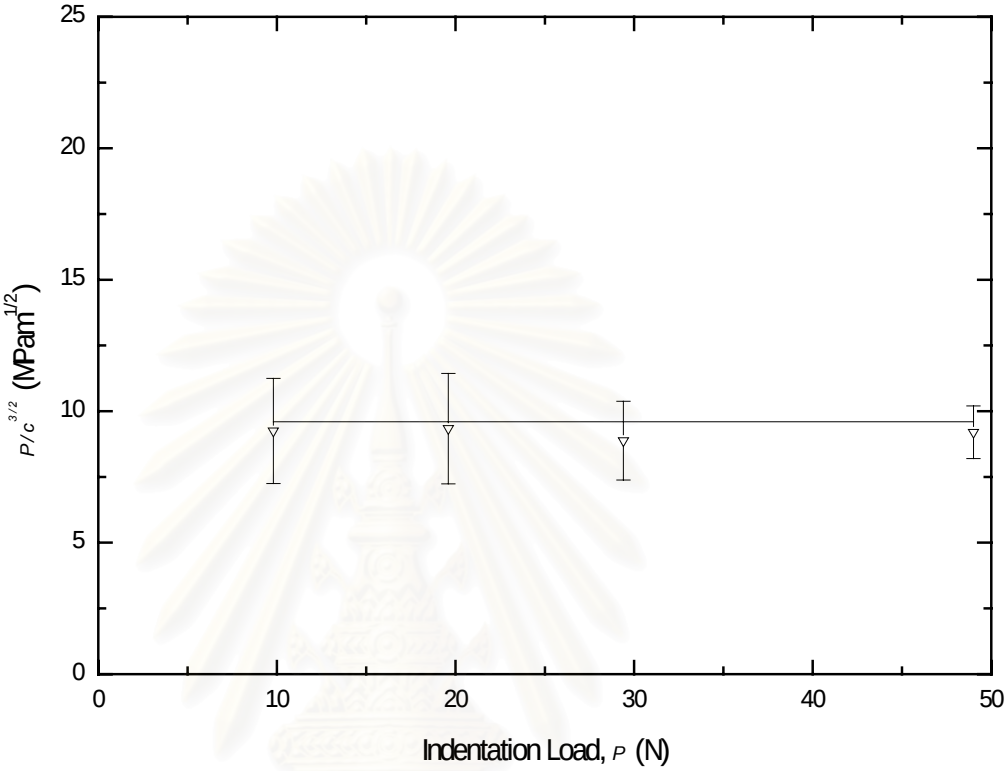

Fig. 4.6 Plot of $P/c^{3/2}$ as a function of indentation load of monolithic HAp

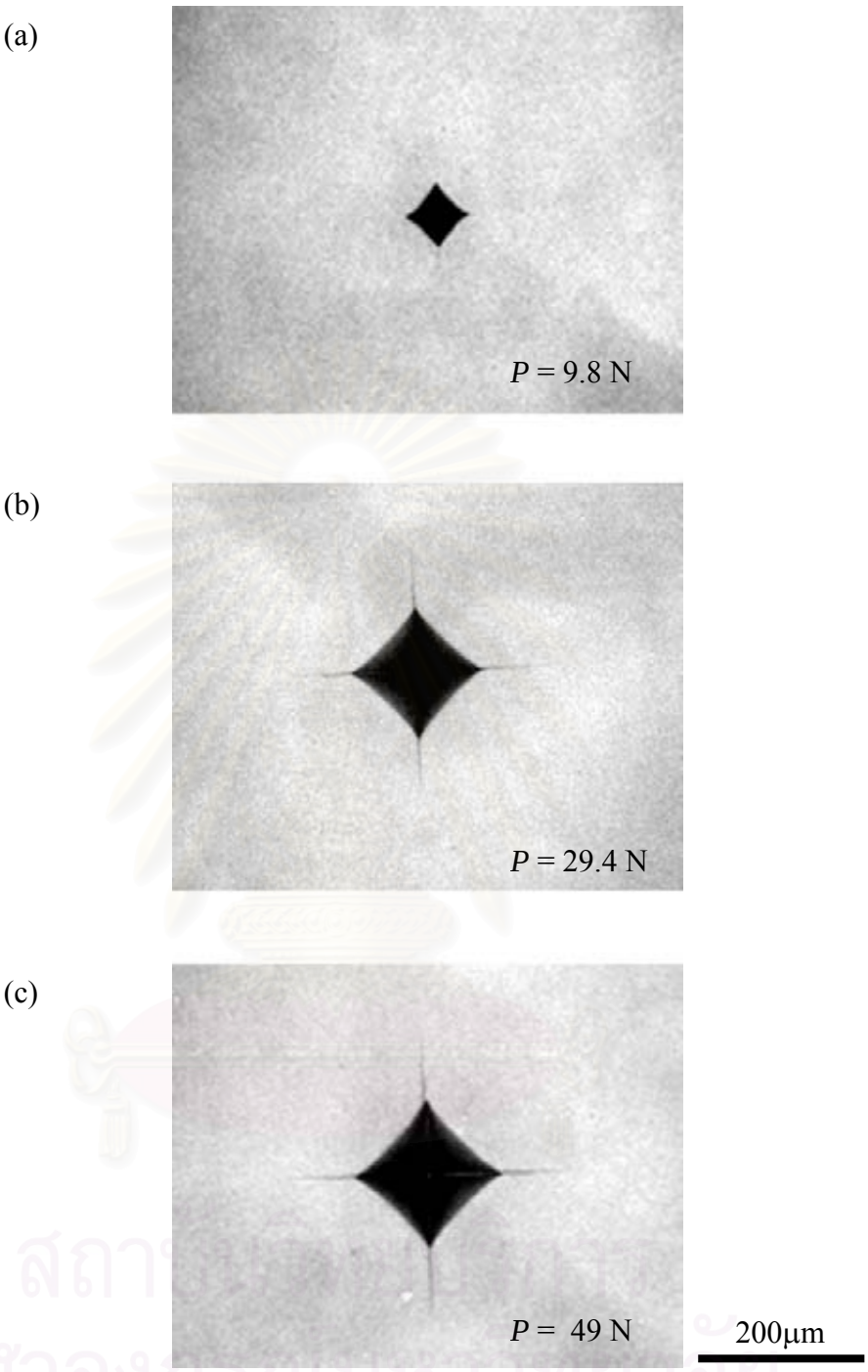

Fig. 4.7 Optical micrographs of Vickers-produced damage patterns on surface of monolithic TZ-3YE at three different indentation loads *P*. (a) *P* = 9.8 N; *P* = 29.4 N; and (c) *P* = 49 N.

The corner of residual impression due to the 9.8 to 98 N load range were well-defined, therefore these indentation load range was retained for hardness measurement. The plot of the impression half-diagonal on the TZ-3YE surface, a, as a function of the indentation load, P, in the range of 9.8 to 98 N is shown in Fig. 4.8. Each data point shows the mean and standard deviation of three indentations. It indicates that the dimension of impression half-diagonal on the TZ-3YE surface follows the 1/2 power dependence of indentation load. The plot of P/a^2 as a function of indentation load P is shown in Fig. 4.9. The solid line depicts the mean value of P/a^2. The mean value is 30.48 ± 1.91 GPa. Using Eq.2.1 along with the mean value of $(P/a^2)_{TZ\text{-}3YE}$ we obtain $H_{TZ\text{-}3YE}$ = 15.34 ± 1.07 GPa.

Since for the indentation load lower than 9.8 N the radial crack on the specimen surface is not easy to observe, tests performed in the 19.6 to 98 N were retained for the radial crack length measurement. Fig. 4.10 is the plot of the radial crack length on the TZ-3YE surface, c, as a function of the indentation load, P. Each data point is the mean and standard deviation of three indentations. The slope of c-P curve is about 2/3. Consequently, the results of impression diagonal measurements are replotted between $P/c^{3/2}$ and indentation load P in Fig. 4.11. The solid line depict the mean value of $P/c^{3/2}$. The mean value is 73.55 ± 6.49 $MPam^{1/2}$. By using Eq. 2.2 along with the mean value of $P/c^{3/2}$, the fracture toughness of TZ-3YE specimen is found to be 4.23 ± 0.43 $MPam^{1/2}$.

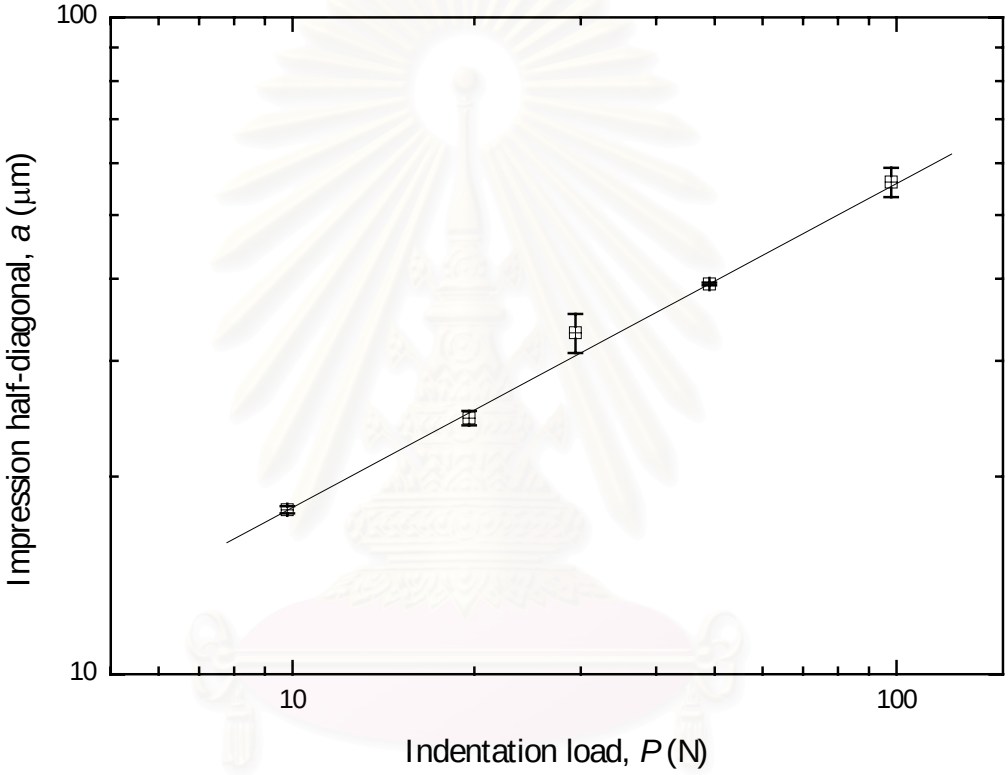

Fig. 4.8 Plot of impression half-diagonal on TZ-3YE surface as a function of indentation load.

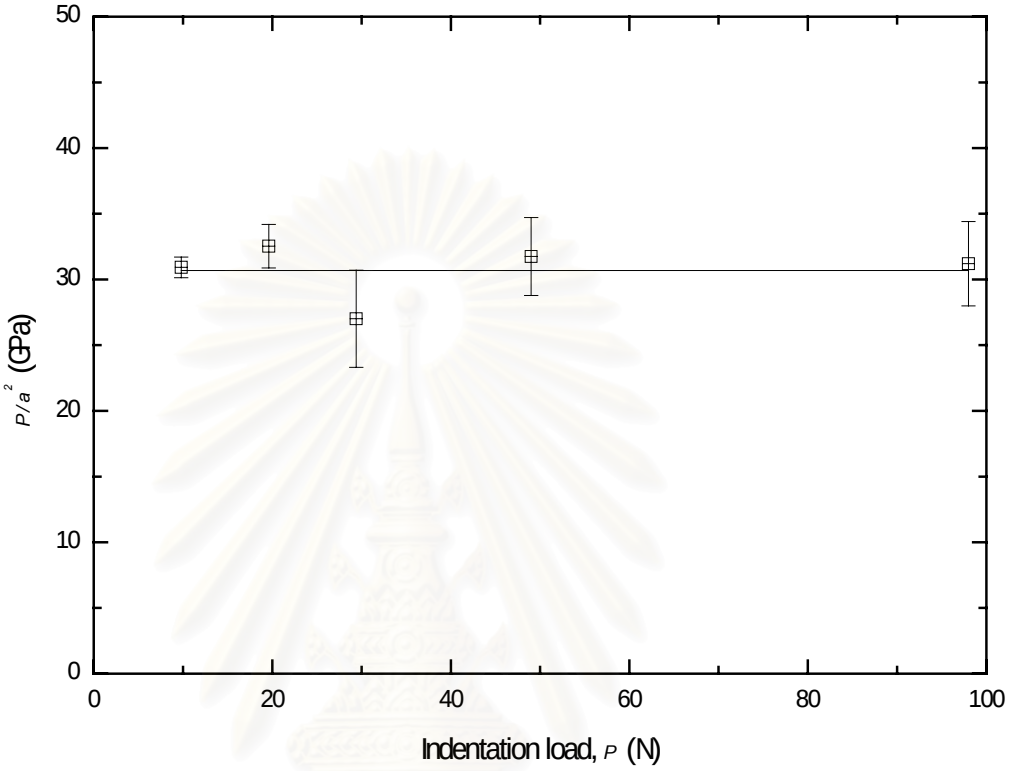

Fig. 4.9 Plot of P/a^2 as a function of indentation load of TZ-3YE specimen.

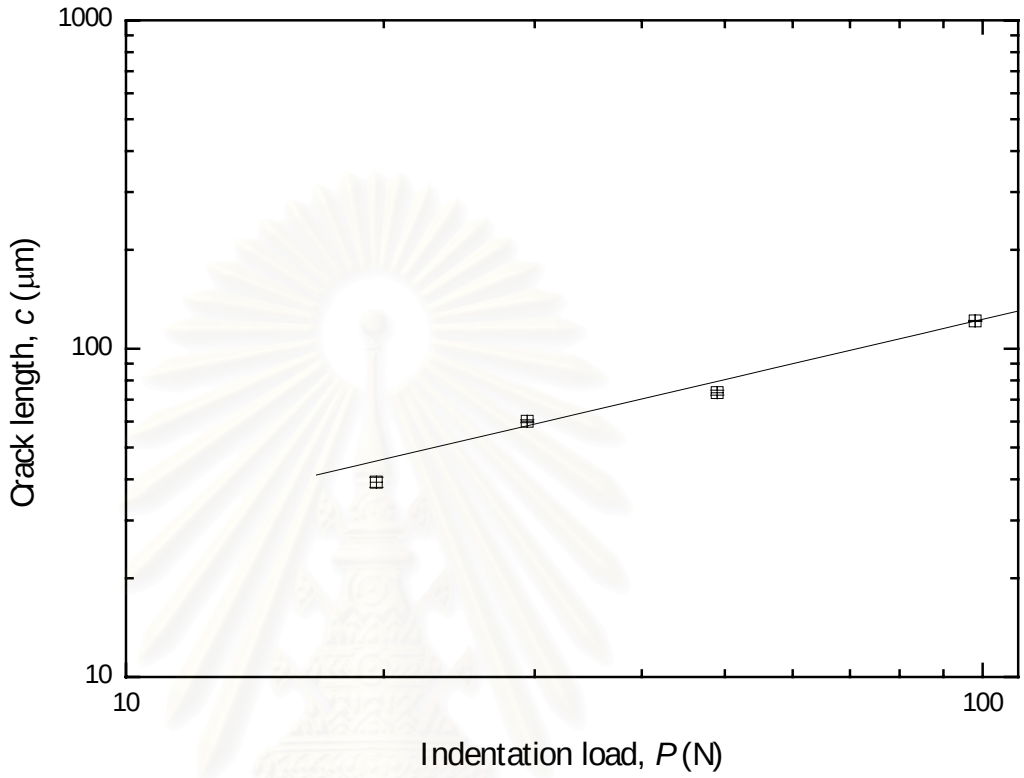

Fig. 4.10 Plot of radial crack length on TZ-3YE surface as a function of indentation load.

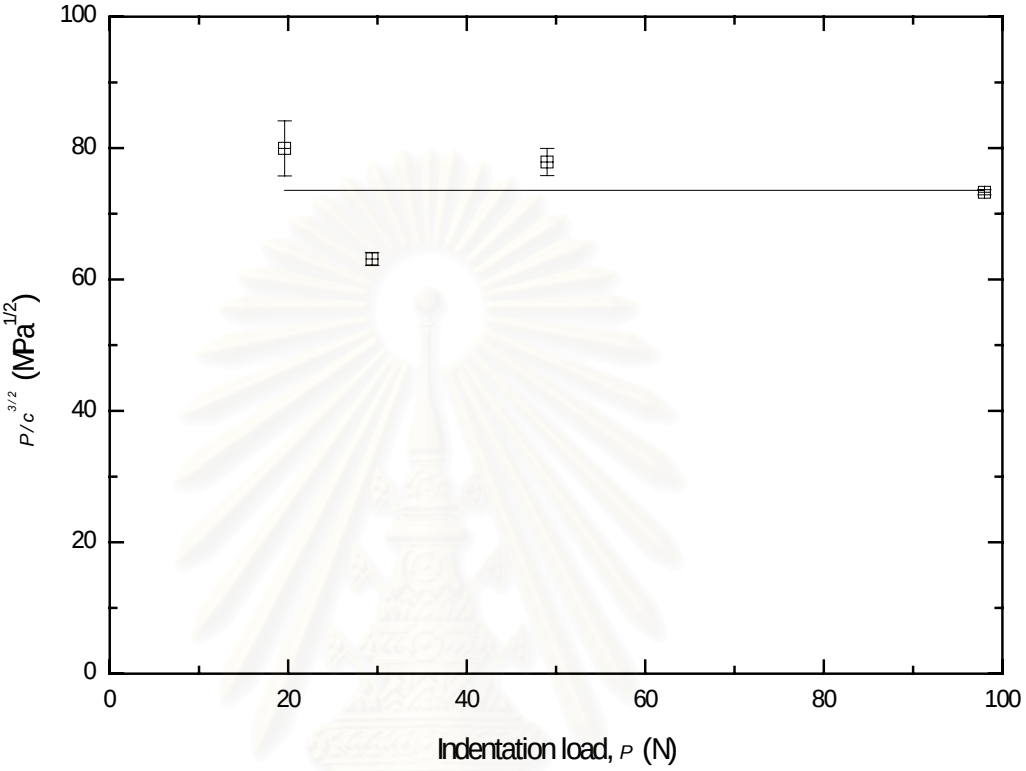

Fig. 4.11 Plot of $P/c^{3/2}$ as a function of indentation load of TZ-3YE specimen.

4.3 Response of HAp/TZ-3YE Bilayer Structure to Vickers Indentation

The indentation crack system associated with Vickers indentation of HAp/TZ-3YE bilayer for HAp layer thickness d = 800 μm in the indentation load range of 9.8 to 49 N is shown in Fig. 4.12. The surface removal due to the intersection of lateral crack with the coating surface can be seen on the bottom left quarter of the damage pattern (Fig.4.12 (c)). The surface trace of the median/radial cracks emanates from the square impression corners in a similar manner as the monolithic HAp (Fig 4.13).

Fig. 4.14 shows the Vickers-produced damage patterns on HAp/TZ-3YE bilayers for different HAp layer thicknesses at P = 29.4 N. The half-diagonal, a, of the specimen with d = 800 μm is slightly shorter than that of 600 μm thickness as shown in Fig 4.15. The impression diagonals of bilayer are inverse to the HAp layer thickness. Therefore the hardness of HAp/TZ-3YE bilayer structure depend upon the HAp layer thickness. Fig. 4.16 shows that the length of radial traces, c, of the bilayer structure is dependent on HAp layer thickness.

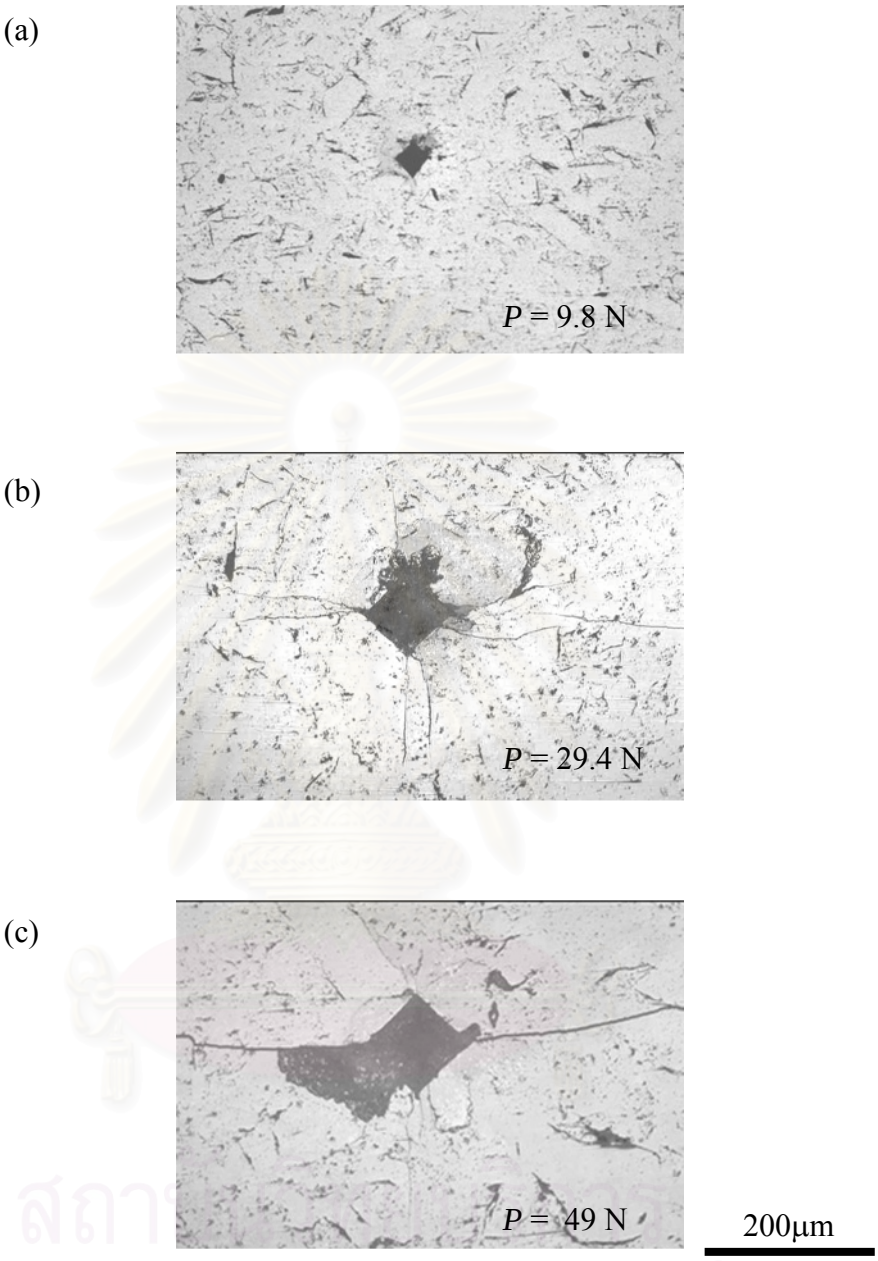

Fig. 4.12 Optical micrographs of Vickers-produced damage patterns on surface of HAp/TZ-3YE bilayer for HAp layer thickness d = 800 μm. (a) P = 9.8 N; (b) P = 29.4 N and (c) P = 49 N.

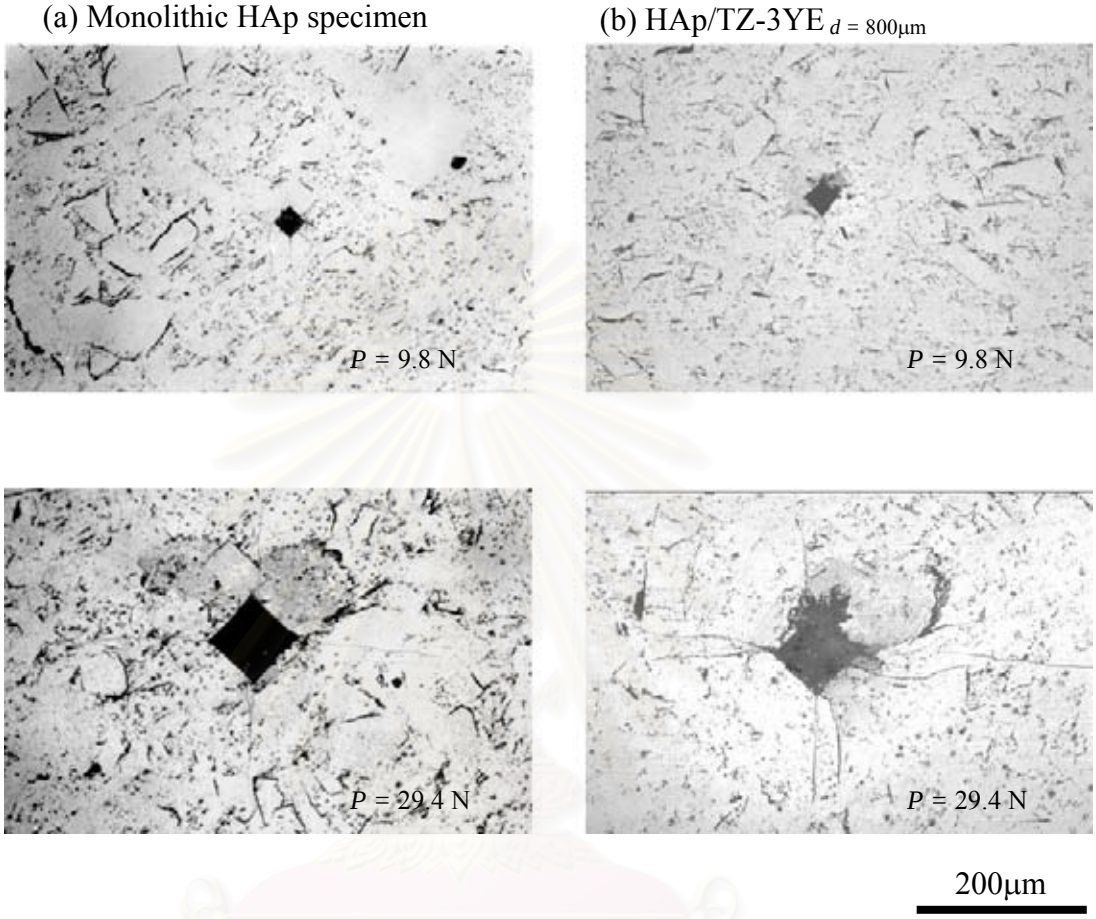

Fig. 4.13 Optical micrographs of Vickers-produced damage patterns on surfaces of monolith HAp specimen and HAp/TZ-3YE for HAp layer thickness d = 800 μm, at two different indentation loads.

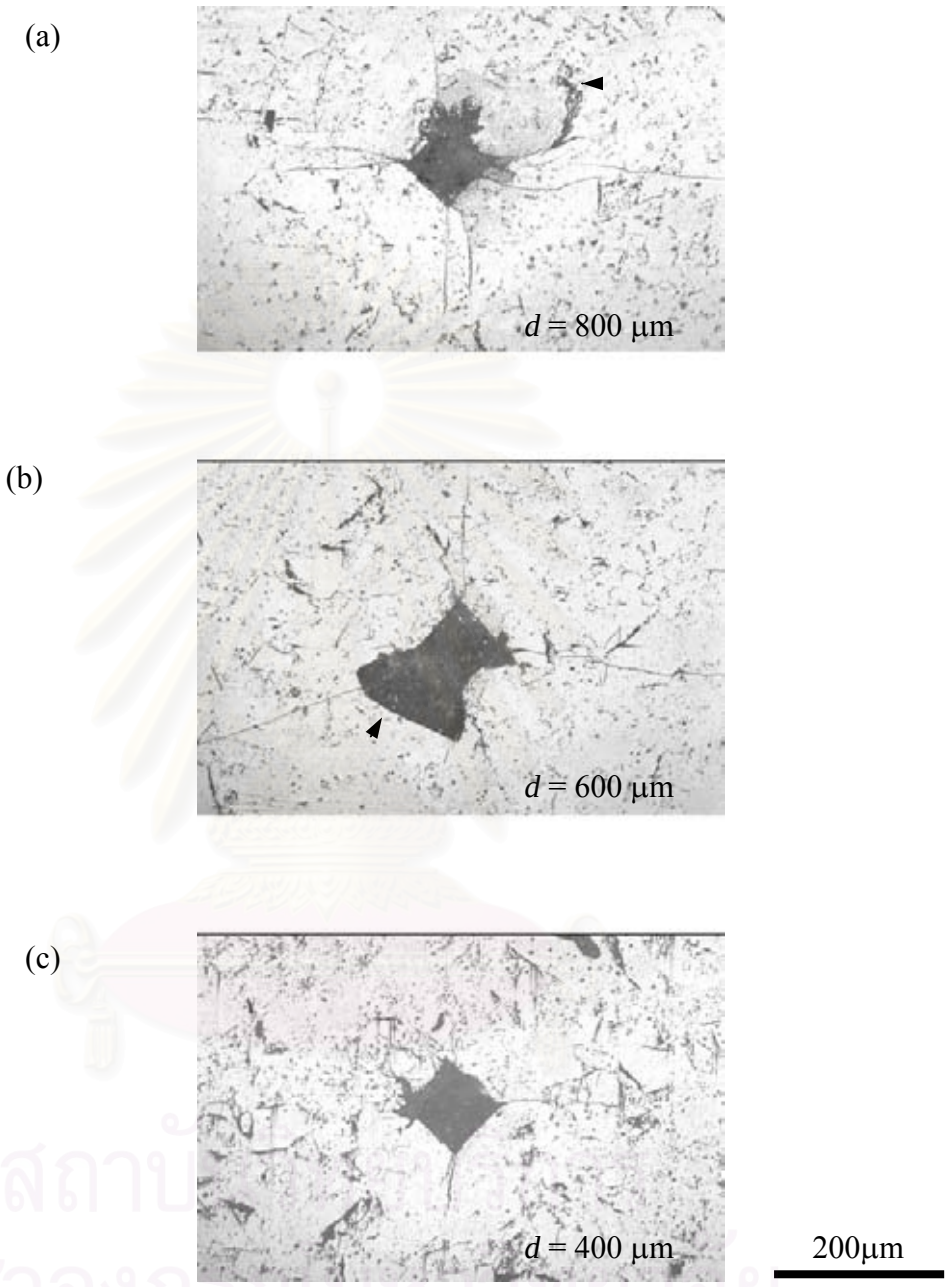

Fig. 4.14 Top coating views of Vickers contact damage in bilayer structures HAp/TZ-3YE for different HAp layer thicknesses at load 29.4 N: (a) d = 800 μm; (b) d = 600 μm; and (c) d = 400 μm.

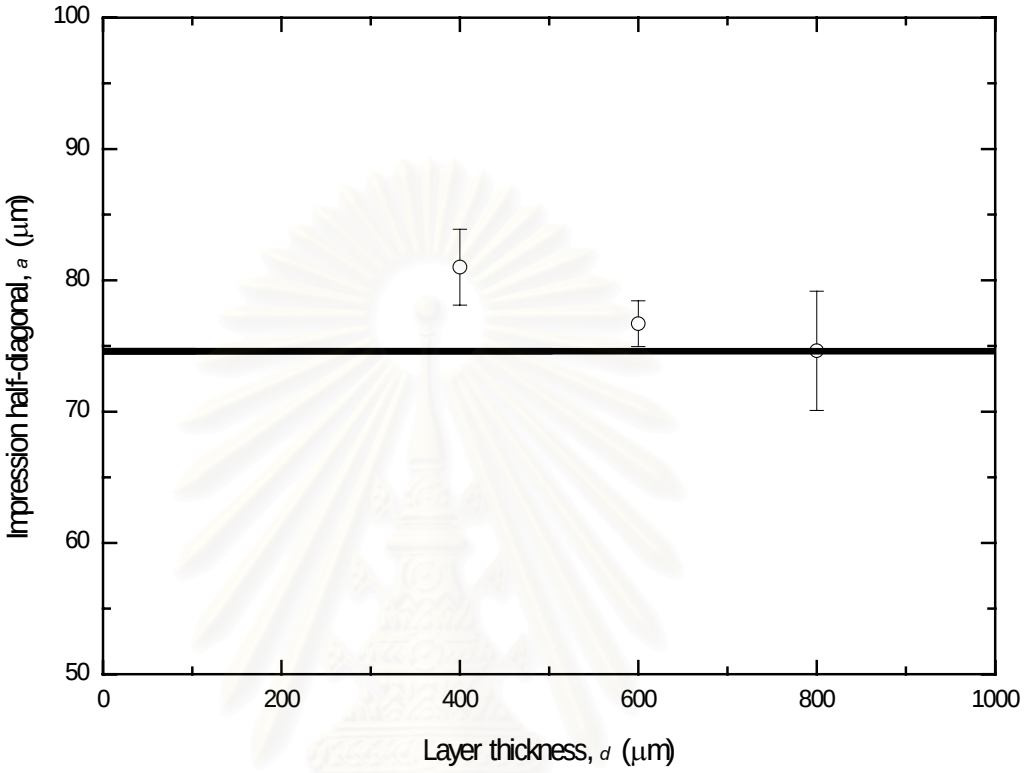

Fig. 4.15 Plot of Vickers impression half-diagonal due to 49 N as a function of HAp layer thickness. Horizontal band is the corresponding data of monolithic HAp.

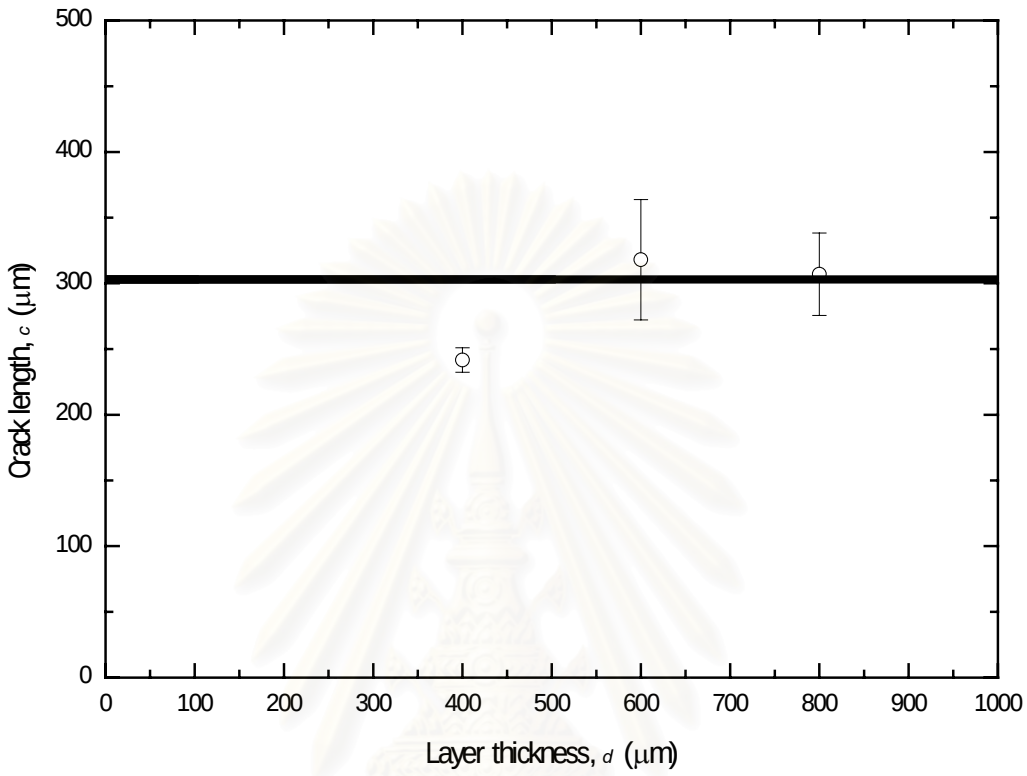

Fig. 4.16 Plot of radial crack length due to 49 N as a function of HAp layer thickness. Horizontal band is the corresponding data of monolithic HAp.

The impression half-diagonal as a function of the indentation load for HAp/TZ-3YE bilayer structure with various HAp layer thicknesses; d = 400, 600, 800 μm, is plotted in Fig. 4.17. Each data point in Fig. 4.17 shows the mean and standard deviation of three indentations. Fig. 4.17 illustrates that the dimension of impression half-diagonal on the coating HAp/TZ-3YE bilayer structures is about 1/2 power dependence of indentation load. Again, the results of impression diagonal measurements are replotted between P/a^2 and indentation load P in Fig. 4.18 for all of the three HAp layer thicknesses. The dash lines depict the mean values of P/a^2 of the bilayer with different HAp layer thicknesses. The mean values of P/a^2 are 8.65 ± 0.91, 7.99 ± 1.03, and 6.64± 0.85 GPa for the top layer thicknesses of 800, 600 and 400 μ m, respectively. Using Eq.2.1 along with the mean value of $(P/a^2)_{HAp/TZ-3YE}$ we obtain $H_{HAp/TZ-3YE}$ = 4.32 ± 0.36, 3.99 ± 0.51 and 3.32 ± 0.42 GPa for HAp layer thicknesses of 800, 600 and 400 μm, respectively.

The radial crack length as a function of indentation load in the range of 9.8 to 49 N for HAp/TZ-3YE bilayer structure with various thicknesses is shown in Fig. 4.19. Each data point in Fig. 4.19 represents the mean and standard deviation of three indentations. The dash lines are the best fits to the c-P data. The slope of the three dash lines are 2/3, which has established that the dimension of the radial crack on the coating surface still follows Eq. 2.2 ($P\alpha\ c^{3/2}$). Fig. 4.20 resummarizes the result of crack measurements as $P/c^{3/2}$ as a function of indentation load, P. It denotes that $P/c^{3/2}{}_{HAp/TZ-3YE}$ of 800, 600, and 400 μm thicknesses of the HAp layers are 9.04 ± 0.65, 8.83 ± 0.32 and 11.80 ± 1.89 $MPam^{1/2}$, respectively. The fracture toughness of HAp/TZ-3YE bilayer structures are 0.57 ± 0.04, 0.58 ± 0.02 and 0.85 ± 0.13 $MPam^{1/2}$ for thicknesses of 800, 600 and 400 μm of the HAp layer, respectively.

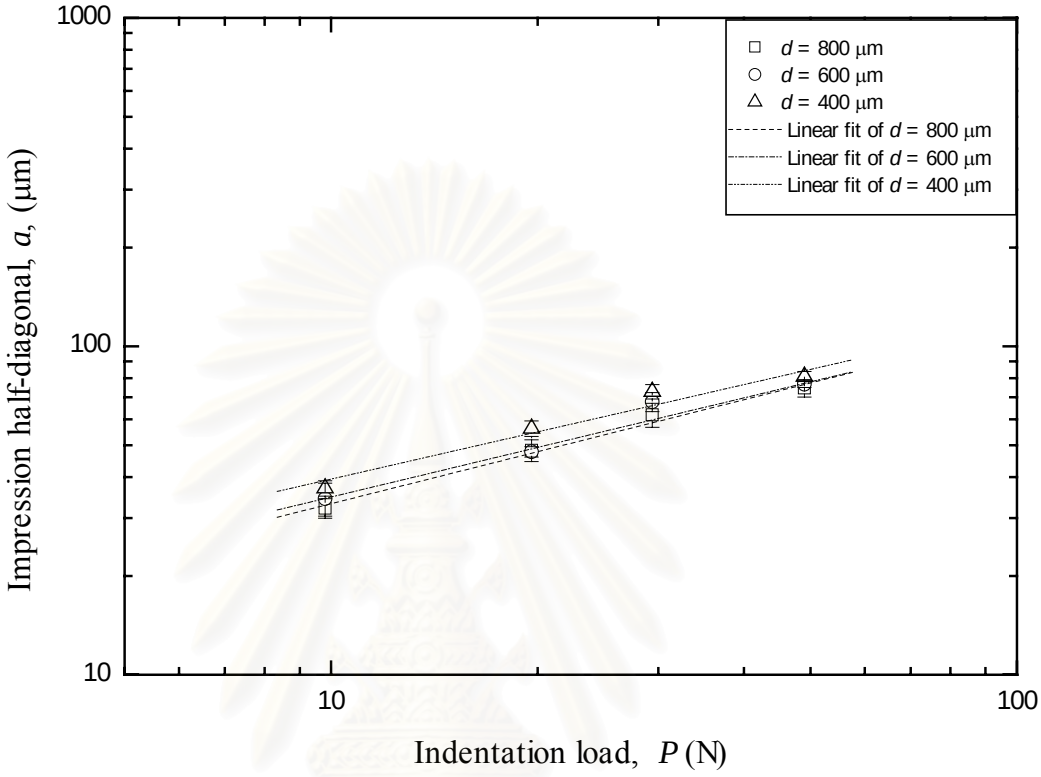

Fig. 4.17 Plot of impression half-diagonal on HAp/TZ-3YE coating surface as a function of indentation load, for different thicknesses of HAp layer.

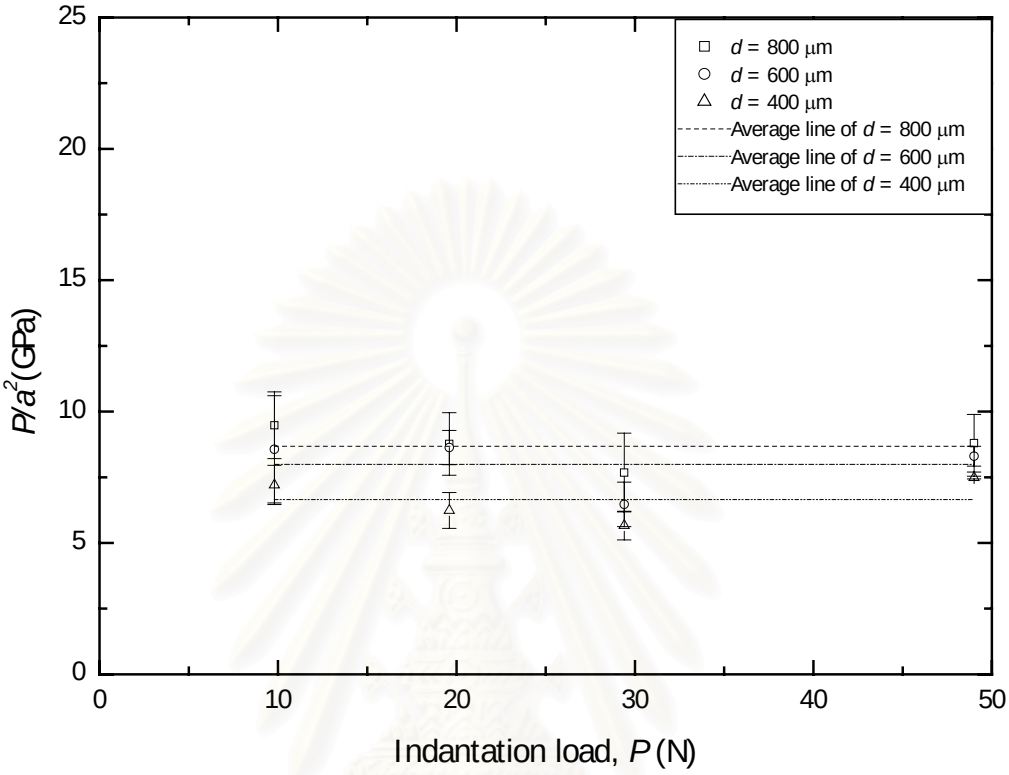

Fig. 4.18 Plot of P/a^2 as a function of indentation load of HAp/TZ-3YE coating surface.

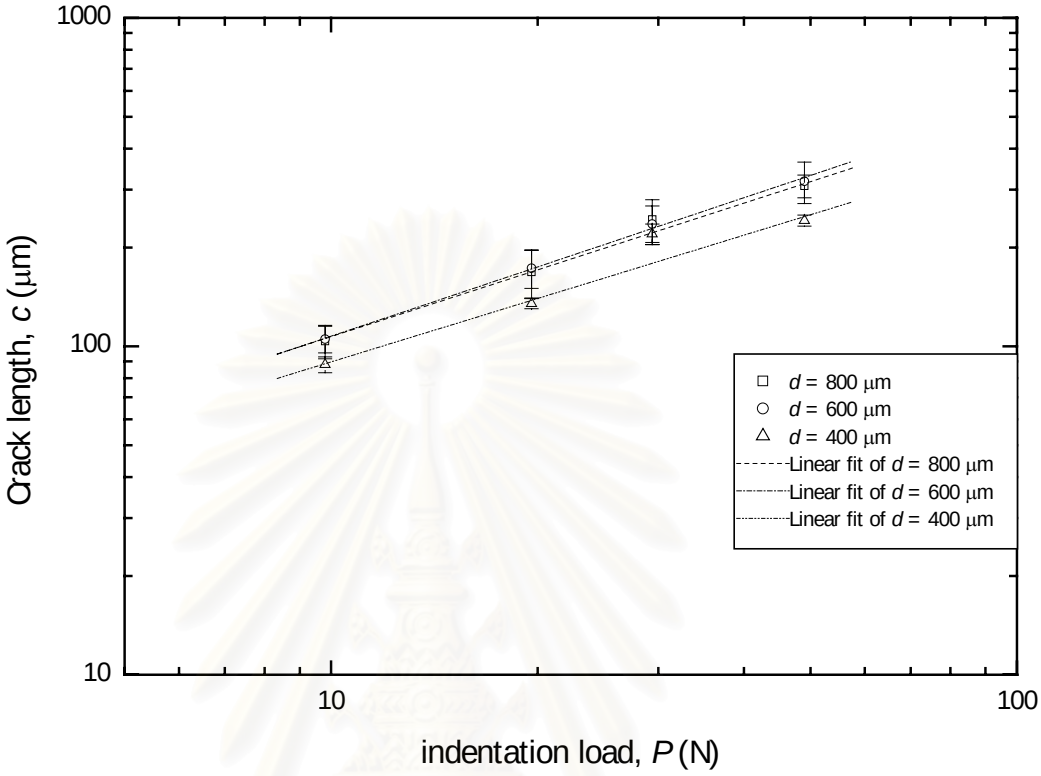

Fig. 4.19 Plot of radial crack length on HAp/TZ-3YE coating surface as a function of indentation load.

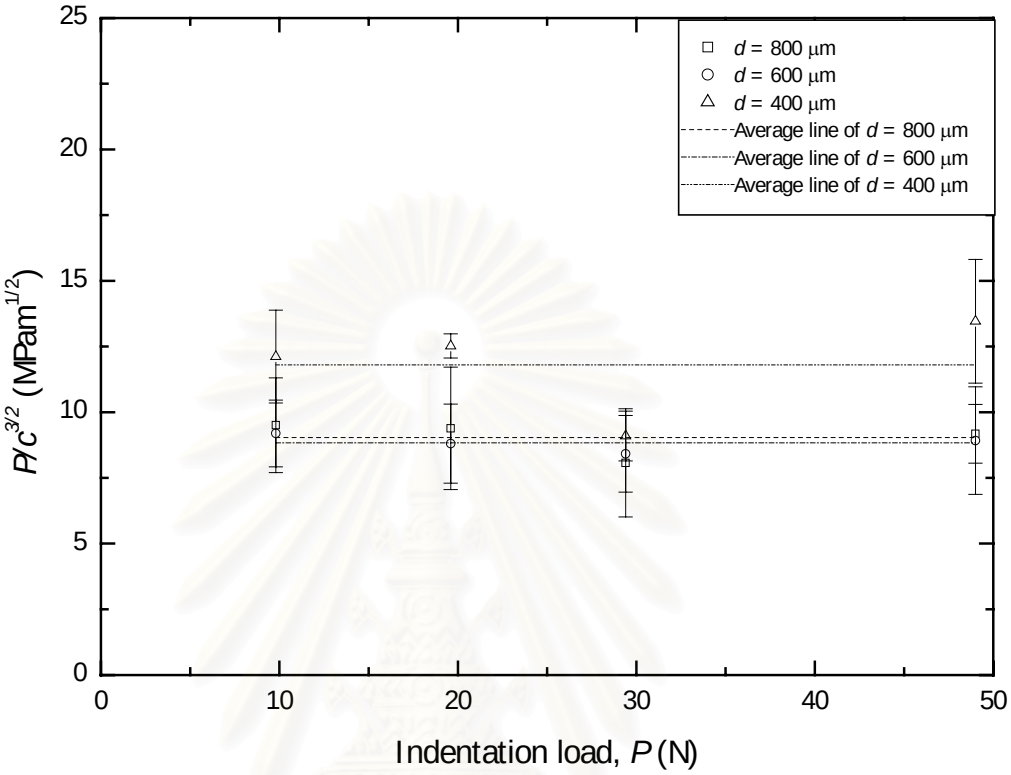

Fig. 4.20 Plot of $P/c^{3/2}$ as a function of indentation load for different HAp layer thicknesses of HAp/TZ-3YE bilayer.

4.4 Response of HAp/TZ-3YE Bilayer Structure to Hertzian Indentation

The Hertzian indentation fracture due to a hard tungsten carbide (WC) sphere, are observed by using bonded-interface technique. Fig 4.21 shows Hertzian indentation damage in HAp/TZ-3YE bilayer with the HAp layer thickness of 600 μm, using WC sphere of the radius of 3.96 mm at P = 70 N. It can be seen that ring crack occurs on the top surface and the cone crack occur in subsurface.

Fig. 4.22 shows the effect of indentation load on Hertzian contact damage on HAp/TZ-3YE bilayer, with HAp layer thickness of 600 μm, from bonded-interface specimens. The indentation loads, P, are 50, 70 and 100 N. In this bilayer system, the adhesive bonding is strong enough to preclude delamination. Micrographs show cone crack fractures in the coating layer without any crack in the substrate. The cone crack initiated on the top coating surface at P = 50 N extends downward into the coating layer (Fig. 4.22 (a)). The cone cracks develop at P = 70 N (Fig. 4.22 (b)) and P = 100 N (Fig. 4.22 (c)) do not appear to extend much further in depth than the cone crack due to P = 50 N. Consequently the primary effect of increased loading is to increase the density rather than the depth of cone cracks.

The sequence of micrographs of Hertzian contact damage in HAp/TZ-3YE bilayers at fixed indentation load P = 100 N in Fig. 4.23 illustrates the effect of HAp layer thickness on the damage pattern. For HAp layers of 600 and 800 μm thicknesses, only cone crack is generated in the HAp layer (Fig 4.23 (a) and (b)).

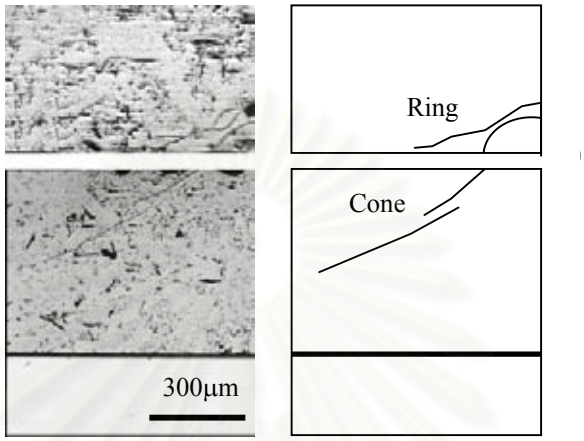

Fig. 4.21 Contact fracture in HAp/TZ-3YE bilayer, for HAp layer of thickness of 600 μm, using WC sphere with radius of 3.96 mm at P = 70 N. Optical micrographs are on the left hand side whereas the corresponding schematic diagrams are on the right hand side.

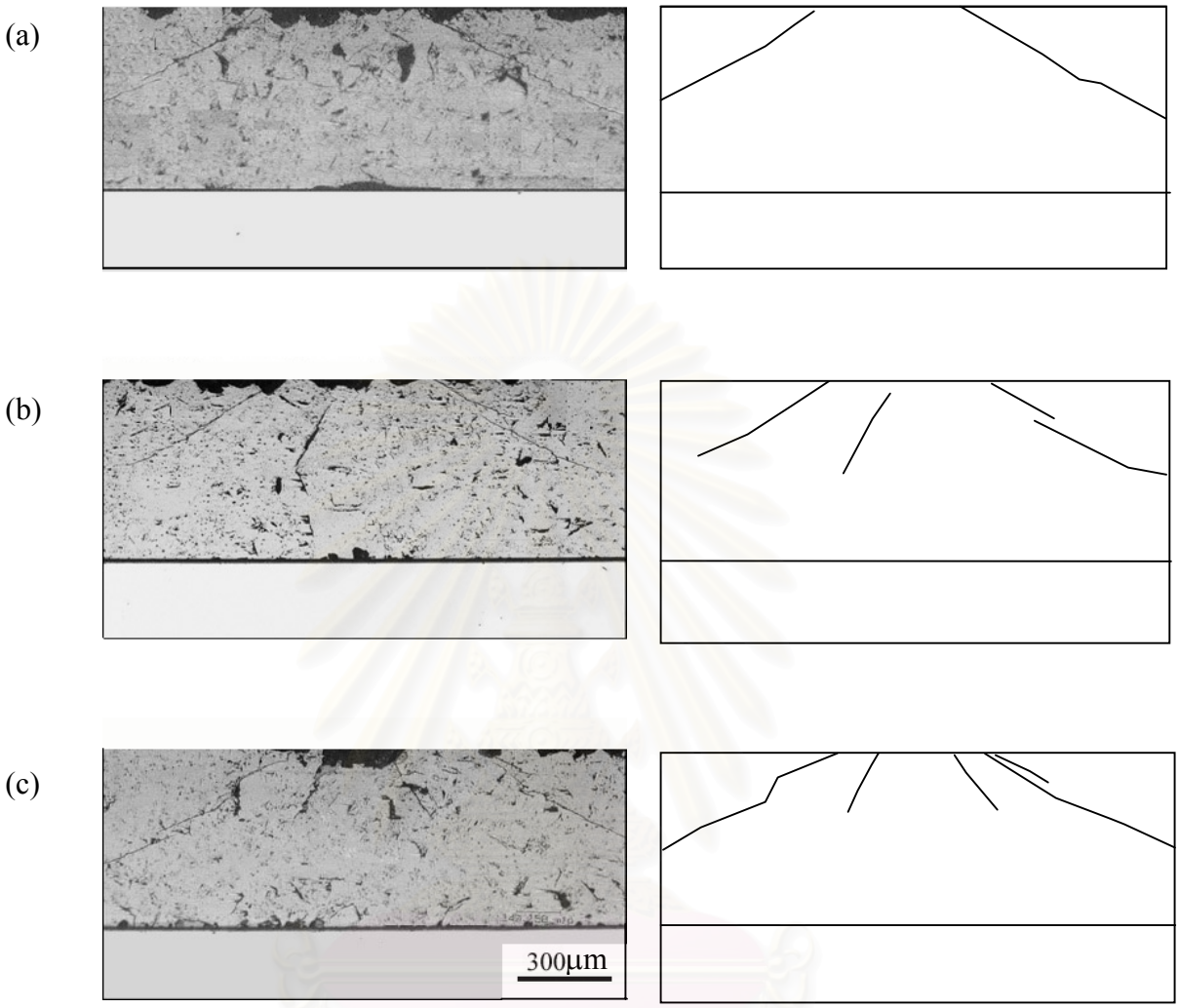

Fig. 4.22 Contact fracture in HAp/TZ-3YE bilayer with HAp layer thickness of 600 μm due to, using WC sphere r = 3.96 mm, demonstrating the effect of indentation load: (a) P = 50 N; (b) P = 70 N; and (c) P = 100 N. Optical micrographs are on the left hand side whereas the corresponding schematic diagrams are on the right hand side. Note the formation of cone cracks in top layer increase in density, but not depth of cone cracks, with increasing load.

Fig. 4.23 Contact fracture in HAp/TZ-3YE bilayer, due to WC sphere r = 3.96 mm at P = 100 N, demonstrating the effect of HAp layer thickness: (a) d = 800 μm; (b) d = 600μm; and (c) d = 400 μm. Optical micrographs are on the left hand side whereas the corresponding schematic diagrams are on the right hand side.

However the density of cone crack increases as the HAp layer thickness decreases. For HAp theckness of 400 μm, the inner crack which initiate from the coating/substrate interface under contact area extend vertically upward toward the HAp surface.

4.5 Discussion and Conclusion

Examinations of damage patterns produced by Vickers indenter on HAp/TZ-3YE surfaces (Figs. 4.12 and 4.14) indicate that the Vickers indentation pattern consist of a square impression and two crack systems, i.e. the median/radial crack and lateral crack, as those on the monolithic HAp surfaces (Figs. 4.1 and 4.2). It is noted that the impression diagonals of HAp/TZ-3YE bilayer with the HAp thicknesses of 800 and 600 μm are close to monolithic HAp (Fig. 4.15). Furthermore the lengths of the median/radial crack traces are closed to those in the monolithic HAp (Fig. 4.16). The data obtained by directly measuring the impression diagonals and the median/radial crack lengths from the damage patterns due to Vickers indentation as function of indentation load (Figs. 4.15 – 4.20) indicated that the value of hardness and fracture toughness of the bilayer with the HAp layer of thickness of 800 μm and that of the monolithic HAp are not much different. These results imply that the mechanical properties of the bilayer with the HAp layer thicknesses of 800 and 600 μ m are similar to the HAp monolith. Whereas the HAp layer thickness of 400 μm are different form HAp monolith.

The results of Hertzian indentation on the HAp/TZ-3YE bilayer indicates that only cone cracks are in the HAp layer of thicknesses of 800 and 600μm. The primary

effect of increased loading is to increase the density rather than the depth of cone cracks (Fig. 4.22). In the thinnest coating; d = 400 μm, both cone crack and inner crack are observed at P = 100 N (Fig. 4.23). There are two factors that result in the initiation of factor the inner crack. The first factor is the properties of specimen and the second factor is the ratio between the adhesive thickness and coating thickness [56]. The Young's modulus of adhesive layer (about 2 MPa) is much less than that of the HAp layer (67 GPa). Therefore this system might be flexed in the bottom of coating layer, which cause the generation of the inner crack. In addition, the critical load inducing the inner crack is inversely proportional to the ratio of adhesive and coating thicknesses. Therefore, indentation loads ($10 \leq P \leq 100$ N) might be not enough to generate the inner crack in the HAp layers of thicknesses of 800 and 600 μm.

For the thin HAp layer (d= 400 μm), the response of cracks are different. This might be influenced by the presence of the intermediate layer (adhesive polymer) or the substrate (TZ-3YE). However, there are not enough evidences to draw a conclusion. In order to gain decisive conclusion on these responses, it will be needed to apply finite element computation to the process of stress analysis.

4.6 Suggestion for Further Work

In the processing of HAp/TZ-3Y (or HAp/TZ-3YE) bilayer structure, it is important to improve many factors, which can eliminate the flaws occurred in the HAp layer. These factors include the reduction of the thermal expansion coefficient mismatch and different shrinkage between the two layers during sintering schedule. The improvement in the processing of HAp/TZ-3YE may be done as following:

1. Include whiskers or chopped fibers in the powders in order to increase strengthen in HAp layer during the sintering period.

2. Modify sintering rate by adding second phases or different particle sizes.

3. Get better particle packing and smaller shrinkage by tape casting processing.

To understand and enable the prediction of the mechanical response of HAp/TZ-3YE bilayer (with adhesive polymer), finite element analysis should be used to map out detailed contact stress fields from indentation contact on bilayer structure.

REFERENCES

1. L.L. Hench. Bioceramics: from Concept to Clinic. J.Am.Ceram.Soc. 74 (1991) 1487-510.
2. J.B. Park. Biomaterials Science and Engineering. New York : Plenum Press, 1987.
3. L.L. Hench and E.C. Ethridge. Biometerials. New York : Academic Press, 1982.
4. E.A. Monroe, W. Votava, D.B. Bass and J. McMullen. New Calcium Phosphate Ceramic Material for Bone and Tooth Implants. J.Dental.Res. 50 (1971) : 860-861.
5. L.L. Hench, R.J. Splinter, W.C. Allen, T.K. Greenlee Jr. Bonding Mechanisms at the Interface Ceramic Prosthetic Materials. J.Biomed. Mater. Res.Symp. 2 (1972) : 117-41.
6. W. Suchanek, and M. Yoshimura. Processing and Properties of Hydroxyapatite-based Biomaterials for Use as Hard Tissue Replacement Implants. J.Mater.Res. 13 (1998) : 94-116.
7. H. Aoki. Scince and Medical Applications of Hydroxyapatite. Tokyo : JAAS, (1991).
8. S. Best, W. Bonfield and C. Doyle, Bioceramics. Proceedings of the 2 ed International Symposium on Ceramics in Medicine. 2 (1990) : 57.
9. W. Suchanek, M. Yashima, M. Kakihana, and M. Yoshimura. Hydroxyapatite/Hydroxyapatite-Whisker Composites without Sintering Additives: Mechanical Properties and Microstructural Evolution. J.Am.Ceram.Soc. 80(1997) : 2805-13.

10. A. Nakahira, K. Sakamoto, S. Yamaguchi, M. Kaneno, S. Takeda, M. Okazaki. Novel Synthesis Method of Hydroxyapatite Whiskers by Hydrolysis of α-Tricalcium Phosphate in Mixtures of Water and Organic Sovent. J.Am.Ceram.Soc. 82 (1999) : 2029-32.

11. A.J. Ruys, B.K. Milthorpe, and C.C. Sorrell. Short-Fibre-reinforced Hydroxyapatite: Effects of Processing on Thermal Stability. J.Aust.Ceram.Soc. 29 (1993) : 39-49.

12. K. Ioku, S. Somiya, and M. Yoshimura. Hydroxyapatite Ceramics with Tetragonal Zirconia Particle Dispersion Prepared by HIP Post-sintering. J.Ceram.Soc.Jpn.Int.Ed. 99 (1991) : 191-98.

13. E. Adolfsson, P. Alberius-Henning, and L. Hermansson. Phase Analysis and Thermal Stability of Hot Isostatically Pressed Zirconia-Hydroxyapatite Composites. J.Am.Ceram.Soc. 83 (2000) : 2798-802.

14. A. Pajares, L.Wei, B.R. Lawn, N.P. Padture and C.C. Berndt. Mechanical Characterization of Plasma-Spayed Ceramic Coatings on Metal Substrates. Mater.Sci.Eng. A208 (1996) : 158-165.

15. J. Weng, X. Liu, X. Zhang, K. and de Groot. Integrity and thermal decomposition of apatite in coatings influenced by underlying titanium during plasma spraying and post-heat-treatment. J.Biomed.Mater.Res. 30 (1996) : 5-11.

16. L. Fu, K.A. Khor, J.P. Lim. Yttria stabilized zirconia reinforced Hydroxyapatite Coatings. Surf.Coat.Tech. 127 (2000) : 66-75.

17. B. Ben-Nissan, and C. Chai. Advavances in Materials Science and Implant Orthopedic Surgery. NATO ASI Series E294. Dordrecht : Kluwer Academic Publishers (1995).

18. K. Hwang, J. Song, B. Kang, Y. Park. Sol-Gel Derived Hydroxyapatite Films on Alumina Substrates Surf.Coat.Tech. 123 (2000) : 252-255.

19. Y. Ohba, T Watanabe, E. Sakai, and M. Daimon. Coating of HAp/$CaTiO_3$ on Titanium Substrates by Hydrothermal Method, J.Ceram.Soc.Jpn.Int.Ed. 107 (1999) : 907-12.

20. K. de Groot. Mater.Technol. 8(1993) : 12. Cite in W. Suchanek, and M. Yoshimura. Processing and Properties of Hydroxyapatite-based Biomaterials for Use as Hard Tissue Replacement Implants. J.Mater.Res. 13 (1998) : 94-116.

21. Y-M. Kong, S. Kim, and H-E. Kim. Reinforcement of Hydroxyapatite Bioceramic by Addition of ZrO_2 Coated with Al_2O_3. J.Am.Ceram.Soc. 82 (1999) : 2963-68.

22. H. Wang and X. Hu. Surface Properties of Ceramic Laminates Fabricated by Die pressing. J.Am.Ceram.Soc. 79 (1996) : 553-56.

23. H. Liu, B.R. Lawn, and S.M. Hsu. Hertzian Contact Response of Tailored Silicon Nitride Multilayers. J.Am.Ceram.Soc. 79 (1996) : 1009-14.

24. J.R. Mawdsley, D. Kover, and J.W. Halloran. Fracture Behavior of Alumina/Monazite Mulilayer Laminates. J.Am.Ceram.Soc. 83 (2000) : 802-08.

25. C.J. Russo, M.P. Harmer, H.M. Chan, and G.A. Miller. Mechanical Properties of Laminated Ceramic Composites in Alumina- and Zirconia- Based Systems. Ceram.Eng.Sci.Proc. 14 (1993) : 988-1005.

26. A.V. Virkar, J.L. Huang, and R.A. Cutler. Strengthening of Oxcide Ceramics by Transformation-Induced Stress. J.Am.Ceram.Soc. 70 (1987) : 164-70.

27. A.V. Virkar, J.F. Jue, J.J. Hansen and R.A. Cutler. Measurement of residual stresses in Oxide-ZrO_2 Three-layer Composites. J.Am.Ceram.Soc. 71 (1988) : C-148-151.

28. H. Wang, and X. Hu. Surface Properties of Ceramic Laminates Frabricated by Die Pressing. J.Am.Ceram.Soc. 79 (1996) : 553-56.

29. A.J. Phillipps, W.J. Clegg, and T.W. Clyne. Fracture Behavior of Ceramic Laminates in Bending-I. Modelling of Crack Propagation. Acta Metall.Mater. 41 (1993) : 805-17.

30. W.J. Clegg and L.R. Seddon. The Failure of Tough Ceramic Laminates. Euro.Mat.91, Anvances in Structural material. 2 (1991) : 266-69.

31. W.J. Clegg. The Frabrication and Failure of Laminatar Ceramic Composites. Acta Metall.Mater. 40 (1992) : 3085-93.

32. J.R. Mawdsley, Desiderio Kovar and J.W. Halloran. Fracture Behavior of Alumina/Monazite Multilayer Laminates. J.Am.Ceram. 83 (2000) : 802-808.

33. C.J. Russo, M.P. Hammer, H.M. Chan and G.A. Miller, Design of a Laminated Ceramic Composite for Improved Strength and Toughness. J.Am.Ceram.Soc. 75 (1992) : 3396-3400.

34. C.J. Russo, M.P. Hammer, H.M. Chan and G.A. Miller, Mechanical Properties of LaminatedCeramic Composites in Alumina-and Zirconia-Based Systems. Ceram.Eng.Sci.Proc. 14 (1993) : 998-1005.

35. S. Wuttiphan, B.R. Lawn and N.P. Padture, Crack Suppression in Strongly-Bonded Homogenous/Heterogenous Laminates : A Study on Glass/Glass-Ceramic Bilayers. J.Am.Ceram.Soc. 79 (1996) : 634-40.

36. K.S. Lee, S. Wuttiphan, X.Z. Hu, S.K. Lee, and B.R. Lawn, Contact-Induced Transverse Fractures in Brittle Layers on Solft Substrates : A Study on Silicon Nitride Bilayers. J.Am.Ceram.Soc. 81 (1998) : 571-80.

37. H. Chai, B.R. Lawn, Role of Adhesive Interlayer in Transverse Fracture of Brittle Layer Structures. J.Mater.Res. 15 (2000) : 1017-24.

38. L. An, H.M. Chan, N.P. Padture and B.R. Lawn, Damage-Resistant Alumina-Based Layer Composites. J.Mater.Res. 11 (1996) : 204-10.

39. A.G. Evans. Strength Degradation by Projectile Impacts. J.Am.Ceram.Soc. 56 (1973) : 405.

40. R.M. Gruver and H.P. Kirchner. Effect of Surface Damage on the Strength of Al_2O_3 Ceramics with Compressive Surface Stresses. J.Am.Ceram.Soc. 56 (1973) : 21.

41. R.M. Gruver and H.P. Kirchner. Effect of Environment on Penetration of Surface Damage and Remaining Strength of Al_2O_3. J.Am.Ceram.Soc. 57 (1974) : 57.

42. B.R. Lawn, and T.W. Wilshaw. Review Indentation Fracture : Principles and Applications. J.Mater.Sci. 10 (1975) : 1049-81.

43. B.R. Lawn, A.G. Even, and D.B. Marshall. Elastic/plastic Indentation Damage in Ceramics: The Median/Radial Crack System. J.Am.Ceram.Soc. 63 (1980) : 574-81.

44. B.R. Lawn, and D.B. Marshall. Hardness, Toughness, and Brittleness: An Indentation Analysis. J.Am.Ceram.Soc. 62 (1979) : 347-50.

45. B.R. Lawn, and T.W. Wilshaw. Fracture of Brittle Solids. London : Cambridge University (1975).

46. B.R. Lawn. Fracture of Brittle Solids. (2nd ed.). Cambridge Solid State Scince Series. Great Britain : Cambridge University (1993).

47. G.R. Antis, P. Chantikul, B.R. Lawn and D.B. Marshall. A critical Evaluation of Indentation Techniques for Measuring Fracture Toughness: I, Direct Crack Measurements. J.Am.Ceram.Soc. 81 (1981) : 533-38.

48. B.R. Lawn, and D.B. Marshall. Indentation Fracture and Strength Degradation in ceramics. In R.C. Bradt, D.P.H. Hasselman, and F.F. Lange. Fracture Mechanics of Ceramics, Vol.3. pp.205-227. (n.p.) : Plenum Publishing Corporation, 1978.

49. B.R. Lawn. Indentation of Ceramics with Spheres: A Century after Hertz. J.Am.Ceram.Soc. 81 (1998) : 1977-94.

50. H.Hertz. Hertz's Miscellaneous Papers. Chs.5,6. (London) : Macmillan, 1896.

51. B.R. Lawn, T.W. Wilshaw, and N.E.W. Hartley. Int.J.Fract. 10 (1974) : 1-16.

52. F.C. Roesler. Brittle Fractures Near Equilibeium. Proc.Phys.Soc.London. B69 (1956) : 981-92.

53. K.S. Lee, S.K. Lee and B.R. Lawn. Contact Damage and Strength Degradation in Brittle/Quasi-Plastic Sillicon Nitride Bilayers. J.Am.Ceram.Soc.. 81 (1998) : 294-404.

54. K.S. Lee, S. Wuttiphan, X.Z. Hu, S.K. Lee and B.R. Lawn. Contact-Induced Transverse Fractures in brittle Layers on Solft Substrates: A Study on Silicon Nitride Bilayers. J.Am.Ceram.Soc. 81 (1998) : 571-80.

55. H. Chai, B.R. Lawn and S. Wuttiphan. Fracture Mode in Brittle Coating with Large Interlayer Modulus Mismatch. J.Mater.Res. 14 (1999) : 3805-17.

56. H. Chai and B.R. Lawn. Role of Adhesive Interlayer in Transverse Fracture of Brittle Layer Structures. J.Mater.Res. 15 (2000) : 1017-24.

57. Y-W. Rhee, H-W. Kim, Y. Deng and B.R. Lawn. Contact-Induced Damage in Ceramic Coatings on Compliant Substrates: Fracture Mechanics and Design. J.Am.Ceram.Soc. 84 (2001) : 1066-72.

58. B.R. Lawn, K.S. Lee, H. Chai, A. Pajares, D.K. Kim, S. wuttiphan, I.M. Peterson and X. Hu. Damage-Resistant Brittle Coating. Advanced Engineering Materials. 2 (2000) : 745-48.

59. F. Guiberteau, N.P. Padture, and B.R. Lawn. Effect of grain Size on Hertzian Contact Damage in Alumina. J.Am.Ceram.Soc. 77 (1994) : 1825-31.

60. B.R. Lawn, S.K. Lee, I.M. Pterson, and S. Wuttiphan. Model of Strength Degradation from Hertzian Contact Damage in Tough Ceramics. J.Am.Ceram.Soc. 81 (1998) : 1509-20.

61. H. Cai, M.A. Stevens Kalceff, and B.R. Lawn. Deformation and Fracture of mica-ceramics in Hertzian Contacts. J.Mater.Res. 9 (1994) : 762-70.

62. L. An, H.M. Chan, N.P. Padture, and B.R. Lawn. Damage-Resistant Alumina-Based Layer Composites.Effect of grain Size on Hertzian Contact Damage in Alumina. J.Mater.Res. 11 (1996) : 204-10.

63. S. Wuttiphan, B.R. Lawn, and N.P. Padture. Crack Suppression in Strongly Boned Homogenous/Heterogenous Laminates: A Study on Glass/Glass-Ceramic Bilayers. J.Am.Ceram.Soc. 79 (1996) : 634-40.

64. L. Wei and B.R. Lawn. Thermal Wave Analysis of Contact Damage in Ceramics: Case Study on Alumina. J.Mater.Res. 11 (1996) : 939-47.

65. M. Jarcho, C.H. Bolen, M.B. Thomas, J. Bobick, J.F. Kay, and R.H. Doremus. Hydroxyapatite Synthesis and Characterization in Dense Polycrystalline Form. J.Mat.Sci. 11 (1976) : 2027-35.

66. H. Tagai, and H. Aoki, Bioceramics Symposium, Keele, Sep. 16, (1978).

67. R.Z. Kegeros, W.P. Shirra, M. Miravite, and J.P.Legeros, ColloquesInternationaux du CNRS. Physico-Chimie et Cristallographie des Apatites d'-Interet Biologique. Paris : CNRS, (1975).

68. G. Bonel, Contribution à Í étude de la Carbonation des apatites. I. Synthése et é tude des propriétés physico-chimiques des apatites carbonatées de type A. Ann.Chim.(Paris) 7 (1972) : 65-88 .

69. KANAZAWA, Takafumi. Inorganic Phosphate Materials. Materials Science Monographs 52. Tokyo : Kodansha Ltd., (1989).

70. R.A. Young, ColloquesInternationaux du CNRS. Physico-Chimie et Cristallographie des Apatites d'-Interet Biologique. Paris : CNRS, (1975).

71. H. Monma, S. Ueno, and T. Kanasawa, Properties of Hydroxyapatite Prepared by the Hydrolysis of Tricalcium Phosphate. J.Chem.Technol.Biotechnol. 31 (1981) : 15-24.

72. S. Wuttipan. Strength and Microstructure of Hydroxyapatite Ceramics M.Sc. Thesis. Physics Science Chulalongkorn University, (1993).

73. P.A. Christel,T. Klein, P. Patka, H.B.M. Vander Lubbe, J.G.C. Wolke, and K.de.Groot. Plasma-Spayed Coatings of Tetracalciumphosphate, Hydroxyl-apatite, and α- TCP on Titnium Alloy: An Interface Study. J.Biomed.Mater.Res 25 (1991) : 53.

74. W.H. Gitzen. Alumian as A Ceramic Material. USA : The American Ceramic Society (1980).

75. K. de Groot, T. Yamamuro, L.L. Hench and J. Wilson. Handbook of Bioactive Ceramic 2. (np.) : CRC (1990).

76. R.A. Miller, R.G. Smialek and Garlick. Science and Technology of Zirconia. Advance Ceramic. 3 (1981) : 241.

77. R.C. Garive, R.H.J. Hannink, and R. T. Pascoe. Ceramic Steel?. Nature. 258 (1975) : 703-704.

78. R.H.J. Hannink, P.M. Kelly, and B.C. Muddle. Transform Toughening in Zirconia-Containing Ceramics. J.Am.Ceram.Soc. 83 (2000) : 461-87.

79. M.A. Meyers and K.K. Chawla. Mechanical Behavior of Materials. USA. : Prentice-Hall, Inc. (1999).

80. M. Oishi, Y. Matsuda, K. Noguchi and T. Masaki. Evaluation of Tensile Strength and Fracture Toughness of Yittria-Stabilized Zirconia Polycrystals with Fracture Surface Analysis. J.Am.Ceram.Soc. 78 (1995) : 1212-16.

81. J. Martinez-Fernandez, M. Jimenez-Melendo, A. Dominguez-Rodriguez and A.H. Heuer. Microindentation-Induced Transformation in 3.5-mol%- Yittria-Partially-Stabilized Zirconia Single Crystals. J.Am.Ceram.Soc. 74 (1991) : 1071-81.

82. T. Masaki and K. Kobayyaschi. High Toughened PSZ (Partially Stabilized Zirconia). Technology Development, Japan (1989). Cite in V. Apivatanapong. Preparation and Mechanical Characteristics of Hydroxyapatite's Substrate B.Sc. Project. Physics Science Chulalongkorn University, (1998).

83. ASTM: C 20-80a, Standard Test Methods for Apparent Porosity, Water Absorption, Apparent Specific Gravity, and Bulk Density of Bunded Refractory Brick and Shapes by Boiling water.

VITE

Miss Lugsanee Pinyo

1976 Born :dec., 1976 in Narathiwat , Thailand.

Fater : Mongkol Pinyo

Mother : Suwanna Pinyo

1995 – 1998 Bachelor of Science (Physis).

Prince of Songkhla University ,Songkhla , THAILAND.